COPERNICUS SPACE COMPONENT SENTINEL OPTICAL IMAGING

MISSION PERFORMANCE CLUSTER SERVICE

Data Quality Report

Sentinel-3 OLCI

March 2023

Ref.: OMPC.ACR.DQR.03.03-2023
Issue: 1.0
Date: 12/04/2023
Contract: 4000136252/21/I-BG

Customer:	ESA	**Document Ref.:**	OMPC.ACR.DQR.03.03-2023
Contract No.:	4000136252/21/I-BG	**Date:**	12/04/2023
		Issue:	1.0

Project:	COPERNICUS SPACE COMPONENT SENTINEL OPTICAL IMAGING MISSION PERFORMANCE CLUSTER SERVICE		
Title:	Data Quality Report - OLCI		
Author(s):	OLCI ESL team		
Approved by:	L. Bourg, OPT-MPC OLCI ESL Coordinator S. Clerc, OPT-MPC Optical ESL Coordinator	**Authorized by**	C. Hénocq, OPT-MPC S3 Technical Manager
Distribution:	ESA, EUMETSAT, published in Sentinel Online		
Accepted by ESA	S. Dransfeld, ESA TO		
Filename	OMPC.ACR.DQR.03.03-2023 - i1r0 - OLCI DQR March 2023.docx		

Disclaimer

The views expressed herein can in no way be taken to reflect the official opinion of the European Space Agency or the European Union.

Changes Log

Version	Date	Changes
1.0	12/04/2023	First version

List of Changes

Version	Section	Answers to RID	Changes

Table of content

TABLE OF CONTENT ..... **IV**

LIST OF FIGURES ..... **VI**

LIST OF TABLES ..... **XIII**

1 PROCESSING BASELINE VERSION **1**

1.1 Sentinel3-A 1

1.2 Sentinel3-B 1

2 INSTRUMENT MONITORING **2**

2.1 CCD temperatures 2

2.1.1 OLCI-A 2

2.1.2 OLCI-B 4

2.2 Radiometric Calibration 5

2.2.1 Dark Offsets [OLCI-L1B-CV-230] 8

2.2.3 Instrument response and degradation modelling [OLCI-L1B-CV-250] 18

2.2.4 Ageing of nominal diffuser [OLCI-L1B-CV-240] 36

2.2.5 Updating of calibration ADF [OLCI-L1B-CV-260] 45

2.3 Spectral Calibration [OLCI-L1B-CV-400] 45

2.3.1 OLCI-A 45

2.3.2 OLCI-B 45

2.4 Signal to Noise assessment [OLCI-L1B-CV-620] 46

2.4.1 SNR from Radiometric calibration data 46

2.5 Geometric Calibration/Validation 52

2.5.1 OLCI-A 52

2.5.2 OLCI-B 55

3 OLCI LEVEL 1 PRODUCT VALIDATION **59**

3.1 [OLCI-L1B-CV-300], [OLCI-L1B-CV-310] – Radiometric Validation 59

3.1.1 S3ETRAC Service 59

3.1.2 Radiometric validation with DIMITRI 61

3.1.3 Radiometric validation with OSCAR 66

3.1.4 Radiometric validation with Moon observations 71

4 LEVEL 2 LAND PRODUCTS VALIDATION **72**

4.1 [OLCI-L2LRF-CV-300] 72

4.1.1 Routine extractions 72

4.1.2 Comparisons with MERIS MGVI and MTCI climatology 82

4.1.3 Comparisons with GBOV (Ground-Based Observations for Validation) data v3 82

4.1.4 Sentinel-3A and 3B biophysical variables inter-annual variability results 82

4.2 [OLCI-L2LRF-CV-410 & OLCI-L2LRF-CV-420] – Cloud Masking & Surface Classification for Land Products 82

4.2.1 Sky Camera based validation – prototype results for January 2023 82
5 VALIDATION OF INTEGRATED WATER VAPOUR OVER LAND & WATER 96
6 LEVEL 2 SYN PRODUCTS VALIDATION 99
6.1 SYN L2 SDR products 99
6.1.1 Introduction: 99
6.1.2 Results and Discussion: 99
6.1.3 Conclusion 106
6.2 SY_2_VGP, SY_2_VG1 and SY_2_V10 products 107
6.3 SYN L2 AOD NTC products 110
7 EVENTS 111
8 APPENDIX A 112

List of Figures

Figure 1: long term monitoring of OLCI-A CCD temperatures using minimum value (top), time averaged values (middle), and maximum value (bottom) provided in the annotations of the Radiometric Calibration Level 1 products, for the shutter frames, all radiometric calibrations so far except the first one (absolute orbit 183) for which the instrument was not yet thermally stable. ---------- 2

Figure 2: Same as Figure 1 for diffuser frames.---------- 3

Figure 3: long term monitoring of OLCI-B CCD temperatures using minimum value (top), time averaged values (middle), and maximum value (bottom) provided in the annotations of the Radiometric Calibration Level 1 products, for the Shutter frames, all radiometric calibrations so far except the first one (absolute orbit 167) for which the instrument was not yet thermally stable. ---------- 4

Figure 4: same as Figure 3 for diffuser frames.---------- 5

Figure 5: Sun azimuth angles during acquired OLCI-A Radiometric Calibrations (diffuser frame) on top of nominal yearly cycle (black curve). Diffuser 1 with diamonds, diffuser 2 with crosses. Different colours correspond to different years of acquisition (see the legend inside the figure).---------- 6

Figure 6: same as Figure 5 for OLCI-B. ---------- 6

Figure 7: OLCI-A Sun geometry during radiometric Calibrations on top of characterization ones (diffuser frame)---------- 7

Figure 8: same as Figure 7 for OLCI-B---------- 7

Figure 9: Dark Offset table for band Oa06 with (red) and without (black) HEP filtering (Radiometric Calibration of 22 July 2017). The strong HEP event near pixel 400 has been detected and removed by the HEP filtering. ---------- 8

Figure 10: OLCI-A Dark Offset for band Oa1 (top) and Oa21 (bottom), all radiometric calibrations so far except the first one (orbit 183) for which the instrument was not thermally stable yet.---------- 9

Figure 11: map of OLCI-A periodic noise for the 5 cameras, for band Oa21. X-axis is detector number (East part, from 540 to 740, where the periodic noise occurs), Y-axis is the orbit number. Y-axis range is focused on the most recent 5000 orbits. The counts have been corrected from the West detectors mean value (not affected by periodic noise) in order to remove mean level gaps and consequently to have a better visualisation of the long term evolution of the periodic noise structure. At the beginning of the mission the periodic noise for band Oa21 had strong amplitude in camera 2, 3 and 5 compared to camera 1 and 4. However PN evolved through the mission and these discrepancies between cameras have been reduced. At the time of this Cyclic Report Camera 2 still shows a slightly higher PN than other cameras.---------- 10

Figure 12: same as Figure 11 for smear band.---------- 11

Figure 13: OLCI-A Dark Current for band Oa1 (top) and Oa21 (bottom), all radiometric calibrations so far except the first one (orbit 183) for which the instrument was not thermally stable yet.---------- 12

Figure 14: left column: ACT mean on 400 first detectors of OLCI-A Dark Current coefficients for spectral band Oa01 (top) and Oa21 (bottom). Right column: same as left column but for Standard deviation instead of mean. We see an increase of the DC level as a function of time especially for band Oa21.---------- 12

Figure 15: OLCI-A Dark current increase rates with time (in counts per year) vs. band (left) and vs. band width (right)---------- 13

Figure 16: OLCI-B Dark Offset for band Oa1 (top) and Oa21 (bottom), all radiometric calibrations so far except the first one (orbit 167) for which the instrument was not thermally stable yet.---------- 14

Figure 17: OLCI-B map of periodic noise for the 5 cameras, for band Oa21. X-axis is detector number (East part, from 540 to 740, where the periodic noise occurs), Y-axis is the orbit number. The counts have been corrected from the West detectors mean value (not affected by periodic noise) in order to remove mean level gaps and consequently to have a better visualization of the long term evolution of the periodic noise structure. ---------- 15

Figure 18: same as Figure 17 for smear band. ---------- 15

Figure 19: OLCI-B Dark Current for band Oa1 (top) and Oa21 (bottom), all radiometric calibrations so far except the first one (orbit 167) for which the instrument was not thermally stable yet. ---------- 16

Figure 20: left column: ACT mean on 400 first detectors of OLCI-B Dark Current coefficients for spectral band Oa01 (top) and Oa21 (bottom). Right column: same as left column but for Standard deviation instead of mean. We see an increase of the DC level as a function of time especially for band Oa21. ---------- 17

Figure 21: OLCI-B Dark Current increase rates with time (in counts per year) vs. band (left) and vs. band width (right) ---------- 17

Figure 22: OLCI-A Gain Coefficients for band Oa1 (top) and Oa21 (bottom), derived using the in-flight BRDF model. The dataset is made of all diffuser 1 radiometric calibrations since orbit 979. ---------- 18

Figure 23: camera averaged gain relative evolution with respect to calibration of 25/04/2016 (change of OLCI channel settings), as a function of elapsed time since the beginning of the mission; one curve for each band (see colour code on plots), one plot for each module. The diffuser ageing is taken into account.-- 19

Figure 24: OLCI-B Gain Coefficients for band Oa1 (top) and Oa21 (bottom), derived using the in-flight BRDF model. The dataset is made of all diffuser 1 radiometric calibrations since orbit 758. ---------- 20

Figure 25: OLCI-B camera averaged gain relative evolution with respect to first calibration after channel programming change (18/06/2018), as a function of elapsed time since the beginning of the mission; one curve for each band (see colour code on plots), one plot for each module. The diffuser ageing is taken into account. ---------- 21

Figure 26: RMS performance of the OLCI-A Gain Model of the current processing baseline as a function of orbit. ---------- 23

Figure 27: RMS performance of the OLCI-A Gain Model of the previous Processing Baseline as a function of orbit. ---------- 23

Figure 28: OLCI-A Camera-averaged instrument evolution since channel programming change (25/04/2016) and up to the most recent calibration (31/03/2023) versus wavelength. ---------- 24

Figure 29: For the 5 cameras: OLCI-A Evolution model performance, as camera-average and standard deviation of ratio of Model over Data vs. wavelength, for each orbit of the test dataset, including 22 calibrations in extrapolation, with a colour code for each calibration from blue (oldest) to red (most recent). ---------- 25

Figure 30: OLCI-A evolution model performance, as ratio of Model over Data vs. pixels, all cameras side by side, over the whole current calibration dataset (since instrument programming update), including 22 calibrations in extrapolation, channels Oa1 to Oa6. ---------- 26

Figure 31: same as Figure 30 for channels Oa7 to Oa14. ---------- 27

Figure 32: same as Figure 30 for channels Oa15 to Oa21. ---------- 28

Figure 33: RMS performance of the OLCI-B Gain Model of the current processing baseline as a function of orbit. ---------- 29

Figure 34: RMS performance of the OLCI-B Gain Model of the previous processing baseline as a function of orbit (please note the different vertical scale with respect to Figure 33).---------- 30

Figure 35: OLCI-B Camera-averaged instrument evolution since channel programming change (18/06/2018) and up to most recent calibration (31/03/2023) versus wavelength. ---------- 31

Figure 36: For the 5 cameras: OLCI-B Evolution model performance, as camera-average and standard deviation of ratio of Model over Data vs. wavelength, for each orbit of the test dataset, including 22 calibrations in extrapolation, with a colour code for each calibration from blue (oldest) to red (most recent). ---------- 32

Figure 37: OLCI-B evolution model performance, as ratio of Model over Data vs. pixels, all cameras side by side, over the whole current calibration dataset (since instrument programming update), including 22 calibrations in extrapolation, channels Oa1 to Oa6. ---------- 33

Figure 38: same as Figure 37 for channels Oa7 to Oa14. ---------- 34

Figure 39: same as for channels Oa15 to Oa21.---------- 35

Figure 40: diffuser 1 ageing for spectral band Oa01. We see strong ACT low frequency structures that are due to residual of BRDF modelling.---------- 37

Figure 41: same as Figure 40 for spectral band Oa17. We use this band in order to normalize other bands and remove the ACT structures due to residual of BRDF modelling. Normalized curve for spectral band Oa01 is presented in Figure 42. ---------- 37

Figure 42: same as Figure 40 after normalization by band Oa17. Ageing of the diffuser 1 is now visible in the 5 cameras.---------- 38

Figure 43: Diffuser 1 ageing as a function of wavelength (or spectral band). Ageing is clearly visible in spectral band #1 to #6. Note that all ageing sequences are plotted but in order to fit in the figure the box legend only displays 1 ageing sequence over 2 (including the most recent one). ---------- 38

Figure 44: Camera averaged ageing for band Oa01 (normalized by band Oa17) as a function of elapsed time. Linear fit for each camera is plotted. The slope (% loss per year) and the correlation coefficient. - 39

Figure 45: Slope of ageing fit (% of loss per exposure) vs wavelengths, using all the available ageing sequence at the time of the current reporting period (red curve) and at the time of previous reporting periods for which an ageing sequence was measured (see legend within the figure).---------- 40

Figure 46: OLCI-B diffuser 1 ageing for spectral band Oa01. We see strong ACT low frequency structures that are due to residual of BRDF modelling. ---------- 41

Figure 47: same as Figure 46 for spectral band Oa17. We use this band in order to normalize other bands and remove the ACT structures due to residual of BRDF modelling. Normalized curve for spectral band Oa01 is presented in Figure 48. ---------- 41

Figure 48: same as Figure 46 after normalization by band Oa17. Ageing of the diffuser 1 is now visible in the 5 cameras.---------- 42

Figure 49: OLCI-B Diffuser 1 ageing as a function of wavelength (or spectral band). Ageing is clearly visible in spectral band #1 to #5.---------- 42

Figure 50: Slope of ageing fit (% of loss per exposure) vs wavelengths, using all the available ageing sequence at the time of the current reporting period (red curve) and at the time of previous reporting periods for which an ageing sequence was measured (see legend within the figure).---------- 43

Figure 51: OLCI-B diffuser ageing (after 100 exposures, i.e. about two years) according to direct assessment from Yaw Manoeuvres (blue) and nominal method at Cycle 28 (orange).---------- 44

Figure 52: clustered Ageing sequences illumination geometries.---------- 44
Figure 53: various estimates of the ageing rate, according to nominal method for cycles 28, 46 and 62, according to direct assessment during Yaw manoeuvres, and according to the Equal SAA clustering for data up to 03/2022, 11/2022 and 03/2023. ---------- 45
Figure 54: OLCI-A Signal to Noise ratio as a function of the spectral band for the 5 cameras. These results have been computed from radiometric calibration data. All calibrations except first one (orbit 183) are presents with the colours corresponding to the orbit number (see legend). The SNR is very stable with time: the curves for all orbits are almost superimposed. The dashed curve is the ESA requirement.----- 46
Figure 55: long-term stability of the SNR estimates from Calibration data, example of channel Oa1. ---- 47
Figure 56: OLCI-B Signal to Noise ratio as a function of the spectral band for the 5 cameras. These results have been computed from radiometric calibration data. All calibrations except first one (orbit 167) are presents with the colours corresponding to the orbit number (see legend). The SNR is very stable with time: the curves for all orbits are almost superimposed. The dashed curve is the ESA requirement.----- 49
Figure 57: long-term stability of the OLCI-B SNR estimates from Calibration data, example of channel Oa1. ---------- 50
Figure 58: overall OLCI-A georeferencing RMS performance time series (left) and number of validated control points corresponding to the performance time series (right) over the whole monitoring period 52
Figure 59: across-track (left) and along-track (right) OLCI-A georeferencing biases time series for Camera 1. Blue line is the average, black lines are average plus and minus 1 sigma.---------- 53
Figure 60: same as Figure 59 for Camera 2. ---------- 53
Figure 61: same as Figure 59 for Camera 3. ---------- 53
Figure 62: same as Figure 59 for Camera 4. ---------- 54
Figure 63: same as Figure 59 for Camera 5. ---------- 54
Figure 64: OLCI-A spatial across-track misregistration at each camera transition (left) and maximum amplitude of the across-track error within each camera (left). ---------- 54
Figure 65: OLCI-A spatial along-track misregistration at each camera transition (left) and maximum amplitude of the along-track error within each camera (left). ---------- 55
Figure 66: overall OLCI-B georeferencing RMS performance time series over the whole monitoring period (left) and corresponding number of validated control points (right)---------- 55
Figure 67: across-track (left) and along-track (right) OLCI-B georeferencing biases time series for Camera 1.---------- 56
Figure 68: same as Figure 67 for Camera 2. ---------- 56
Figure 69: same as Figure 67 for Camera 3. ---------- 56
Figure 70: same as Figure 67 for Camera 4. ---------- 57
Figure 71: same as Figure 67 for Camera 5. ---------- 57
Figure 72: OLCI-B spatial across-track misregistration at each camera transition (left) and maximum amplitude of the across-track error within each camera (left). ---------- 57
Figure 73: OLCI-B spatial along-track misregistration at each camera transition (left) and maximum amplitude of the along-track error within each camera (left). ---------- 58
Figure 74: summary of S3ETRAC products generation for OLCI-A (number of OLCI-A L1 products Ingested, blue – number of S3ETRAC extracted products generated, green – number of S3ETRAC runs without

generation of output product (data not meeting selection requirements), yellow – number of runs ending in error, red, one plot per site type). ---------- 60

Figure 75: summary of S3ETRAC products generation for OLCI-B (number of OLCI-B L1 products Ingested, yellow – number of S3ETRAC extracted products generated, blue – number of S3ETRAC runs without generation of output product (data not meeting selection requirements), green – number of runs ending in error, red, one plot per site type). ---------- 61

Figure 76: Time-series of the elementary ratios (observed/simulated) signal from OLCI-A for (top to bottom) bands Oa03 and Oa17 respectively over January 2022-March 2023 from the six PICS Cal/Val sites. Dashed-green and orange lines indicate the 2% and 5% respectively. Error bars indicate the desert methodology uncertainty. ---------- 62

Figure 77: Time-series of the elementary ratios (observed/simulated) signal from OLCI-B for (top to bottom) bands Oa08 and Oa17 respectively over January 2022- March 2023 from the six PICS Cal/Val sites. Dashed-green and orange lines indicate the 2% and 5% respectively. Error bars indicate the desert methodology uncertainty. ---------- 63

Figure 78: The estimated gain values for OLCI-A and OLCI-B over the 6 PICS sites identified by CEOS over the period January 2022- March 2023 as a function of wavelength. Dashed-green and orange lines indicate the 2% and 5% respectively. Error bars indicate the desert methodology uncertainty. ---------- 64

Figure 79: The estimated gain values for OLCI-A and OLCI-B from Glint, Rayleigh and PICS methods over the past twelve months as a function of wavelength. We use the gain value of Oa8 from PICS-Desert method as reference gain for Glint method. Dashed-green and orange lines indicate the 2% and 5% respectively. Error bars indicate the method uncertainties. ---------- 65

Figure 80: Ratio of observed TOA reflectance to simulated one for (black) MERIS, (pale-green) S2A/MSI, (white) S2B/MSI, (blue) S3A/OLCI, (green) S3B/OLCI, (red) S3A/SLSTR-NADIR, and (cyan) S3B/SLSTR-NADIR averaged over the six PICS test sites over different periods as a function of wavelength. ---------- 66

Figure 81: OSCAR Rayleigh S3A and S3B Calibration results as a function of wavelength for March 2023. The results are obtained with a new climatology derived from CMEMS OLCI monthly CHL products. ---- 67

Figure 82: OSCAR Rayleigh OLCI-A and OLCI-B Calibration results as a function of wavelength for all acquisitions of 2023. The results are obtained with a new climatology derived from CMEMS OLCI monthly CHL products. ---------- 68

Figure 83: OSCAR Glitter OLCI-A & OLCI-B Calibration results as a function of wavelength for March 2023. The results are obtained with a new climatology derived from CMEMS OLCI monthly CHL products. ---- 70

Figure 84: OSCAR Glitter OLCI-A & OLCI-B Calibration results as a function of wavelength for all acquisitions of 2023. The results are obtained with a new climatology derived from CMEMS OLCI monthly CHL products. ---------- 70

Figure 85: DeGeb time series over current report period ---------- 72

Figure 86: ITCat time series over current report period ---------- 73

Figure 87: ITIsp time series over current report period ---------- 73

Figure 88: ITSro time series over current report period ---------- 74

Figure 89: ITTra time series over current report period ---------- 74

Figure 90: SPAli time series over current report period ---------- 75

Figure 91: UKNFo time series over current report period ---------- 75

Figure 92: USNe1 time series over current report period ---------- 76

Figure 93: USNe2 time series over current report period ---------- 76
Figure 94: USNe3 time series over current report period ---------- 77
Figure 95: DeGeb time series over current report period ---------- 77
Figure 96: ITCat time series over current report period ---------- 78
Figure 97: ITIsp time series over current report period ---------- 78
Figure 98: ITSro time series over current report period ---------- 79
Figure 99: ITTra time series over current report period ---------- 79
Figure 100: SPAli time series over current report period ---------- 80
Figure 101: UKNFo time series over current report period ---------- 80
Figure 102: USNe1 time series over current report period ---------- 81
Figure 103: USNe2 time series over current report period ---------- 81
Figure 104: USNe3 time series over current report period ---------- 82
Figure 105: Temperature and cloud cover Rome, March 2023 (source: https://world-weather.info/forecast/italy/rome/March-2023/) ---------- 84
Figure 106: Average temperature, rainy days, and rainfall over Rome, March 2023 (source: https://www.weather25.com/europe/italy/lazio/rome?page=month&month=March) ---------- 85
Figure 107: Sky camera acquisitions over Rome during Sentinel-3 OLCI overpass ---------- 86
Figure 108: Classified sky camera acquisitions over Rome during Sentinel-3 OLCI overpass ---------- 87
Figure 109: Comparison between OLCI L1 (SC position marked as Pin1), SC image and SC classification for 13th of March overpass of OLCI-A ---------- 88
Figure 110: Comparison between OLCI L1 (SC position marked as Pin1), SC image and SC classification for 15th of March overpass of OLCI-B ---------- 88
Figure 111: Comparison between OLCI L1 (SC position marked as Pin1), SC image and SC classification for 16th of March overpass of OLCI-B ---------- 88
Figure 112: Comparison between OLCI L1 (SC position marked as Pin1), SC image and SC classification for 16th of March overpass of OLCI-A ---------- 89
Figure 113: Confusion matrix showing validation results for OLCI L2 cloud screening including margin against SC1 automated classification. ---------- 89
Figure 114: Confusion matrix showing validation results for OLCI L2 cloud screening excluding margin against SC1 automated classification. ---------- 90
Figure 115: Temperature and cloud cover Valencia, March 2023 (source: https://world-weather.info/forecast/spain/valencia/march-2023/) ---------- 91
Figure 116: Average temperature, rainy days, and rainfall over Valencia, March 2023 (source: https://www.weather25.com/europe/spain/comunidad-valenciana/valencia?page=month&month=March) ---------- 92
Figure 117: Sky camera acquisitions over Rome during Sentinel-3 OLCI overpass ---------- 93
Figure 118: Classified sky camera acquisitions over Rome during Sentinel-3 OLCI overpass ---------- 94
Figure 119: Confusion matrix showing validation results for OLCI L2 cloud screening including margin against SC1 automated classification. ---------- 95

Figure 120: Confusion matrix showing validation results for OLCI L2 cloud screening excluding margin against SC1 automated classification. ---------- 95

Figure 121: Upper: Scatter plot of the IWV products, derived from OLCI (A left, B right) above land and from SUOMI NET GNSS measurements. Middle: Histogram of the difference between OLCI (A: left, B: right) and GNSS (blue: original OLCI, orange: bias corrected OLCI). Lower: Positions of the GNSS (A: left, B: right). ---------- 97

Figure 122: Temporal evolution of different quality measures for OLCI A (left) and OLCI B (right) with respect to SUOMI Net. From top to bottom: systematic deviation factor, bias, root mean squared difference (with and without bias correction), explained variance (number in boxes are the numbers of matchups) ---------- 98

Figure 123: Scatter plots of intercomparison between sentinel S3A SYN SDR (OLCI) and MODIS for selected band pairs, b01 vs Oa08 (a), b02 vs Oa17 (b), b03 vs Oa04 (c) and b04 vs Oa06 (d). ---------- 101

Figure 124: Scatter plot of intercomparison between sentinel S3B SYN SDR (OLCI) and MODIS for selected band pairs, b01 vs Oa08 (a), b02 vs Oa17 (b), b03 vs Oa04 (c) and b04 vs Oa06 (d) ---------- 102

Figure 125: Scatter plot of intercomparison between sentinel S3B SYN SDR (OLCI) and VIIRS for selected band pairs, M5 vs Oa09 (a), M7 vs Oa17 (b), M3 vs Oa04 (c) and M4 vs Oa06 (d) ---------- 103

Figure 126: Scatter plot of intercomparison between sentinel S3B SYN SDR (OLCI) and VIIRS for selected band pairs, M5 vs Oa09 (a), M7 vs Oa17 (b), M3 vs Oa04 (c) and M4 vs Oa06 (d) ---------- 104

Figure 127: Scatter plot of intercomparison between sentinel S3A SYN SDR (OLCI) and MODIS for selected band pairs, b01 vs Oa08 (a), b02 vs Oa17 (b), b03 vs Oa04 (c) and b04 vs Oa06 (d) ---------- 105

Figure 128: Scatter plot of intercomparison between sentinel S3B SYN SDR (OLCI) and MODIS for selected band pairs, b01 vs Oa08 (a), b02 vs Oa17 (b), b03 vs Oa04 (c) and b04 vs Oa06 (d) ---------- 106

Figure 129: Scatter density plots between SY_V10 S3A (top) or S3B (bottom) and PROBA-V C2 S10-TOC for BLUE, RED, NIR and SWIR bands (left to right), March/2023 vs. March/2020 ---------- 108

Figure 130: Temporal evolution of APU statistics between SY_2_V10 S3A (left) or S3B (right) and PROBA-V S10-TOC for BLUE, RED, NIR and SWIR bands (top to bottom), January/2021 - March/2023 (S3 SYN VGT) vs. January/2018 - March/2020 (PROBA-V) ---------- 109

List of Tables

Table 1: OLCI-A SNR figures as derived from Radiometric Calibration data. Figures are given for each camera (time average and standard deviation), and for the whole instrument. The requirement and its reference radiance level are recalled (in $mW.sr^{-1}.m^{-2}.nm^{-1}$). ---------- 48

Table 2: OLCI-B SNR figures as derived from Radiometric Calibration data. Figures are given for each camera (time average and standard deviation), and for the whole instrument. The requirement and its reference radiance level are recalled (in $mW.sr^{-1}.m^{-2}.nm^{-1}$). ---------- 51

Table 3: S3ETRAC Rayleigh Calibration sites ---------- 67

Table 4. OSCAR Rayleigh calibration results for S3A and S3B (average and standard deviation over all 2023 acquisitions) over all scenes currently (re)processed with the new climatology and observed difference (in %) between OLCIA and OLCIB ---------- 68

Table 5: OSCAR Glitter calibration results for OLCI-A and OLCI-B (average and standard deviation over all acquisitions of 2023) currently processed with the new climatology and observed difference (in %) ---- 71

Table 6: List of CEOS LPV sited used as reference sites for intercomparison of SYN SDR products. ------- 100

1 Processing Baseline Version

1.1 Sentinel3-A

IPF	IPF / Processing Baseline version	Date of deployment
OL1	06.13 / OL__L1_.003.00.00 (with uncertainties activated)	23/08/2022
OL2 LAND	06.16 / OL__L2L.002.10.01	23/08/2022
SY2	06.23 / SYN_L2_.002.16.00	23/08/2022
SY2_VGS	06.11 / SYN_L2V.002.08.00	23/08/2022
SY2_AOD	01.06 / AOD_NTC.002.06.01	23/08/2022

1.2 Sentinel3-B

IPF	IPF / Processing Baseline version	Date of deployment
OL1	06.13 / OL__L1_.003.00.00 (with uncertainties activated)	31/08/2022
OL2 Land	06.16 / OL__L2L.002.10.01	05/09/2022
SY2	06.23 / SYN_L2_.002.16.00	09/09/2022
SY2_VGS	06.11 / SYN_L2V.002.08.00	09/09/2022
SY2_AOD	01.06 / AOD_NTC.002.06.01	09/09/2022

2 Instrument monitoring

2.1 CCD temperatures

2.1.1 OLCI-A

The long-term monitoring of the CCD temperatures is based on Radiometric Calibration Annotations (see Figure 1). Variations are very small (0.09 C peak-to-peak) and no trend can be identified. Data from current reporting period (rightmost data points) do not show any specificity.

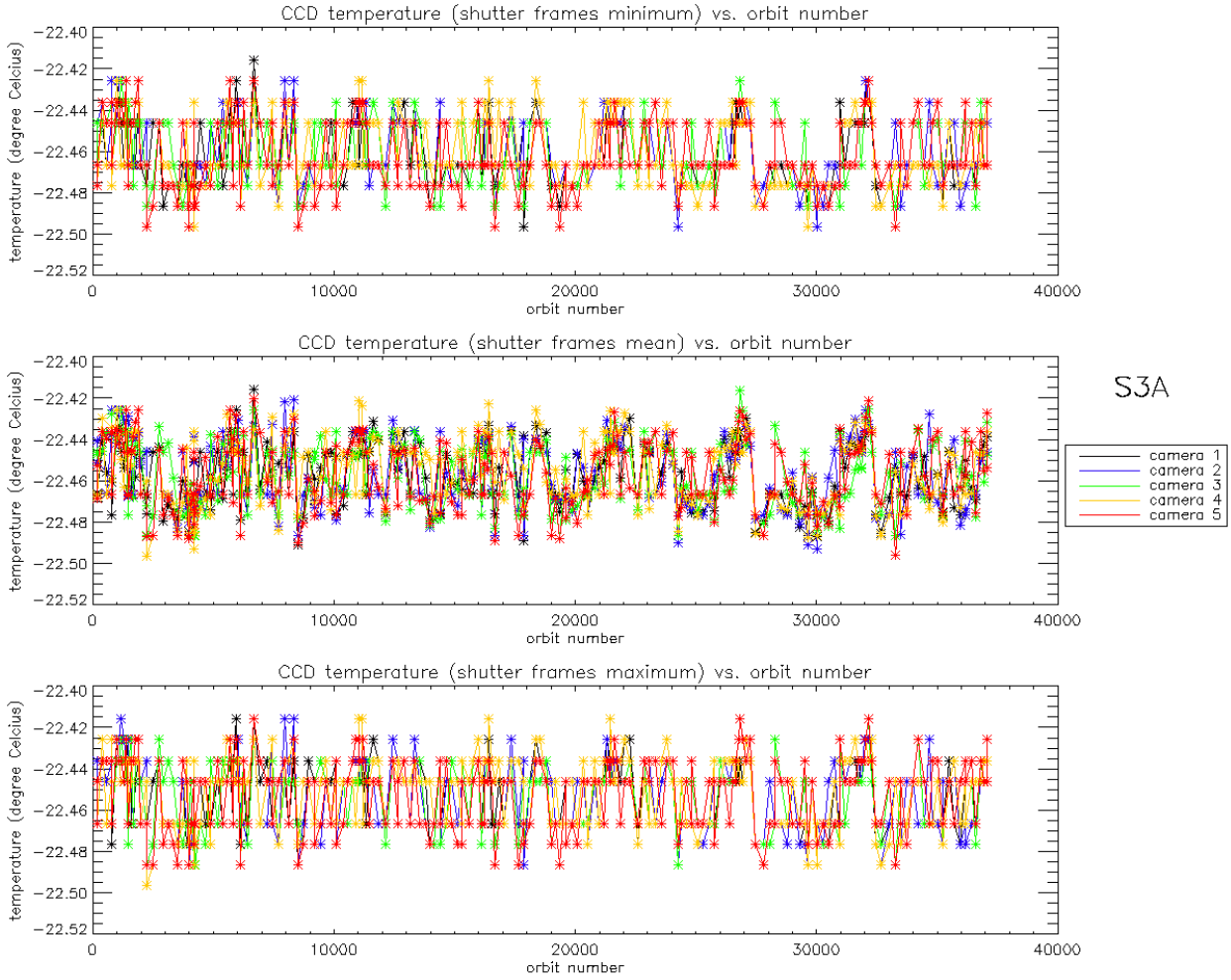

Figure 1: long term monitoring of OLCI-A CCD temperatures using minimum value (top), time averaged values (middle), and maximum value (bottom) provided in the annotations of the Radiometric Calibration Level 1 products, for the shutter frames, all radiometric calibrations so far except the first one (absolute orbit 183) for which the instrument was not yet thermally stable.

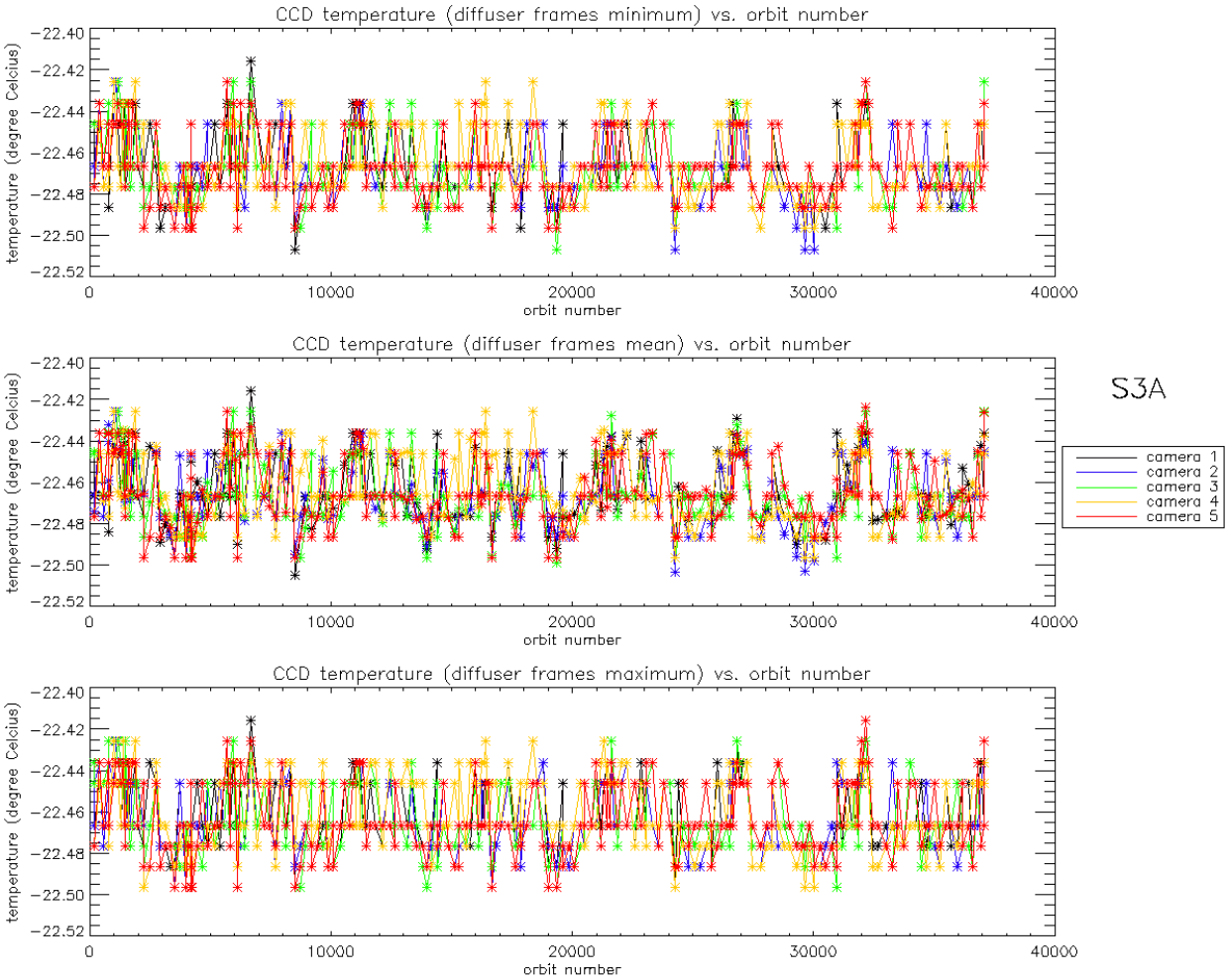

Figure 2: Same as Figure 1 for diffuser frames.

2.1.2 OLCI-B

As for OLCI-A, the variations of CCD temperature are very small (0.08 C peak-to-peak) and no trend can be identified. Data from current reporting period (rightmost data points) do not show any specificity.

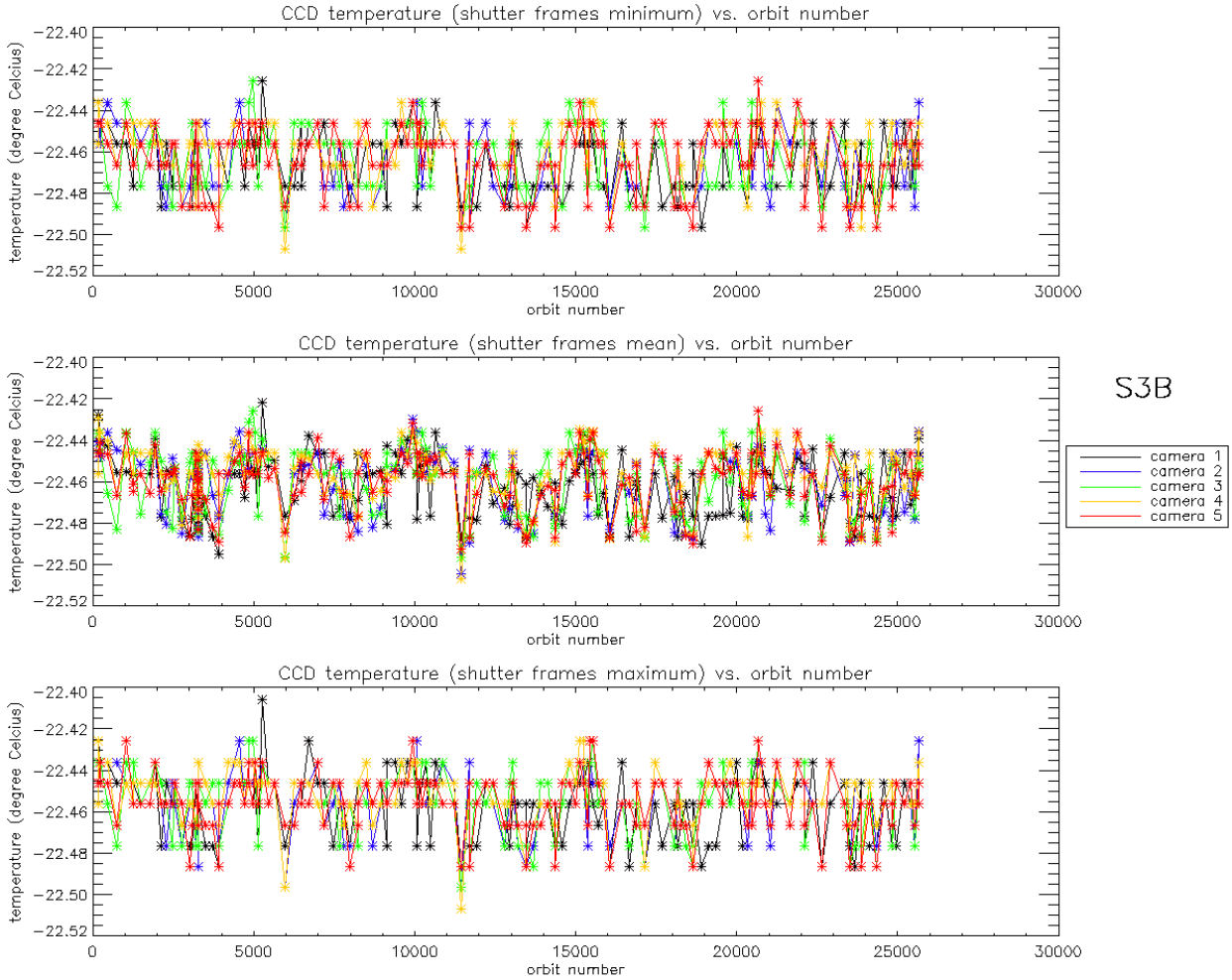

Figure 3: long term monitoring of OLCI-B CCD temperatures using minimum value (top), time averaged values (middle), and maximum value (bottom) provided in the annotations of the Radiometric Calibration Level 1 products, for the Shutter frames, all radiometric calibrations so far except the first one (absolute orbit 167) for which the instrument was not yet thermally stable.

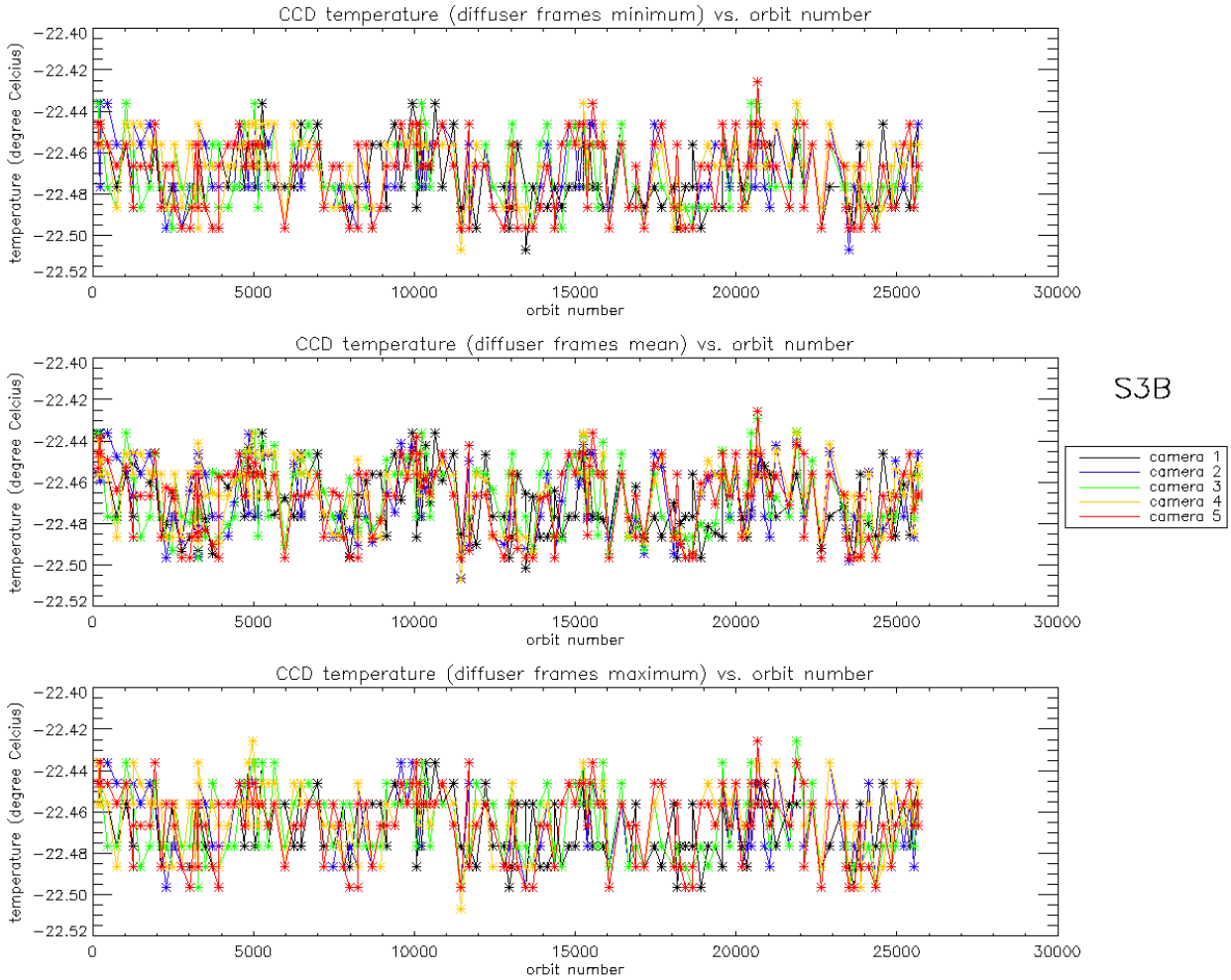

Figure 4: same as Figure 3 for diffuser frames.

2.2 Radiometric Calibration

For OLCI-A, four Radiometric Calibration sequences have been acquired during the reported period:

- S01 sequence (diffuser 1) on 12/03/2023 05:13 to 05:15 (absolute orbit 36795)
- S01 sequence (diffuser 1) on 22/03/2023 10:56 to 10:58 (absolute orbit 36941)
- S01 sequence (diffuser 1) on 31/03/2023 18:46 to 18:48 (absolute orbit 37074)
- S05 sequence (diffuser 2) on 31/03/2023 20:27 to 20:29 (absolute orbit 37075)

For OLCI-B, four Radiometric Calibration sequences have been acquired during the reported period:

- S01 sequence (diffuser 1) on 11/03/2023 08:22 to 08:24 (absolute orbit 25389)
- S01 sequence (diffuser 1) on 21/03/2023 19:08 to 19:10 (absolute orbit 25538)
- S01 sequence (diffuser 1) on 31/03/2023 02:58 to 03:00 (absolute orbit 25671)
- S05 sequence (diffuser 2) on 31/03/2023 04:39 to 04:41 (absolute orbit 25672)

The acquired Sun azimuth angles are presented on Figure 5 for OLCI-A and Figure 6 for OLCI-B, on top of the nominal values without Yaw Manoeuvre (i.e. with nominal Yaw Steering control of the satellite).

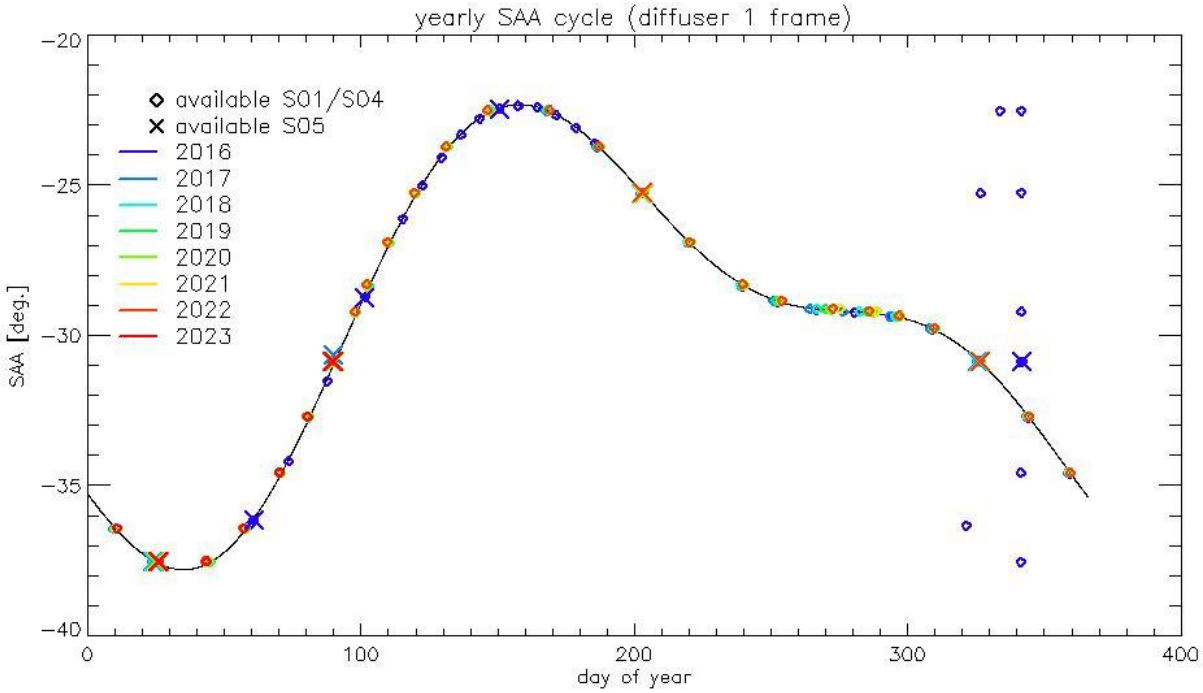

Figure 5: Sun azimuth angles during acquired OLCI-A Radiometric Calibrations (diffuser frame) on top of nominal yearly cycle (black curve). Diffuser 1 with diamonds, diffuser 2 with crosses. Different colours correspond to different years of acquisition (see the legend inside the figure).

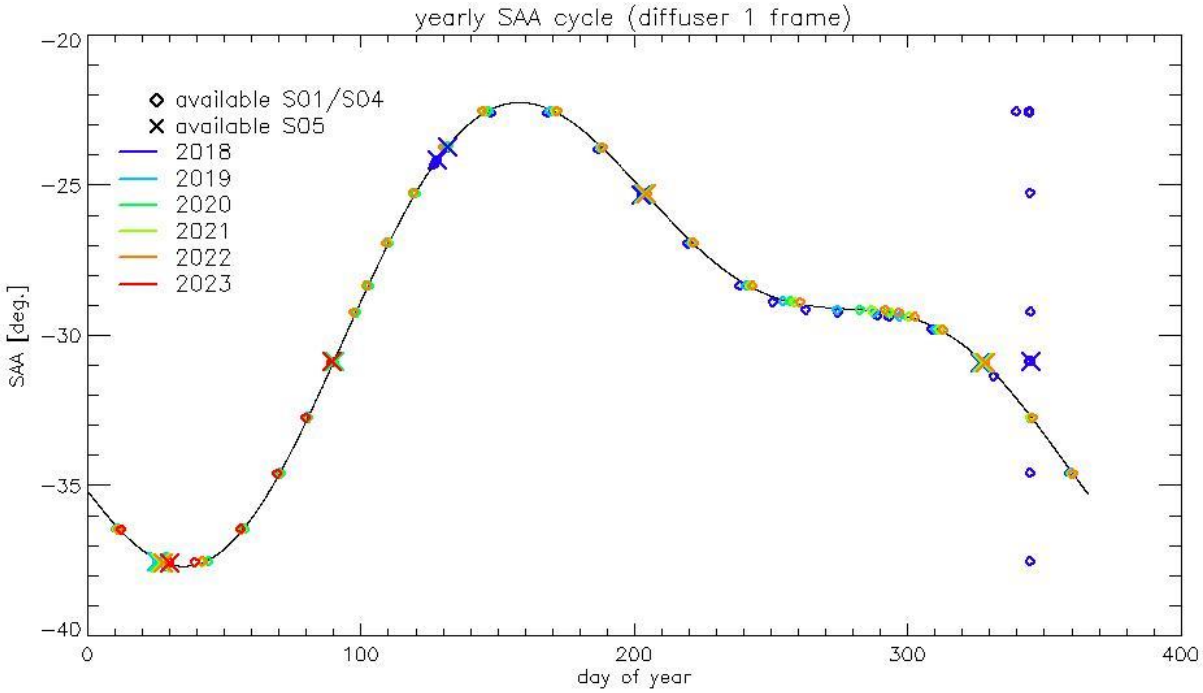

Figure 6: same as Figure 5 for OLCI-B.

Sun Zenith Angles as a function of Sun Azimuth Angles are presented in Figure 7 for OLCI-A and Figure 8 for OLCI-B.

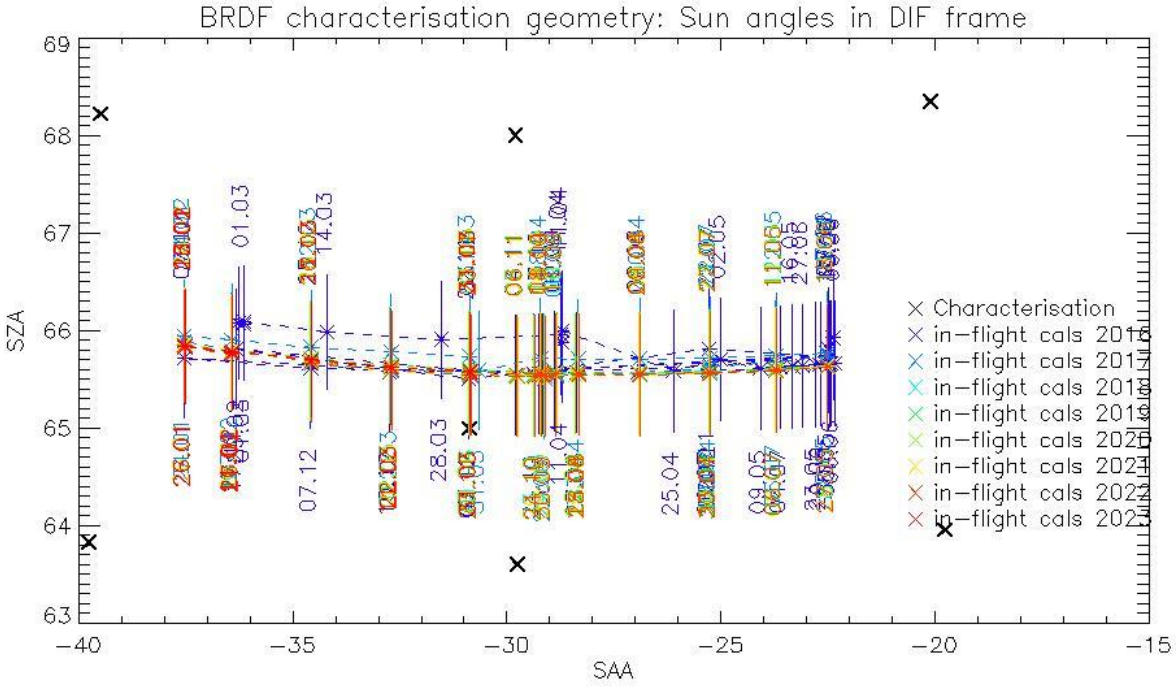

Figure 7: OLCI-A Sun geometry during radiometric Calibrations on top of characterization ones (diffuser frame)

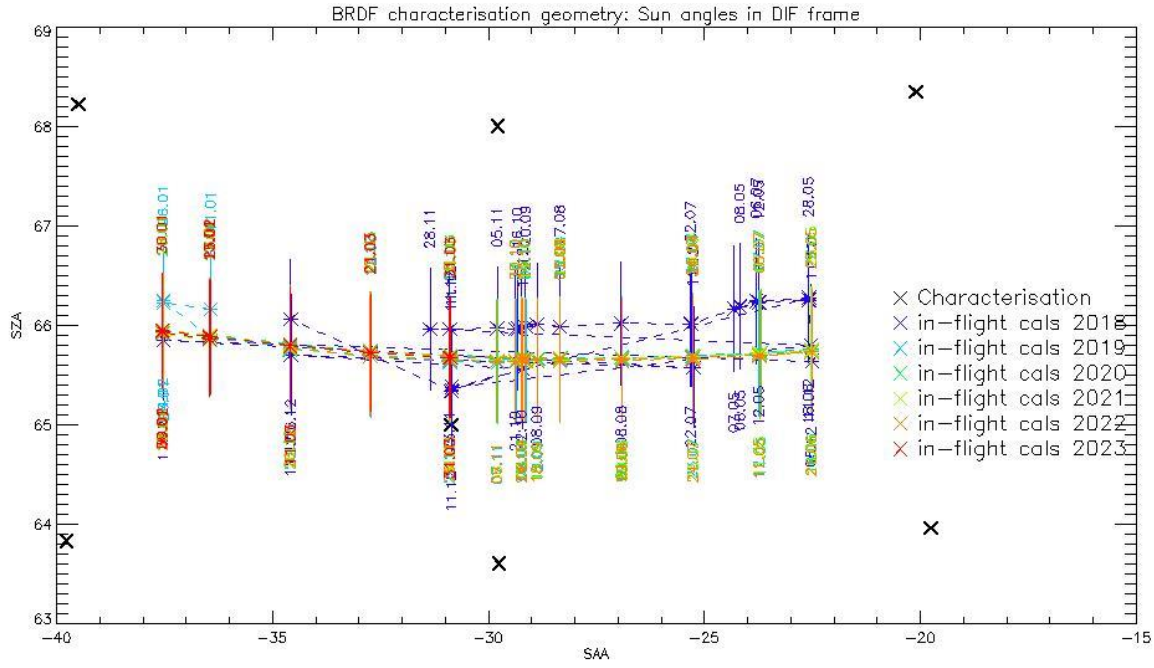

Figure 8: same as Figure 7 for OLCI-B

2.2.1 Dark Offsets [OLCI-L1B-CV-230]

Note about the High Energy Particles:

The filtering of High Energy Particle (HEP) events from radiometric calibration data has been implemented (for shutter frames only) in a post processor, allowing generating Dark Offset and Dark Current tables computed on filtered data. The post-processor starts from IPF intermediate data (corrected counts), applies the HEP detection and filtering and finally computes the Dark Offset and Dark Current tables the same way as IPF. An example of the impact of HEP filtering is given in Figure 9.

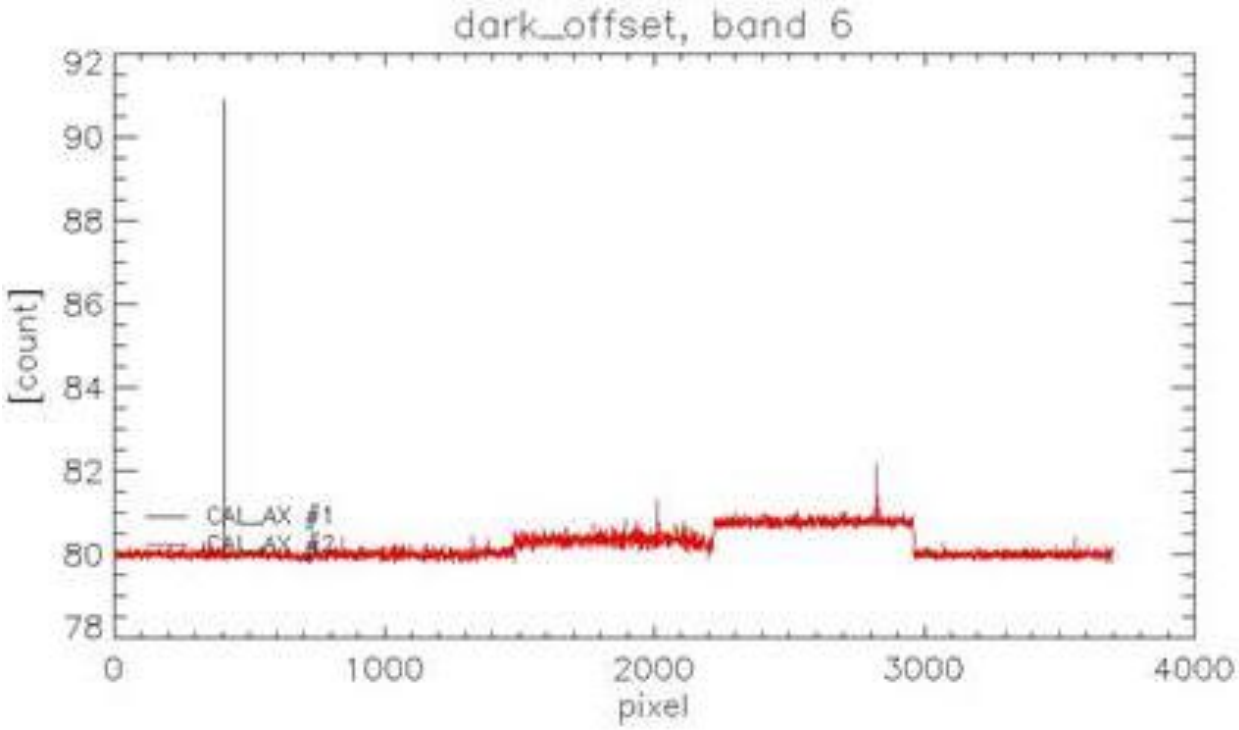

Figure 9: Dark Offset table for band Oa06 with (red) and without (black) HEP filtering (Radiometric Calibration of 22 July 2017). The strong HEP event near pixel 400 has been detected and removed by the HEP filtering.

All results presented below in this section have been obtained using the HEP filtered Dark Offset and Dark Current tables.

2.2.1.2 OLCI-A

Dark offsets

Dark offsets are continuously affected by the global offset induced by the Periodic Noise on the OCL (Offset Control Loop) convergence. Current reporting period calibrations are affected the same way as others. The amplitude of the shift varies with band and camera from virtually nothing (e.g. camera 2, band 0a1) to up to 5 counts (Oa21, camera 3). The Periodic Noise itself comes on top of the global shift with its known signature: high frequency oscillations with a rapid damp. This effect remains more or less stable with time in terms of amplitude, frequency and decay length, but its phase varies with time, introducing the global offset mentioned above.

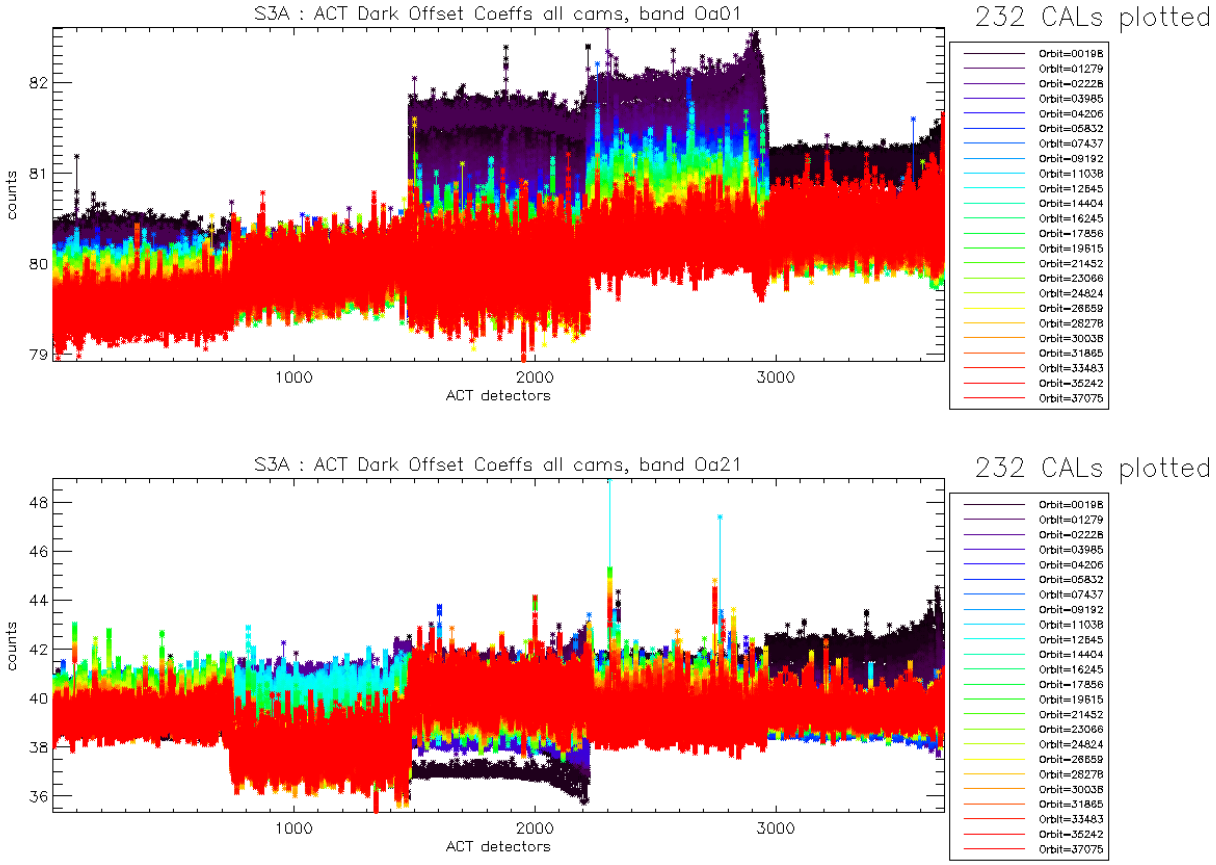

Figure 10: OLCI-A Dark Offset for band Oa1 (top) and Oa21 (bottom), all radiometric calibrations so far except the first one (orbit 183) for which the instrument was not thermally stable yet.

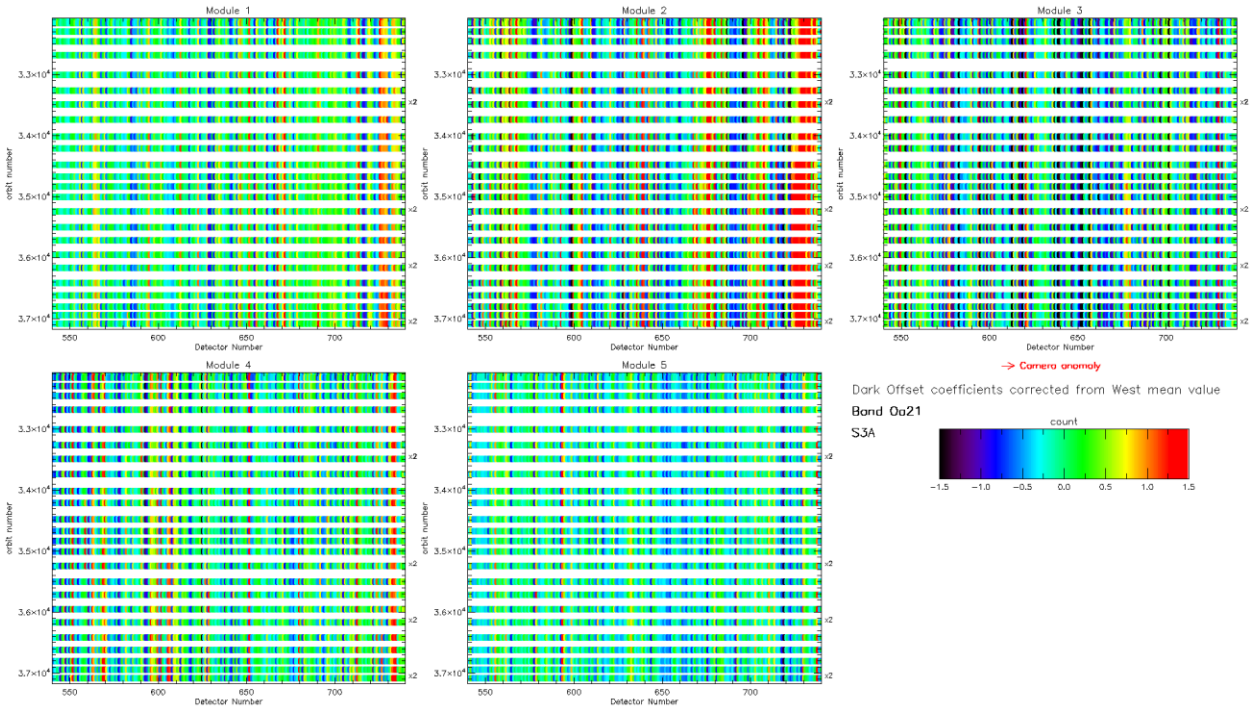

Figure 11: map of OLCI-A periodic noise for the 5 cameras, for band Oa21. X-axis is detector number (East part, from 540 to 740, where the periodic noise occurs), Y-axis is the orbit number. Y-axis range is focused on the most recent 5000 orbits. The counts have been corrected from the West detectors mean value (not affected by periodic noise) in order to remove mean level gaps and consequently to have a better visualisation of the long term evolution of the periodic noise structure. At the beginning of the mission the periodic noise for band Oa21 had strong amplitude in camera 2, 3 and 5 compared to camera 1 and 4. However PN evolved through the mission and these discrepancies between cameras have been reduced. At the time of this Cyclic Report Camera 2 still shows a slightly higher PN than other cameras.

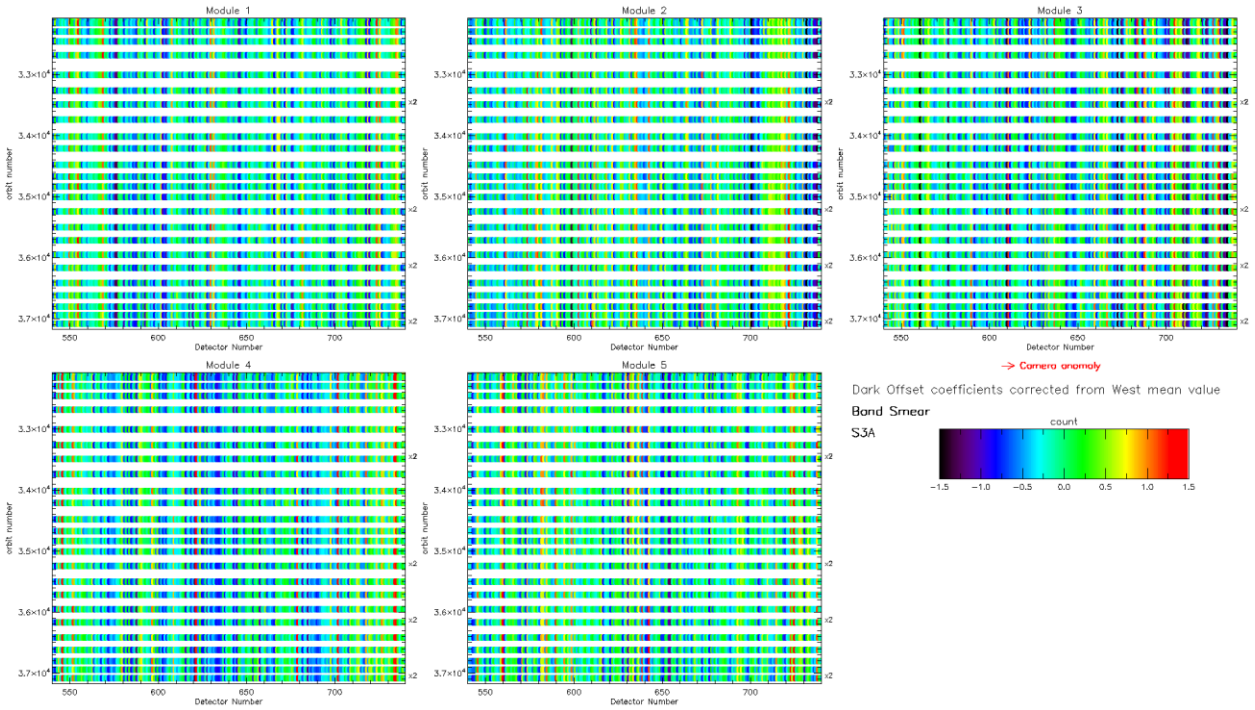

Figure 12: same as Figure 11 for smear band.

Figure 11 and Figure 12 show the so-called 'map of periodic noise' in the 5 cameras, for respectively band 21 and smear band. These maps have been computed from the dark offsets after removal of the mean level of the WEST detectors (not impacted by PN) in order to remove mean level gaps from one CAL to the other and consequently to highlight the shape of the PN. Maps are focused on the last 200 EAST detectors where PN occurs and on a time range covering only the last 5000 orbits in order to better visualize the CALs of the current reporting period.

Figure 11 and Figure 12 show that at this stage of the mission the PN is very stable in all cameras. There is no special behaviour noticed during the reporting period.

Dark Currents

Dark Currents (Figure 13) are not affected by the global offset of the Dark Offsets, thanks to the clamping to the average blind pixels value. However, the oscillations of Periodic Noise remain visible. There is no significant evolution of this parameter during the current reporting period except the small regular increase (almost linear), for all detectors, since the beginning of the mission (see Figure 14).

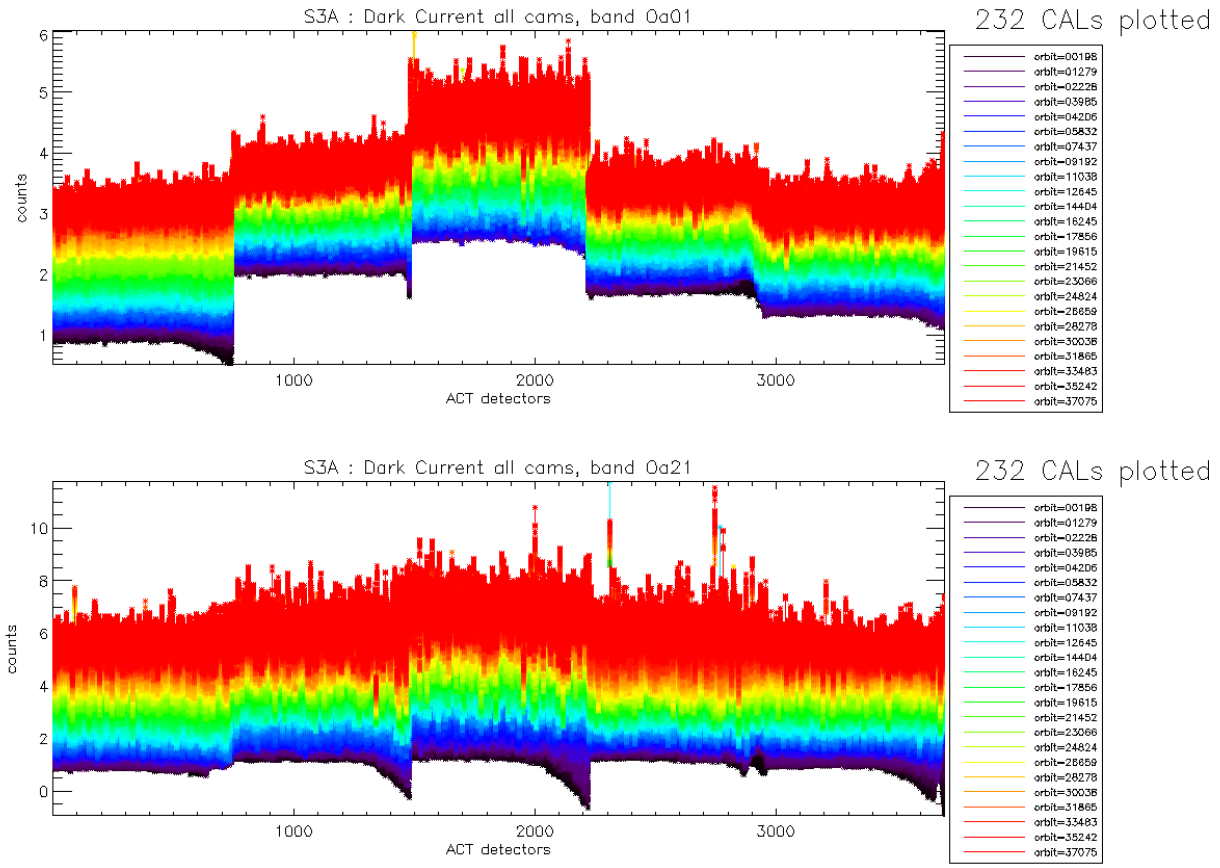

Figure 13: OLCI-A Dark Current for band Oa1 (top) and Oa21 (bottom), all radiometric calibrations so far except the first one (orbit 183) for which the instrument was not thermally stable yet.

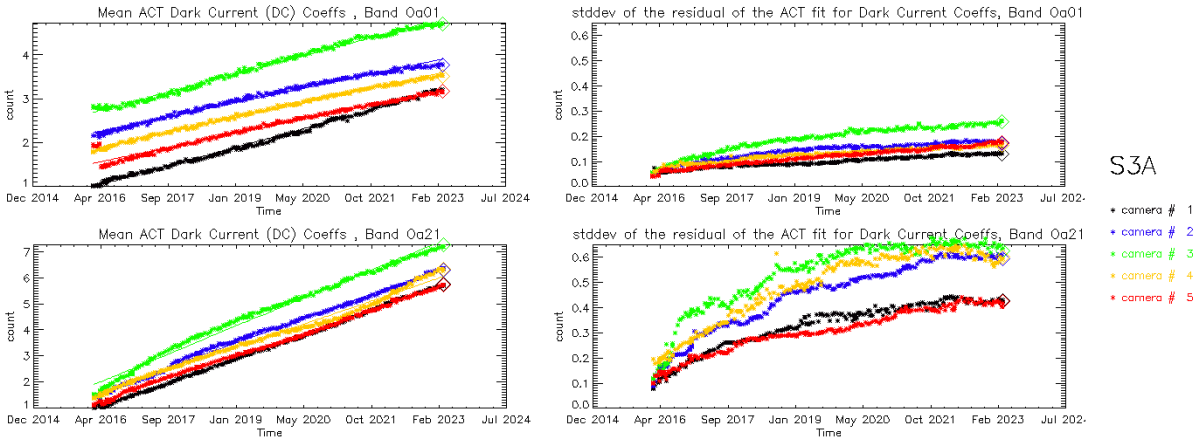

Figure 14: left column: ACT mean on 400 first detectors of OLCI-A Dark Current coefficients for spectral band Oa01 (top) and Oa21 (bottom). Right column: same as left column but for Standard deviation instead of mean. We see an increase of the DC level as a function of time especially for band Oa21.

A possible explanation of the regular increase of DC could be the increase of the number of hot pixels which is more important in Oa21 because this band is made of more CCD lines than band Oa01 and thus receives more cosmic rays impacts. It is known that cosmic rays degrade the structure of the CCD, generating more and more hot pixels at long term scales. Indeed, when computing the time slopes of the spatially averaged Dark Current as a function of band, i.e. the slopes of curves in left plots of Figure 14, one can see that Oa21 is by far the most affected, followed by the smear band (Figure 15, left); when plotting these slopes against total band width (in CCD rows, regardless of the number of micro-bands), the correlation between the slope values and the width becomes clear (Figure 15, right).

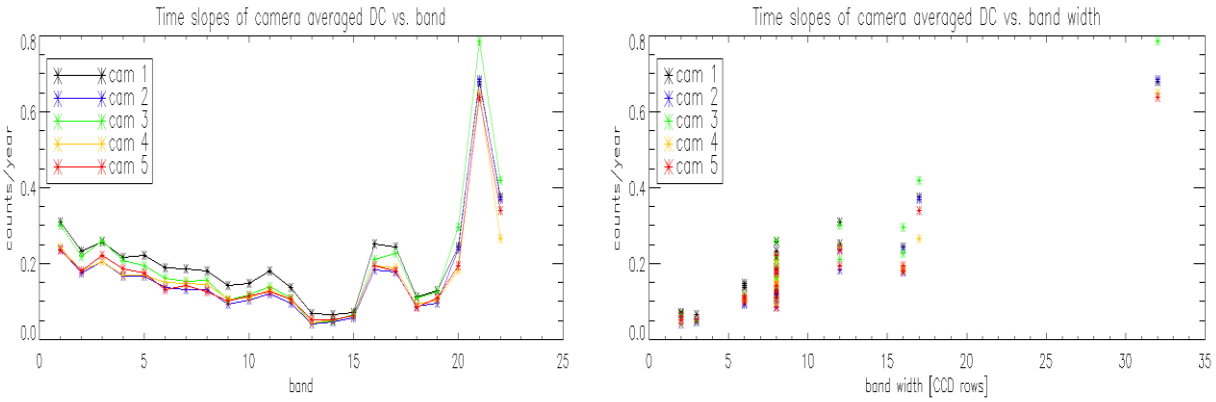

Figure 15: OLCI-A Dark current increase rates with time (in counts per year) vs. band (left) and vs. band width (right)

2.2.1.3 OLCI-B

Dark Offsets

Dark offsets for OLCI-B show a similar behaviour than for OLCI-A: mean level gaps between different orbits, induced by the presence of a pseudo periodic noise on the east edge of the cameras with a drifting phase.

Evolution of OLCI-B Dark Offset coefficients for band Oa01 and Oa21 are represented in Figure 16.

The periodic noise maps are shown for band Oa21 and smear band respectively in Figure 17 and Figure 18. As it happened for OLCI-A after a few thousands of orbits, the strong periodic noise phase and amplitude drift, present at the very beginning of the mission is now showing a clear stabilization.

Despite this overall stabilization, small evolutions are still noticeable in some bands/camera, like for example camera 1 in band Oa21 (upper left map in Figure 17) or in camera 1 band smear (upper left map in Figure 18).

Globally, OLCI-B PN is slightly less stabilized than OLCI-A PN.

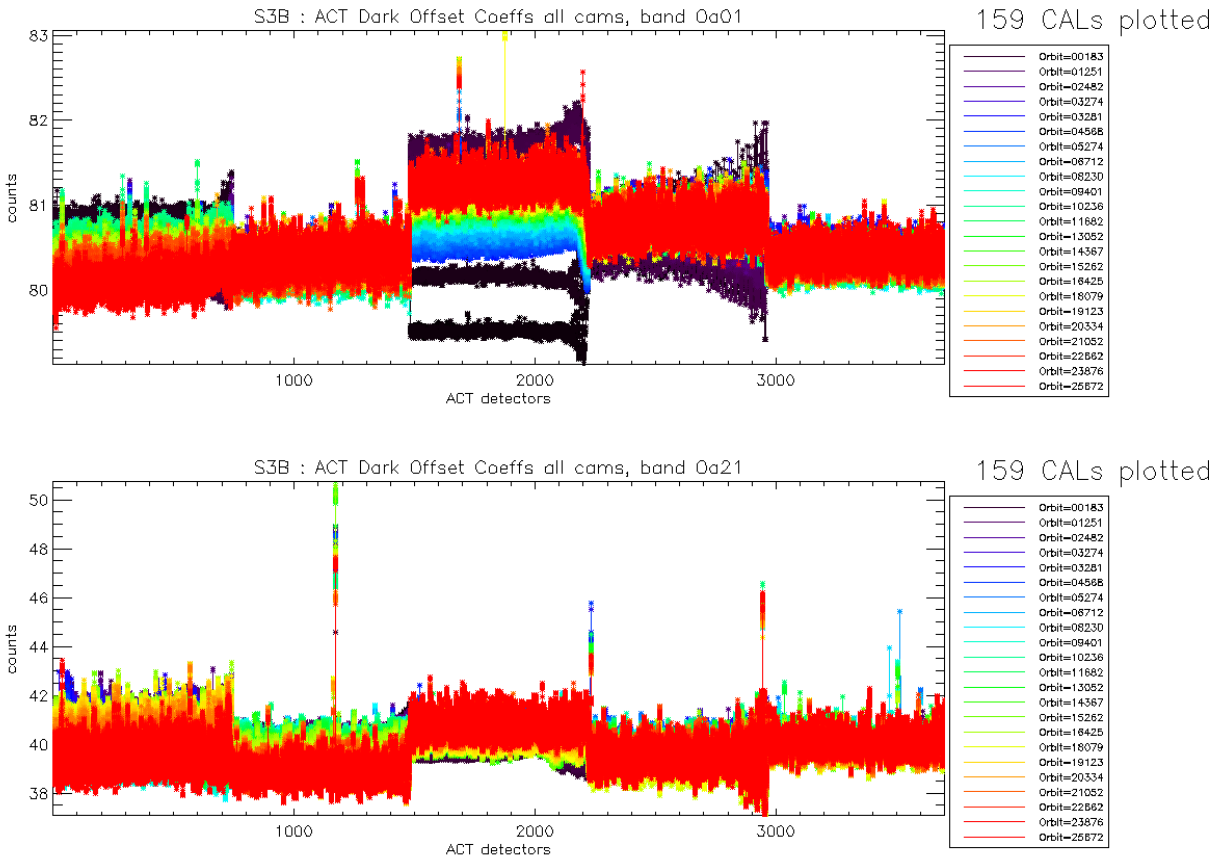

Figure 16: OLCI-B Dark Offset for band Oa1 (top) and Oa21 (bottom), all radiometric calibrations so far except the first one (orbit 167) for which the instrument was not thermally stable yet.

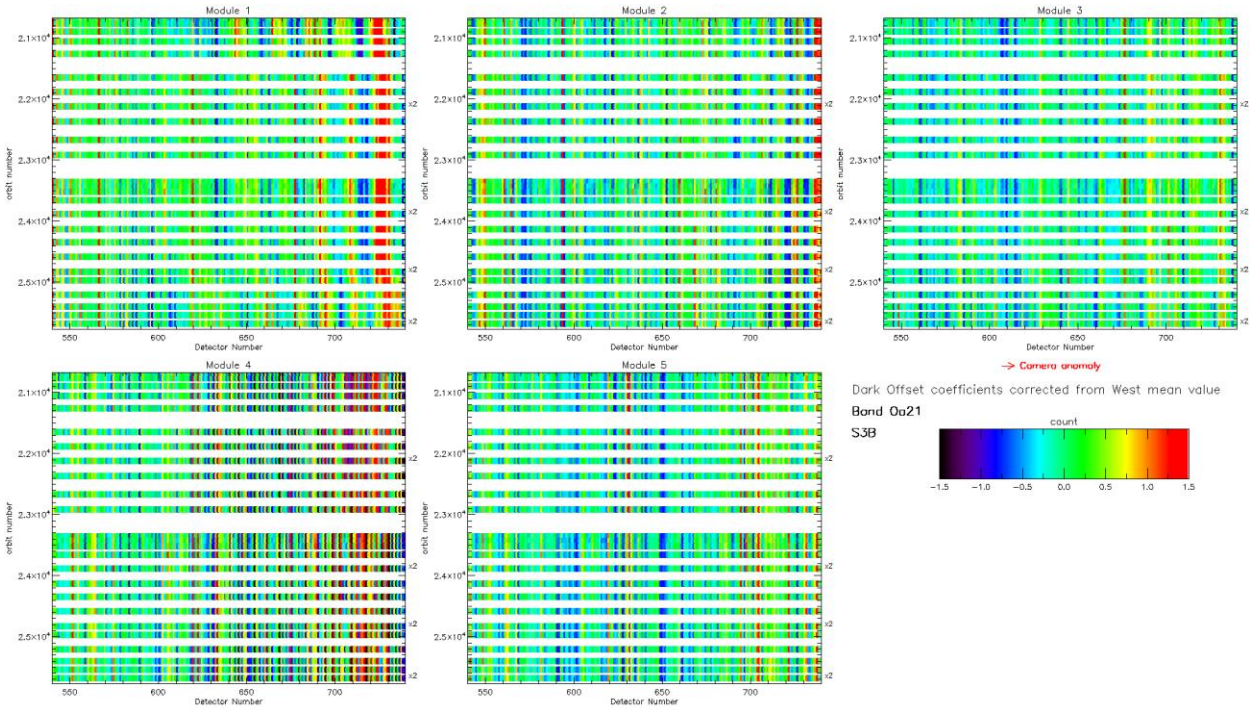

Figure 17: OLCI-B map of periodic noise for the 5 cameras, for band Oa21. X-axis is detector number (East part, from 540 to 740, where the periodic noise occurs), Y-axis is the orbit number. The counts have been corrected from the West detectors mean value (not affected by periodic noise) in order to remove mean level gaps and consequently to have a better visualization of the long term evolution of the periodic noise structure.

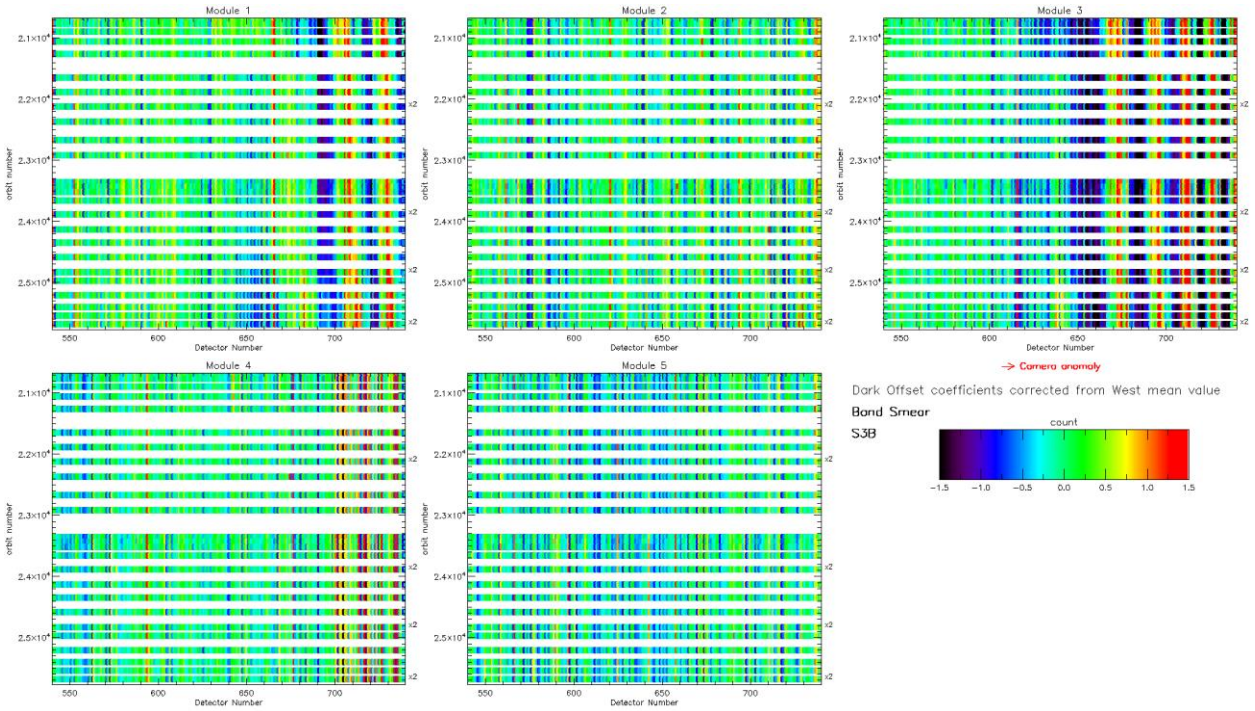

Figure 18: same as Figure 17 for smear band.

Dark Currents

As for OLCI-A there is no significant evolution of the Dark Current coefficients (Figure 19) during the current reporting period except the small regular increase (almost linear), for all detectors, since the beginning of the mission (see Figure 20) probably due to an increase of hot pixels (see Figure 21).

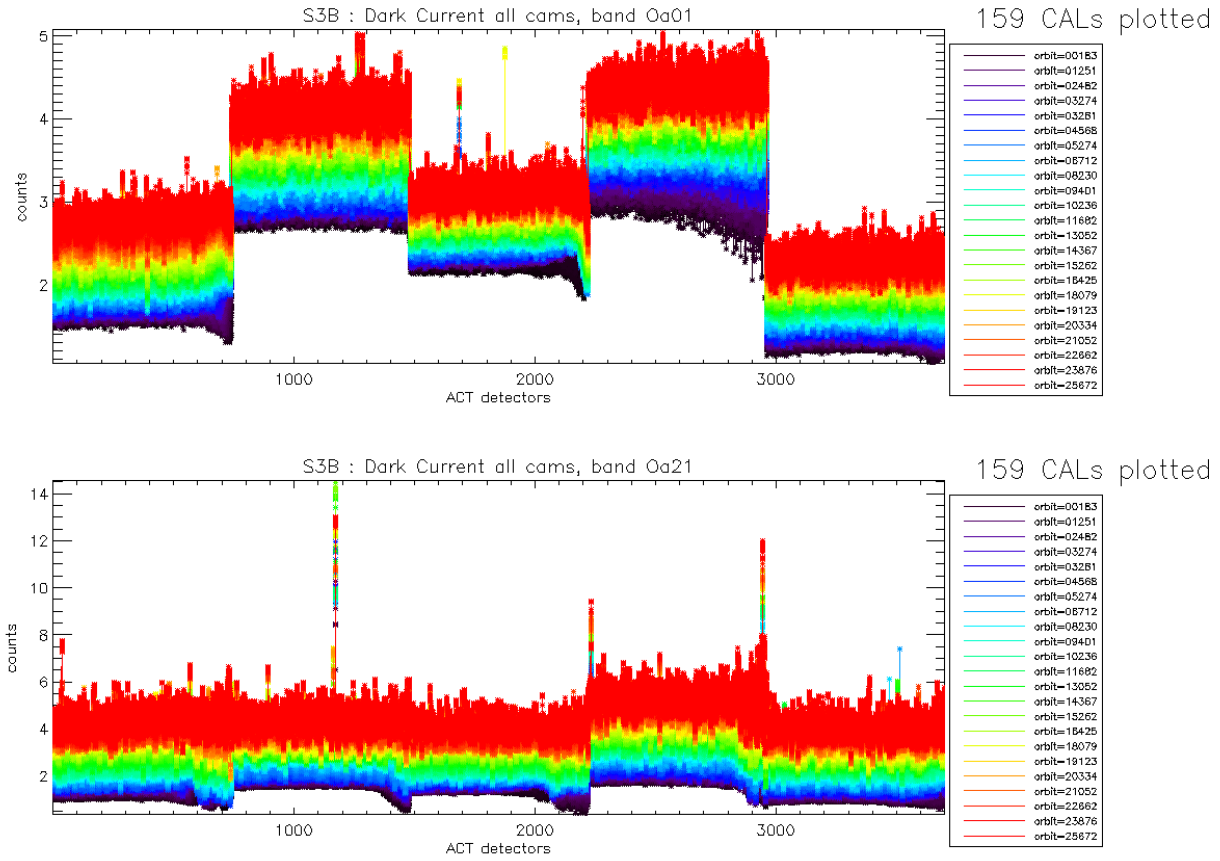

Figure 19: OLCI-B Dark Current for band Oa1 (top) and Oa21 (bottom), all radiometric calibrations so far except the first one (orbit 167) for which the instrument was not thermally stable yet.

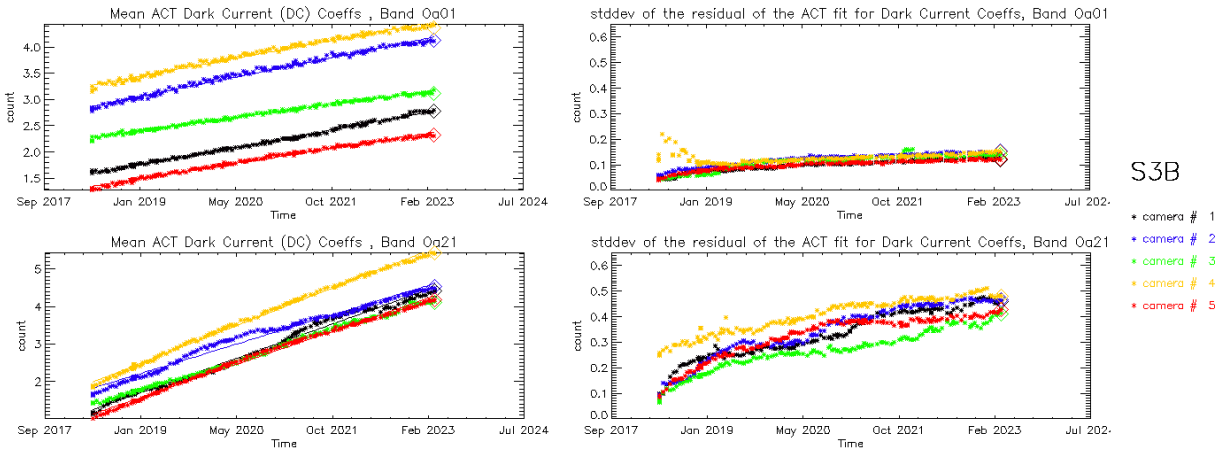

Figure 20: left column: ACT mean on 400 first detectors of OLCI-B Dark Current coefficients for spectral band Oa01 (top) and Oa21 (bottom). Right column: same as left column but for Standard deviation instead of mean. We see an increase of the DC level as a function of time especially for band Oa21.

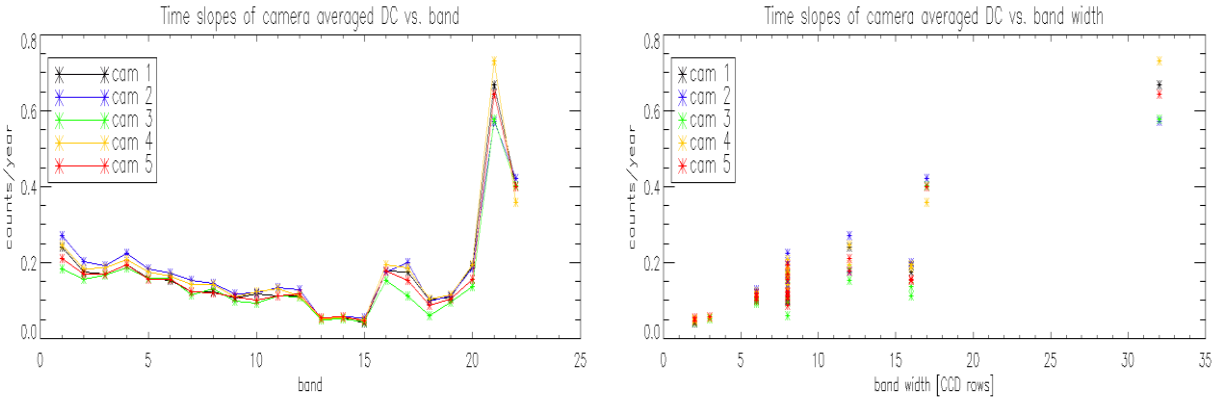

Figure 21: OLCI-B Dark Current increase rates with time (in counts per year) vs. band (left) and vs. band width (right)

2.2.3 Instrument response and degradation modelling [OLCI-L1B-CV-250]

2.2.3.1 Instrument response monitoring

2.2.3.1.1 OLCI-A

Figure 22 shows the gain coefficients of every pixel for two OLCI-A channels, Oa1 (400 nm) and Oa21 (1020 nm), highlighting the significant evolution of the instrument response since early mission.

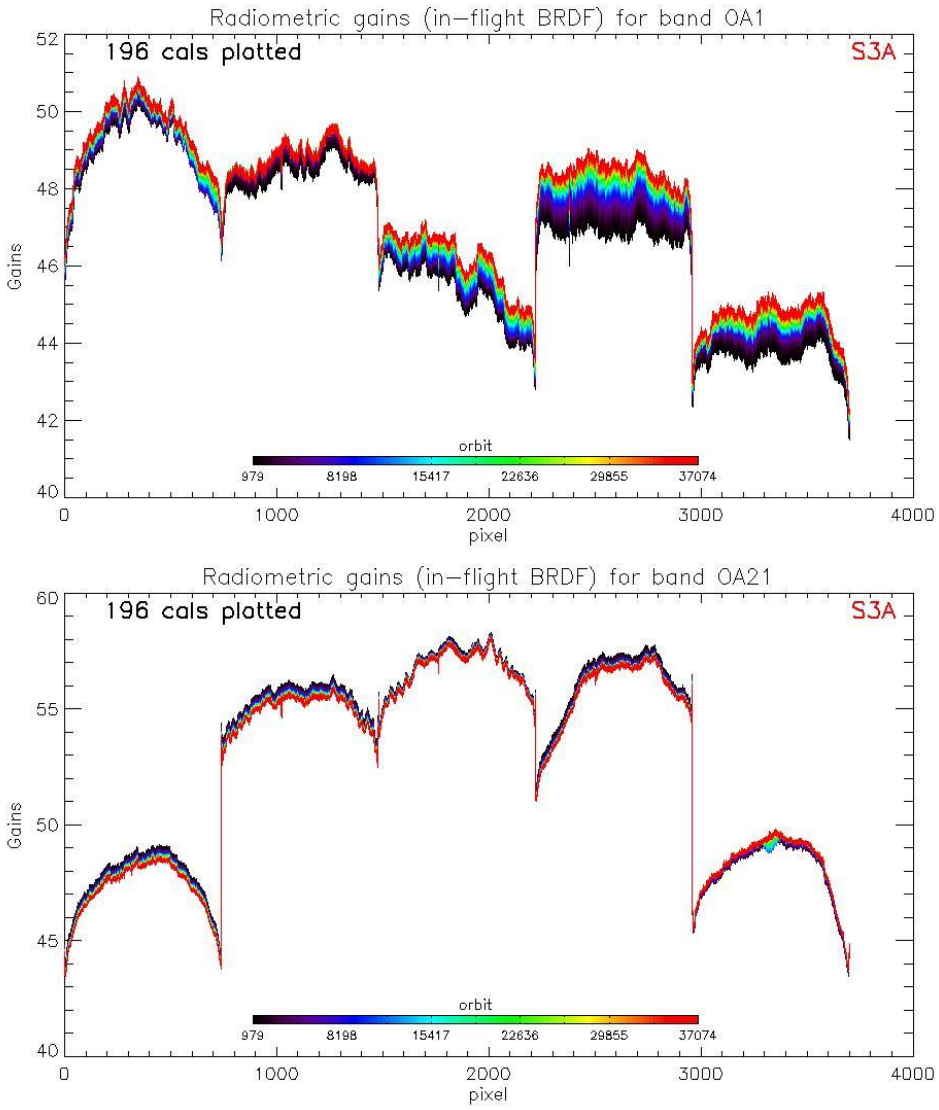

Figure 22: OLCI-A Gain Coefficients for band Oa1 (top) and Oa21 (bottom), derived using the in-flight BRDF model. The dataset is made of all diffuser 1 radiometric calibrations since orbit 979.

Figure 23 displays a summary of the time evolution of the cross-track average of the gains (in-flight BRDF, taking into account the diffuser ageing), for each module, relative to a given reference calibration (the 25/04/2016, change of OLCI channel settings). It shows that, if a significant evolution occurred during the early mission, the trends tend in general to stabilize, with some exceptions (e.g. band 1 of camera 1 and 4, bands 2 & 3 of camera 5).

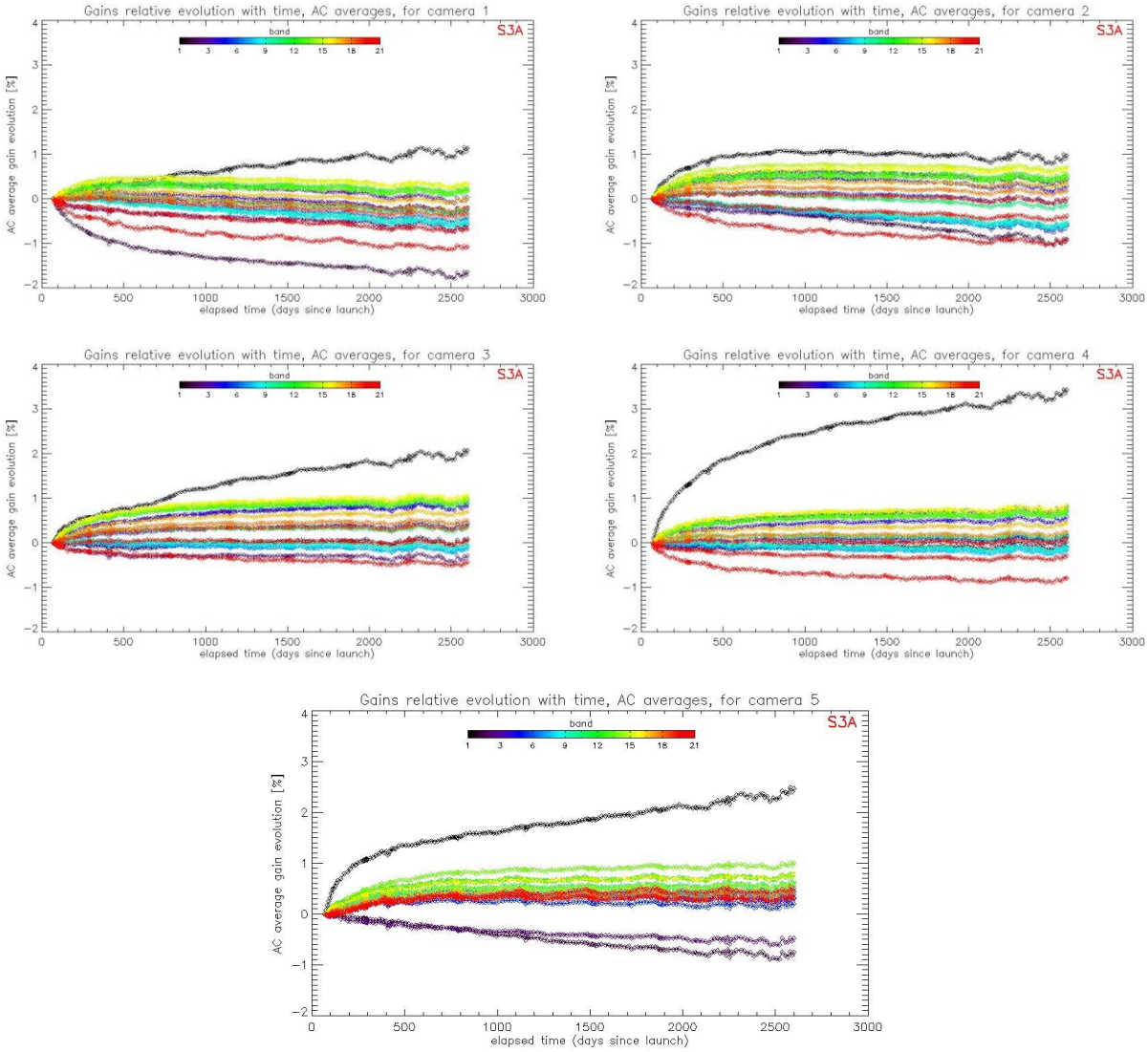

Figure 23: camera averaged gain relative evolution with respect to calibration of 25/04/2016 (change of OLCI channel settings), as a function of elapsed time since the beginning of the mission; one curve for each band (see colour code on plots), one plot for each module. The diffuser ageing is taken into account.

2.2.3.1.2 OLCI-B

Figure 24 shows the gain coefficients of every pixel for two OLCI-B channels, Oa1 (400 nm) and Oa21 (1020 nm), highlighting the significant evolution of the instrument response since early mission.

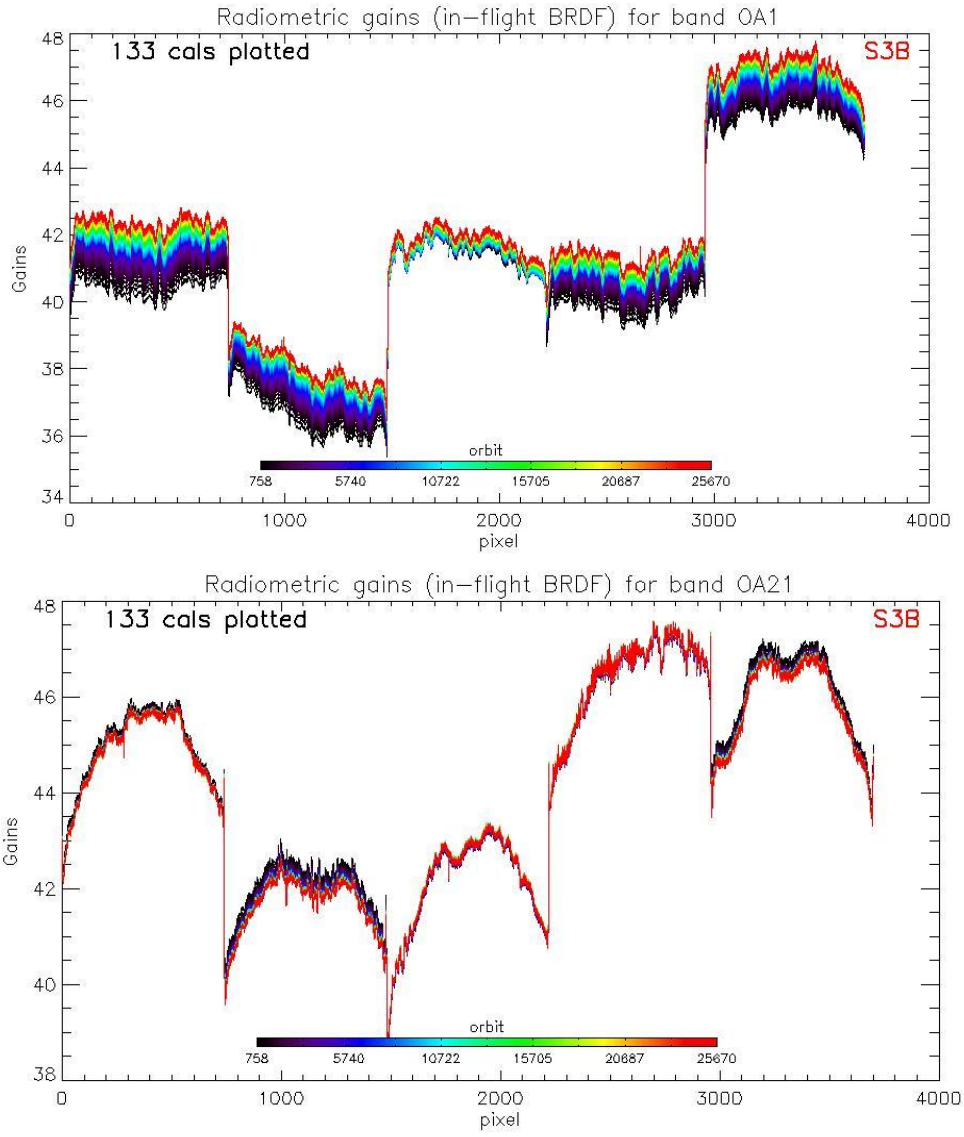

Figure 24: OLCI-B Gain Coefficients for band Oa1 (top) and Oa21 (bottom), derived using the in-flight BRDF model. The dataset is made of all diffuser 1 radiometric calibrations since orbit 758.

Figure 25 displays a summary of the time evolution of the cross-track average of the gains (in-flight BRDF, taking into account diffuser ageing), for each module, relative to a given reference calibration (first calibration after channel programming change: 18/06/2018). It shows that, if a significant evolution occurred during the early mission, the trends tend to stabilize. The large amount of points near elapsed time = 220 days is due to the yaw manoeuvre campaign. The slight discontinuity near "day 920 since launch" is due to the upgrade of the Ageing model.

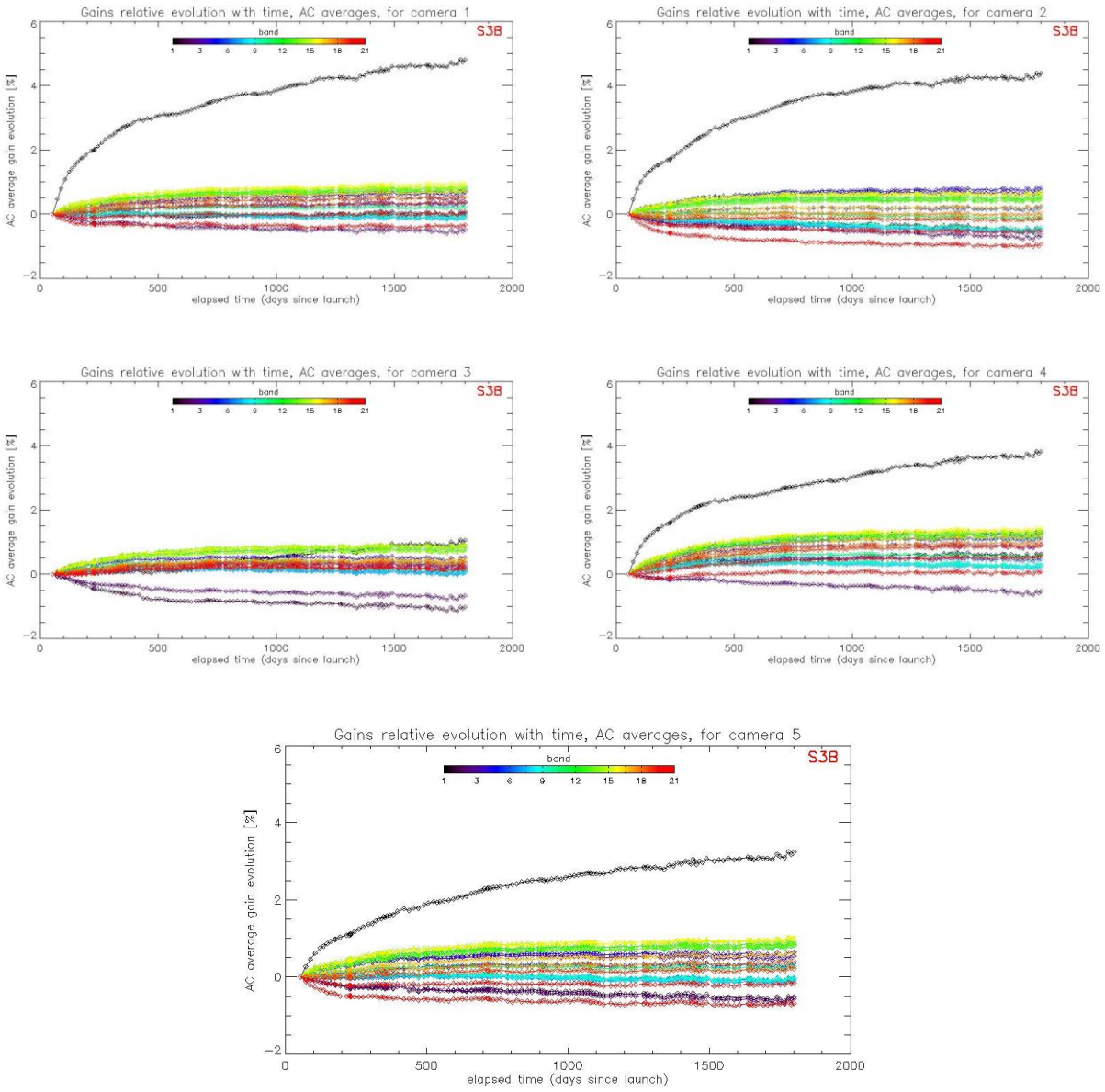

Figure 25: OLCI-B camera averaged gain relative evolution with respect to first calibration after channel programming change (18/06/2018), as a function of elapsed time since the beginning of the mission; one curve for each band (see colour code on plots), one plot for each module. The diffuser ageing is taken into account.

2.2.3.2 Instrument evolution modelling

2.2.3.2.1 OLCI-A

A new OLCI-A Radiometric Gain Model has been put in operations at PDGS the 19/07/2022 (Processing Baseline 3.09). This model has been derived on the basis of a more recent (compared to the previous model) Radiometric Calibration dataset, going from 23/10/2018 to 30/04/2022. It includes the correction of the diffuser ageing for the six bluest bands (Oa1 to Oa6) for which it is clearly measurable. The model performance over the complete dataset (including the 22 calibrations in extrapolation over about 11 months) remains better than about 0.1% for all bands at the exception of Oa01 which shows the presence of a strong peak near orbit 33000 reaching about 0.16%. This peak is also present for other bands but with a smaller amplitude. A slight drift of the model with respect to the most recent data seems to appear for all bands, despite the presence of this peak that makes it difficult to assess. The previous model, trained on a Radiometric Dataset limited to 03/10/2021, shows a clear drift of the model with respect to most recent data (Figure 27), that motivated the change. Comparison of the two figures shows the improvement brought by the updated model over almost all the mission. Performance shown on Figure 26 adopts, as for OLCI-B, the multiple model approach, i.e. different models (three for OLCI-A since PB, three for OLCI-B since PB 1.57) are used to cover the whole mission (red dashed line on Figure 26), each model being fitted on a partial dataset (green dashed line on Figure 26) whose coverage is optimized to provide best performance.

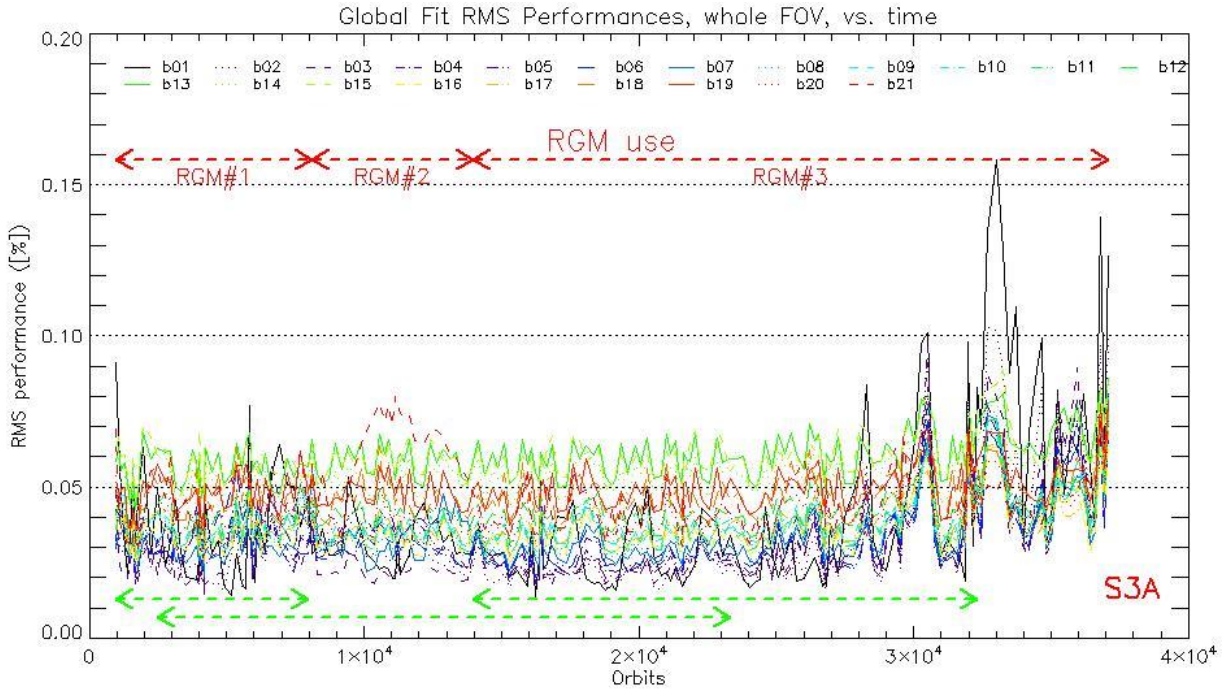

Figure 26: RMS performance of the OLCI-A Gain Model of the current processing baseline as a function of orbit.

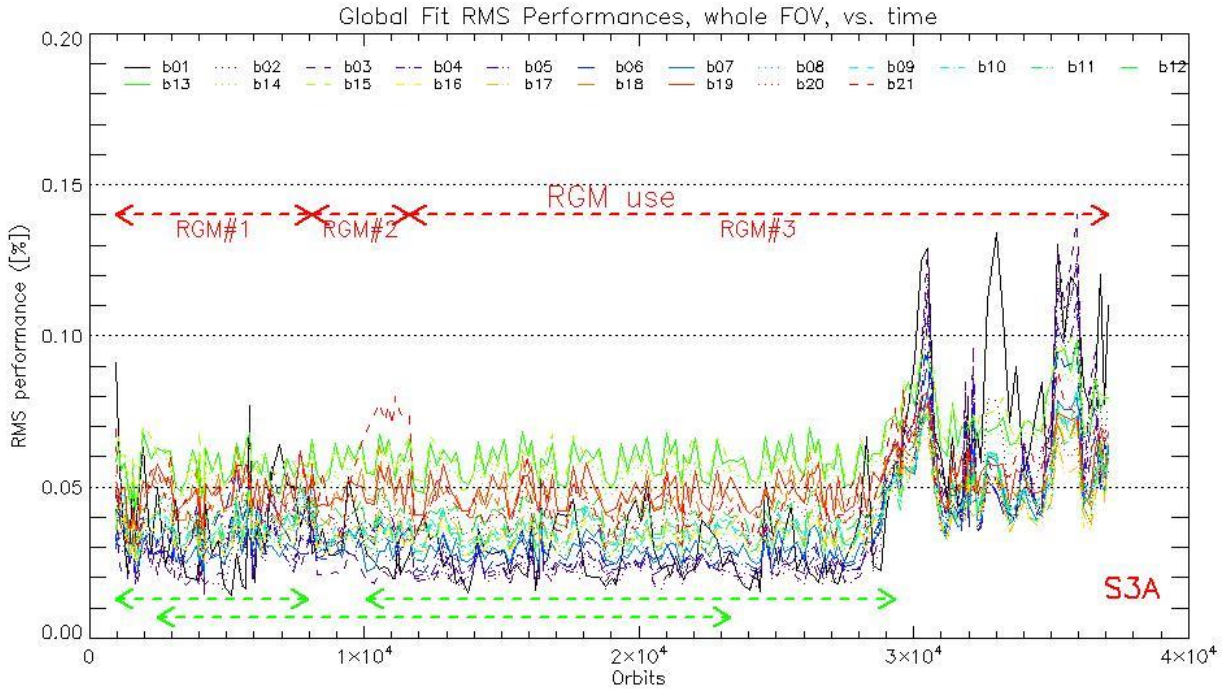

Figure 27: RMS performance of the OLCI-A Gain Model of the previous Processing Baseline as a function of orbit.

The overall instrument evolution since channel programming change (25/04/2016) is shown on Figure 28.

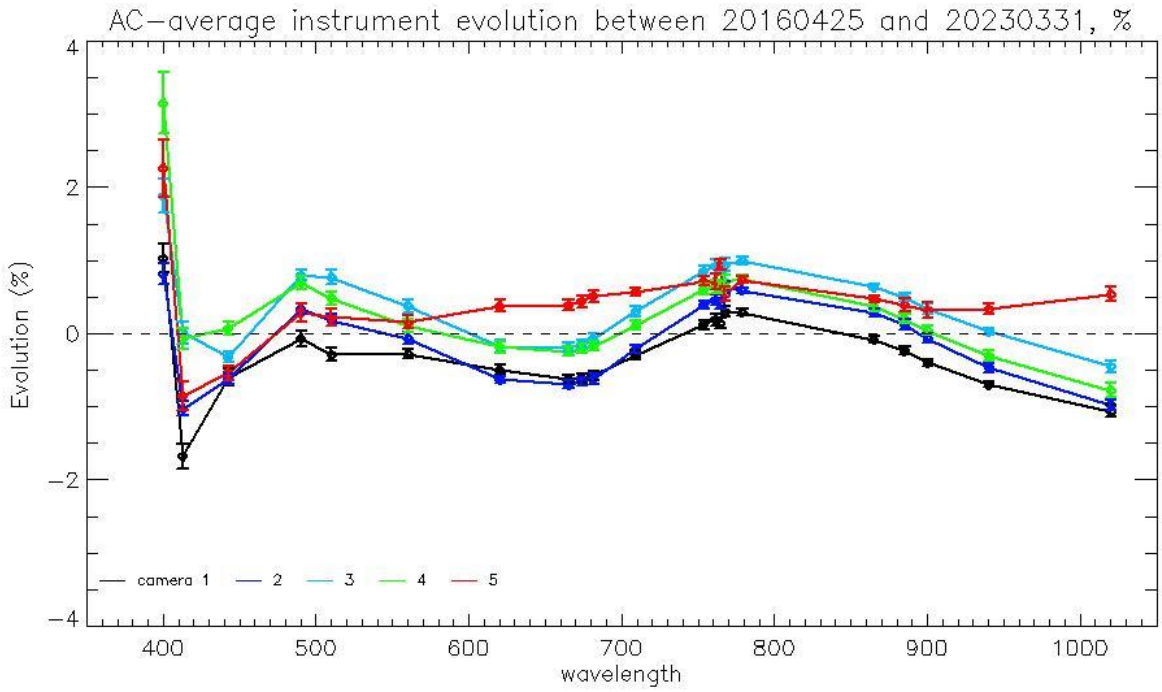

Figure 28: OLCI-A Camera-averaged instrument evolution since channel programming change (25/04/2016) and up to the most recent calibration (31/03/2023) versus wavelength.

The overall per camera performance, as a function of wavelength, and at each orbit is shown on Figure 29 as the average and standard deviation of the model over data ratio.

Finally, Figure 30 to Figure 32 show the detail of the model performance, with across-track plots of the model over data ratios at each orbit, one plot for each channel.

Comparisons of Figure 30 to Figure 32 with their counterparts in DQR of July 2022 clearly demonstrate the improvement brought by the new model whatever the level of detail.

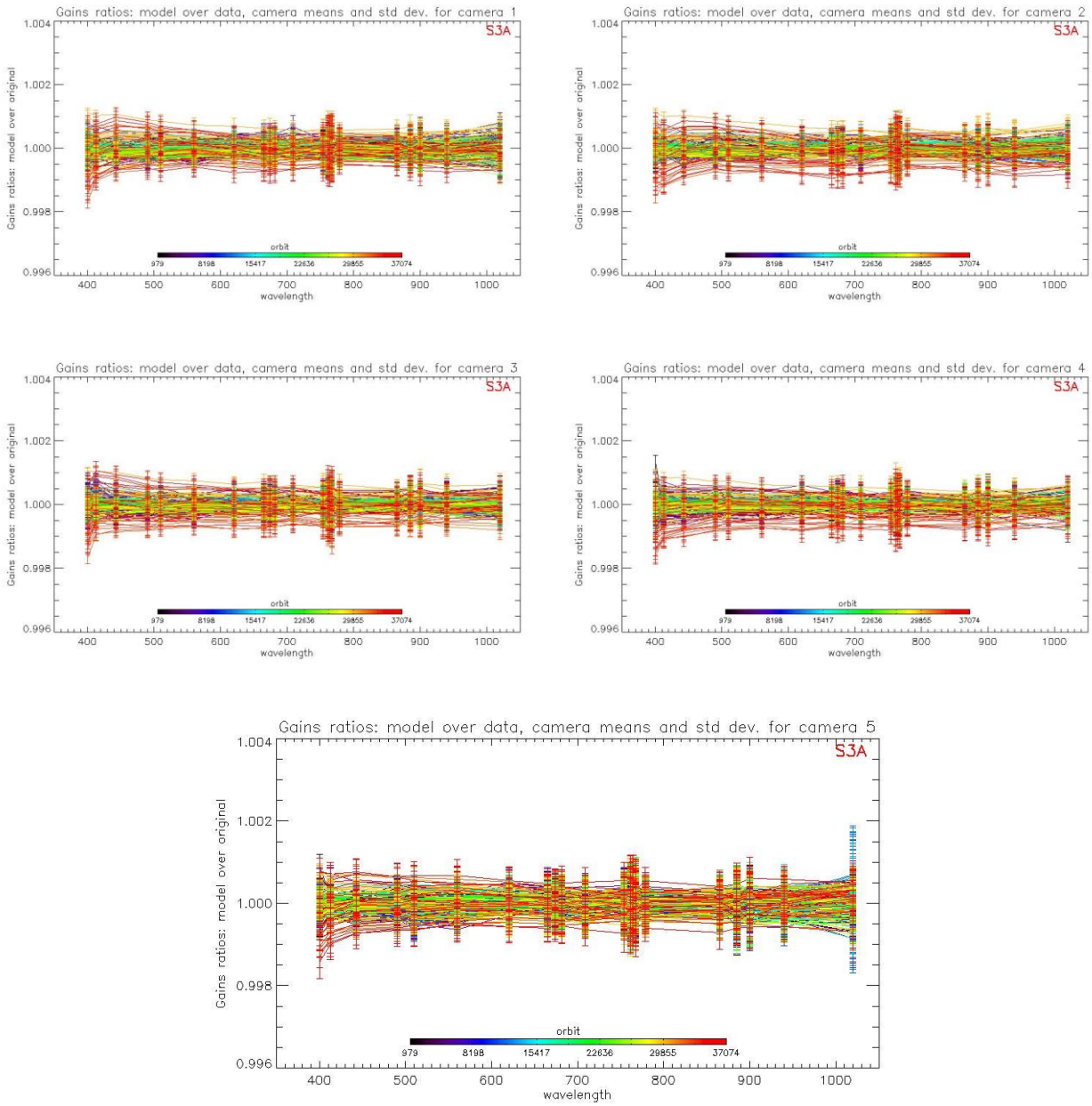

Figure 29: For the 5 cameras: OLCI-A Evolution model performance, as camera-average and standard deviation of ratio of Model over Data vs. wavelength, for each orbit of the test dataset, including 22 calibrations in extrapolation, with a colour code for each calibration from blue (oldest) to red (most recent).

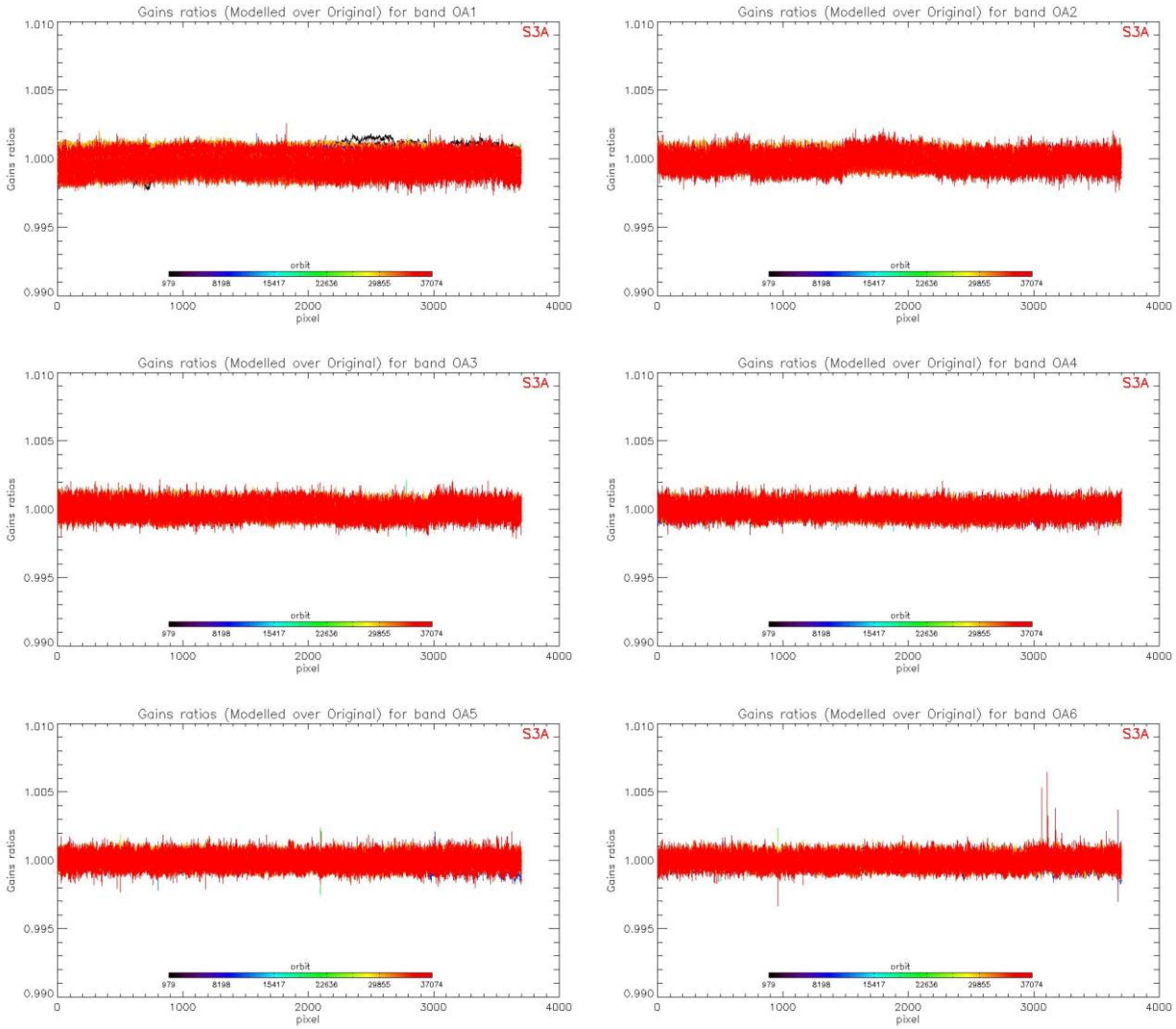

Figure 30: OLCI-A evolution model performance, as ratio of Model over Data vs. pixels, all cameras side by side, over the whole current calibration dataset (since instrument programming update), including 22 calibrations in extrapolation, channels Oa1 to Oa6.

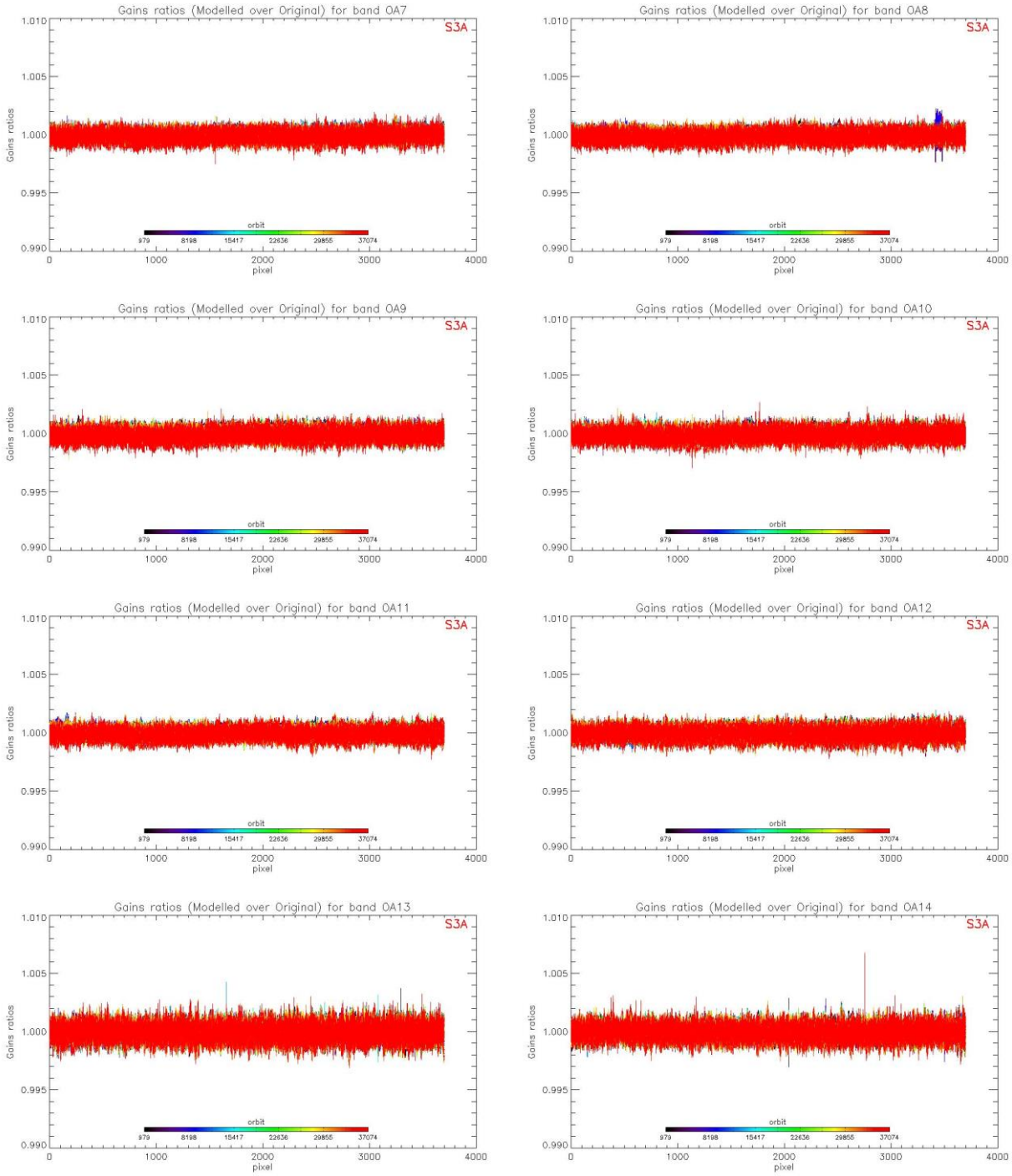

Figure 31: same as Figure 30 for channels Oa7 to Oa14.

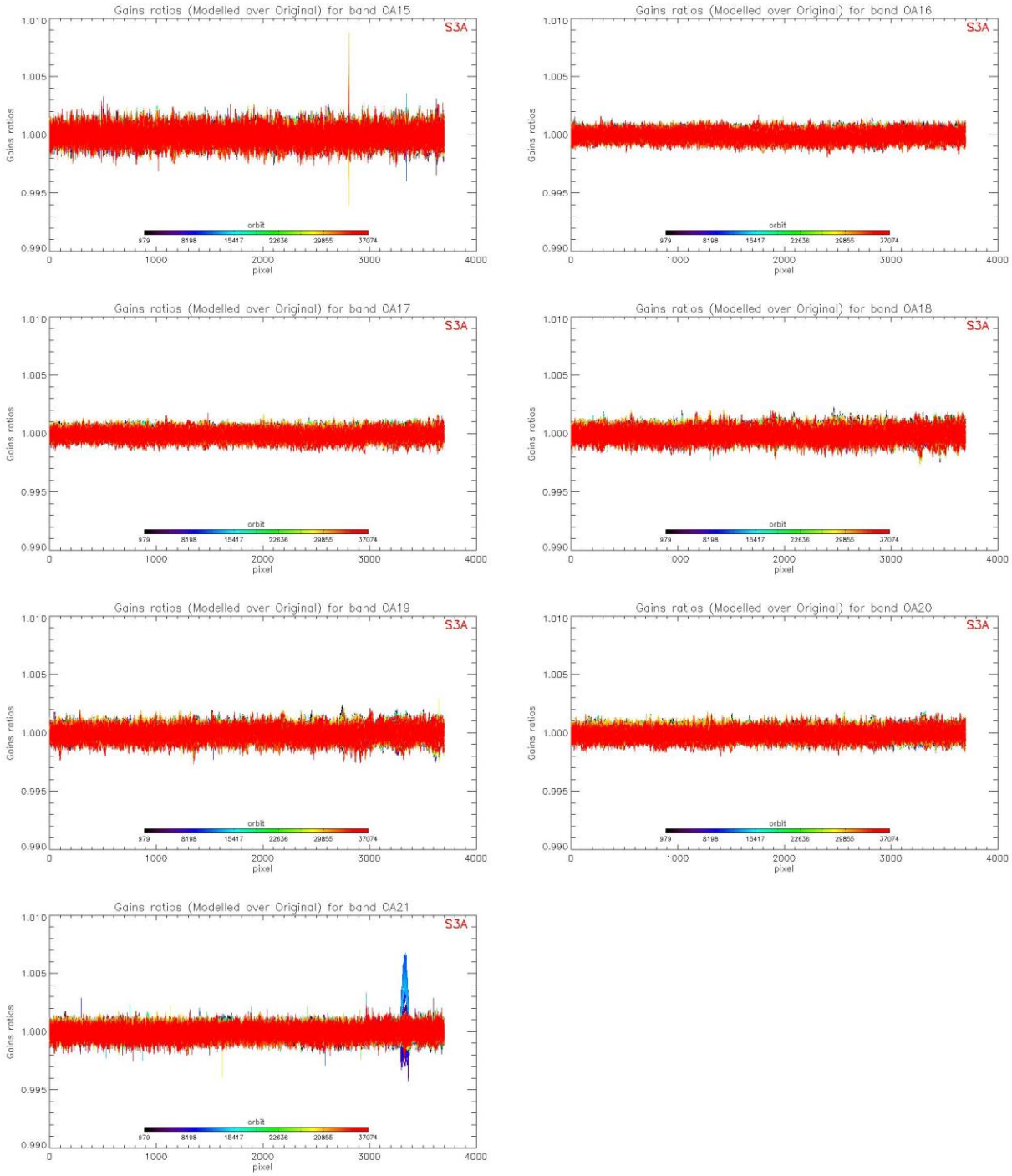

Figure 32: same as Figure 30 for channels Oa15 to Oa21.

2.2.3.2.2 OLCI-B

A new OLCI-B Radiometric Gain Model has been put in operations at PDGS on 19/07/2022 (Processing Baseline 3.09). This model has been derived on the basis of an extended Radiometric Calibration dataset (from 13/04/2019 to 29/04/2022). It includes the correction of the diffuser ageing for the five bluest bands (Oa1 to Oa5) for which it is clearly measurable. The model performance over the complete dataset (including 22 calibrations in extrapolation over about 11 months) is illustrated in Figure 33. It remains better than about 0.13% when averaged over the whole field of view for all bands. A slight drift of the model with respect to the most recent data seems to appear for all bands and a new Radiometric Gain Model has been trained on an extended data set but is not yet in operation. The previous model, trained on a Radiometric Dataset limited to 16/09/2021, shows a pronounced drift of the model with respect to most recent data, especially for band Oa01 (Figure 34). Comparison of the two figures shows the improvement brought by the updated Model over all the mission.

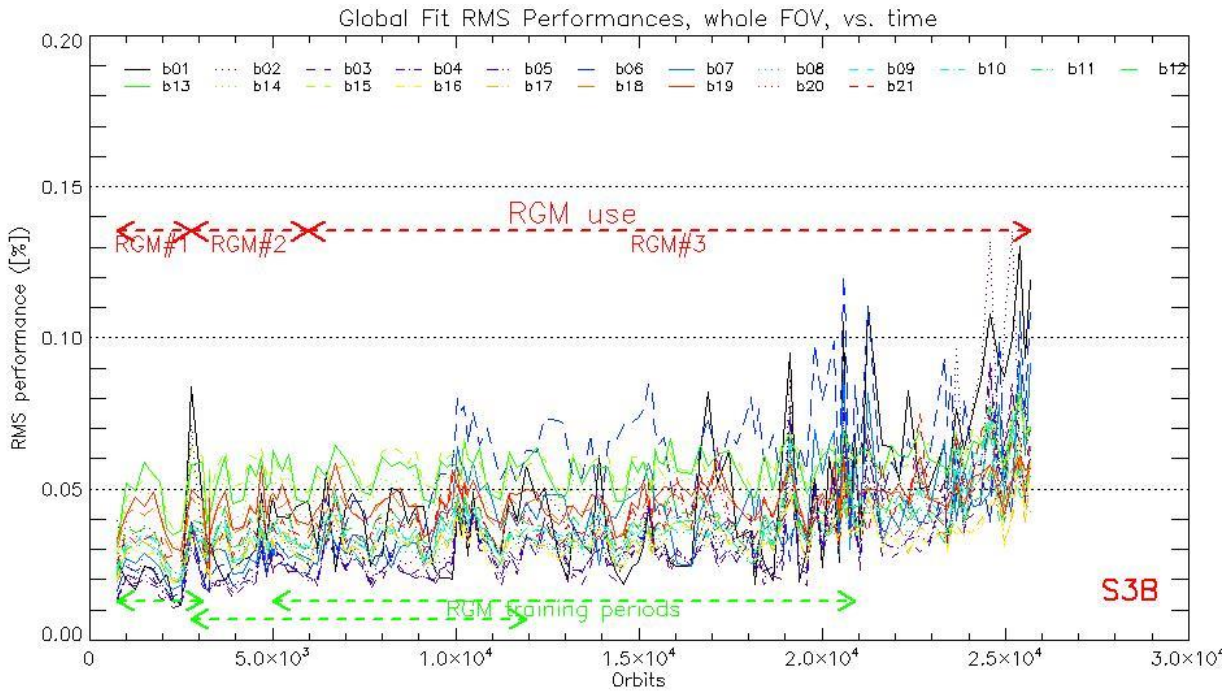

Figure 33: RMS performance of the OLCI-B Gain Model of the current processing baseline as a function of orbit.

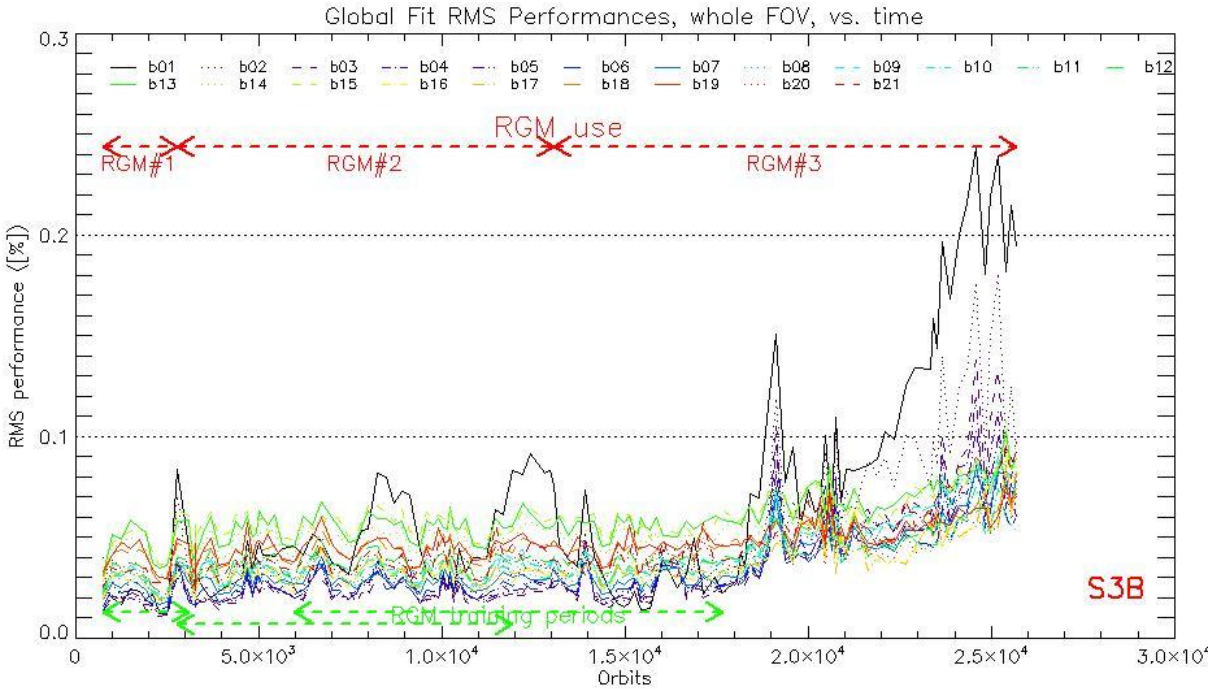

Figure 34: RMS performance of the OLCI-B Gain Model of the previous processing baseline as a function of orbit (please note the different vertical scale with respect to Figure 33).

The overall instrument evolution since channel programming change (18/06/2018) is shown on Figure 35.

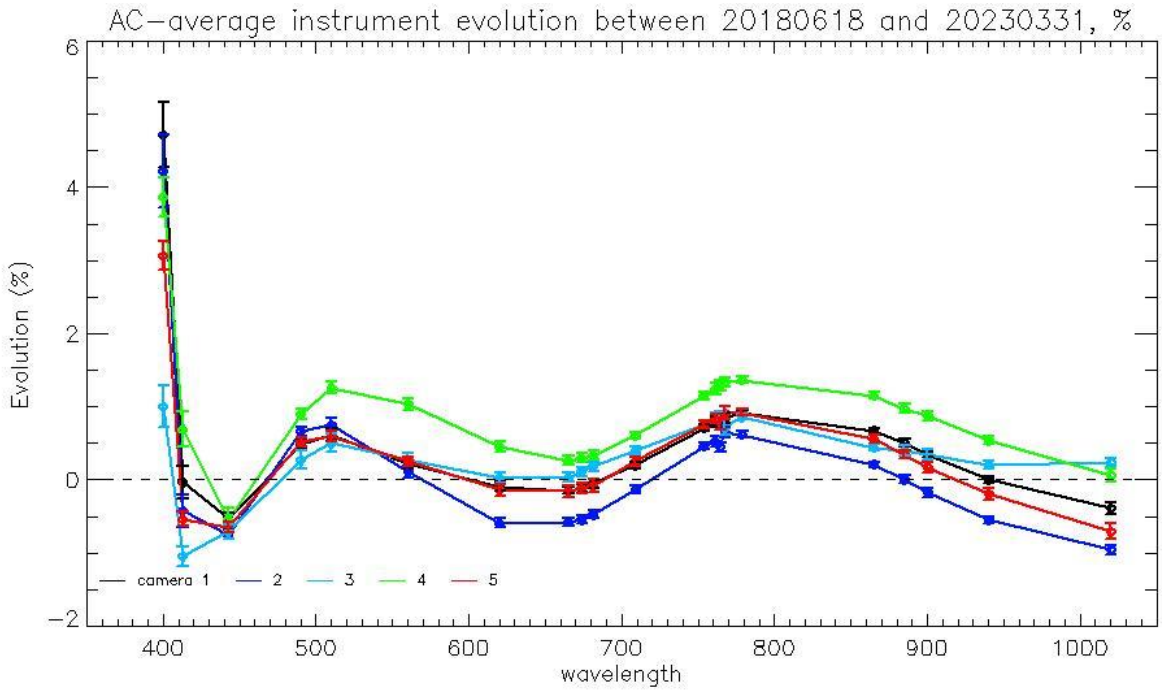

Figure 35: OLCI-B Camera-averaged instrument evolution since channel programming change (18/06/2018) and up to most recent calibration (31/03/2023) versus wavelength.

The overall per camera performance, as a function of wavelength, and at each orbit is shown on Figure 36 as the average and standard deviation of the model over data ratio.

Finally, Figure 37 to Figure 39 show the detail of the model performance, with across-track plots of the model over data ratios at each orbit, one plot for each channel.

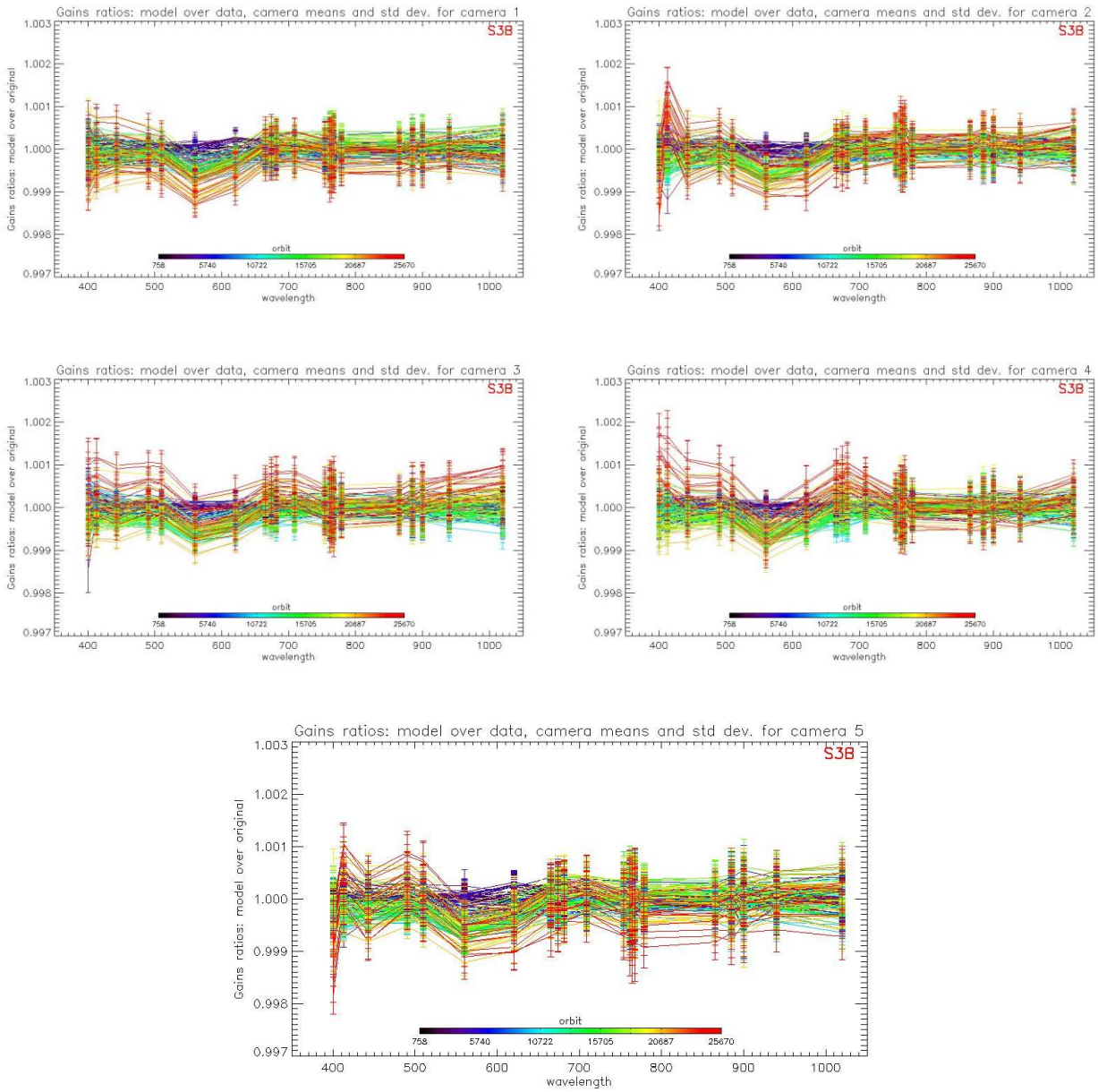

Figure 36: For the 5 cameras: OLCI-B Evolution model performance, as camera-average and standard deviation of ratio of Model over Data vs. wavelength, for each orbit of the test dataset, including 22 calibrations in extrapolation, with a colour code for each calibration from blue (oldest) to red (most recent).

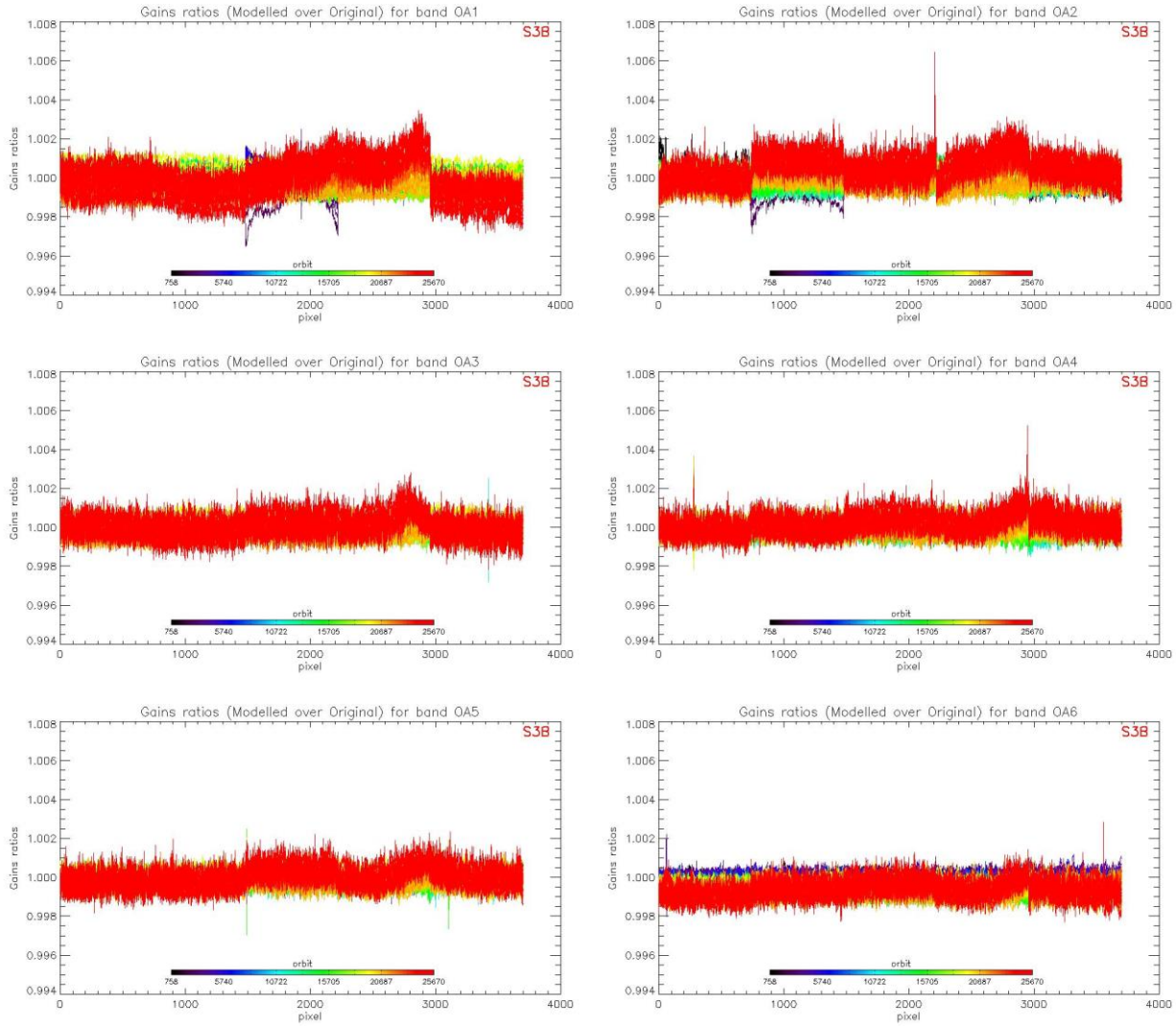

Figure 37: OLCI-B evolution model performance, as ratio of Model over Data vs. pixels, all cameras side by side, over the whole current calibration dataset (since instrument programming update), including 22 calibrations in extrapolation, channels Oa1 to Oa6.

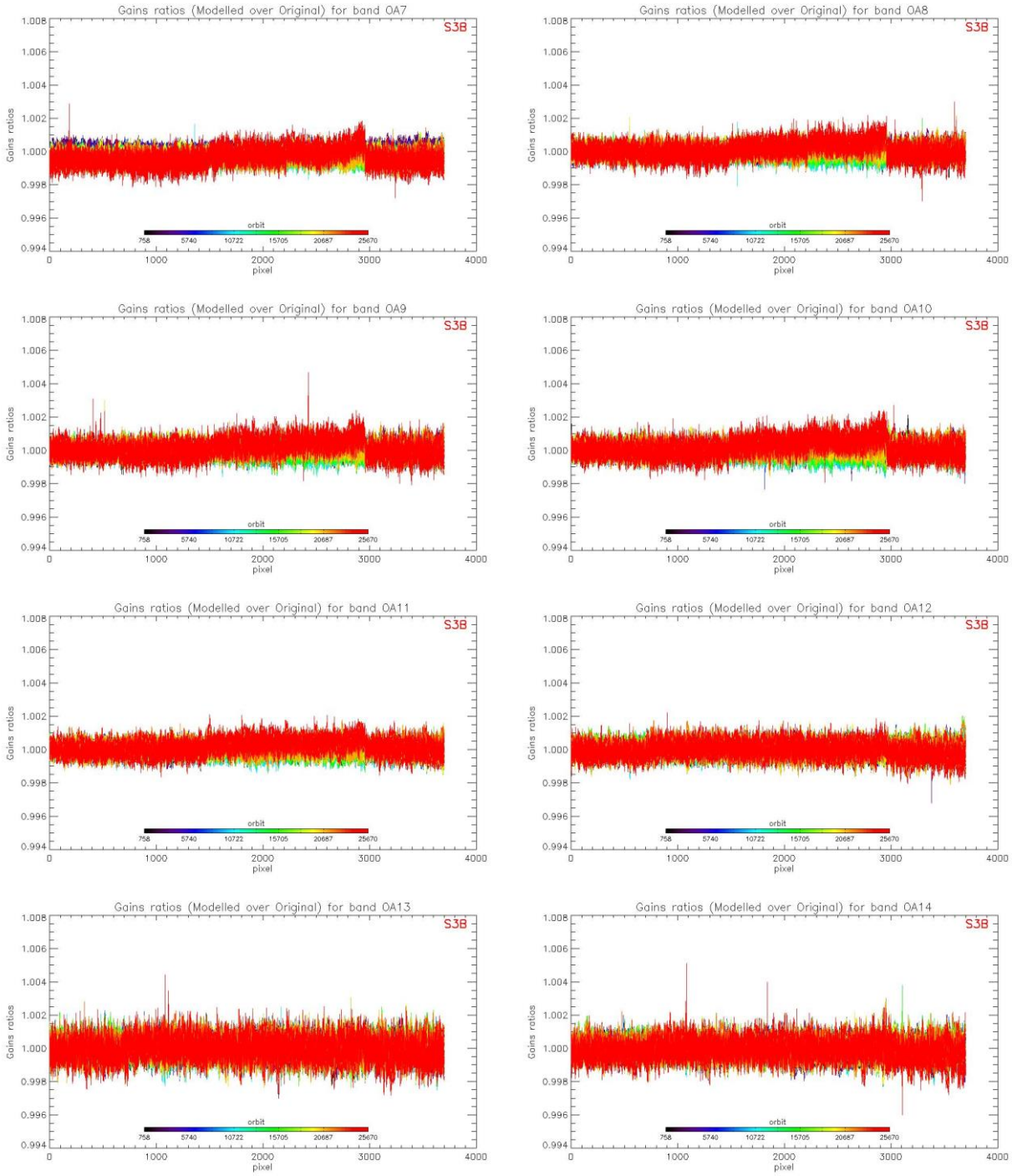

Figure 38: same as Figure 37 for channels Oa7 to Oa14.

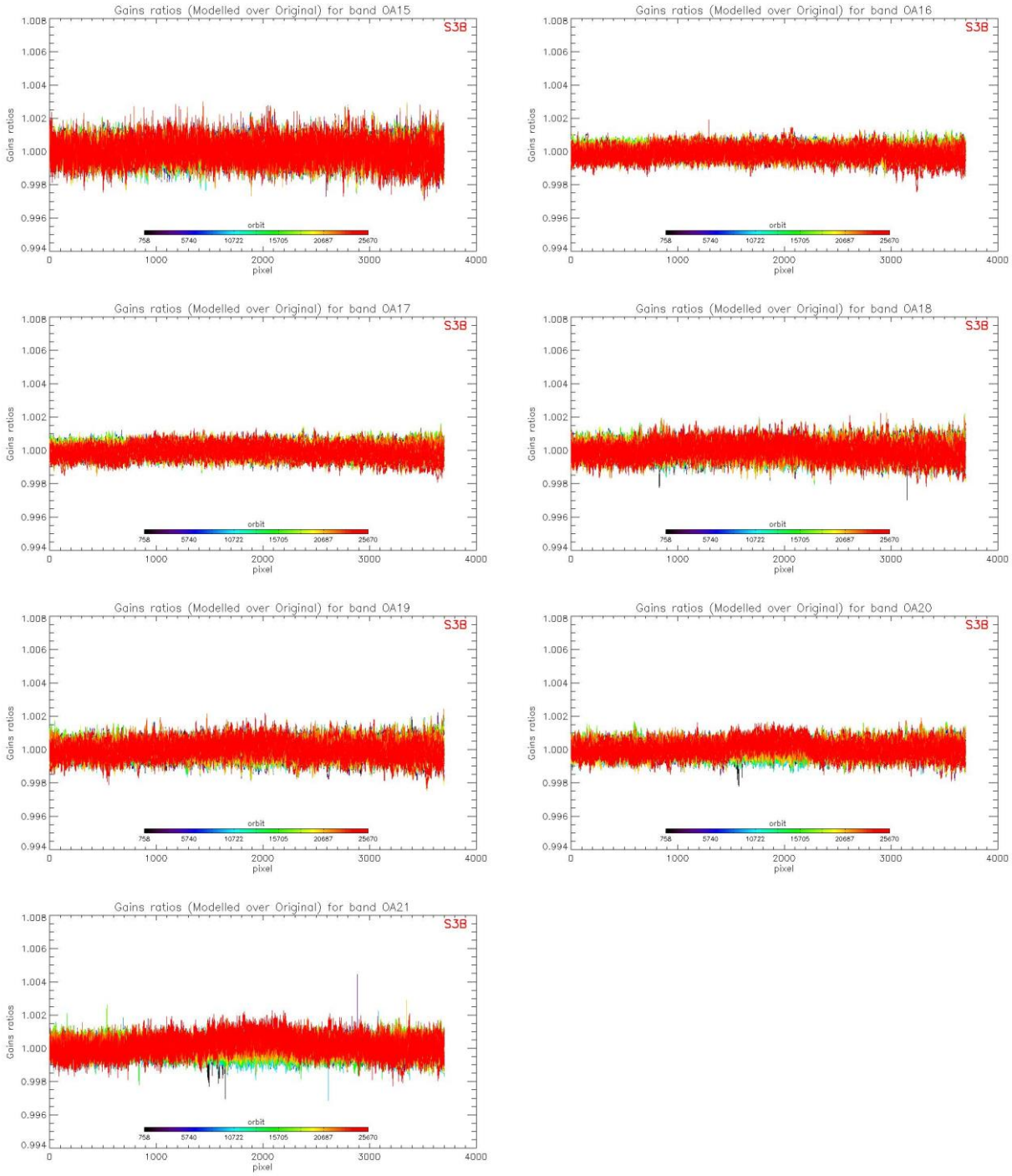

Figure 39: same as for channels Oa15 to Oa21.

2.2.4 Ageing of nominal diffuser [OLCI-L1B-CV-240]

2.2.4.1 OLCI-A

There has been one calibration sequence S05 (reference diffuser) for OLCI-A during the current reported period:

- S05 sequence (diffuser 2) on 31/03/2023 20:27 to 20:29 (absolute orbit 37075)

With the associated S01 sequence (nominal diffuser) in order to compute ageing:

- S01 sequence (diffuser 1) on 31/03/2023 18:46 to 18:48 (absolute orbit 37074)

The diffuser 1 Ageing is computed for each 3700 detector and each spectral band by formula:

Ageing(orb)=G1(orb)/G2(orb)- G1(orb_ref)/G2(orb_ref)

Where:

- G1 is the diffuser 1 (= nominal diffuser) Gain coefficients
- G2 is the diffuser 2 (= reference diffuser) Gain coefficients
- orb_ref is a reference orbit chosen at the beginning of the mission

Ageing is represented in Figure 40 for band Oa01 and in Figure 41 for band Oa17. The negative shift of the sequence at orbit 5832 (for which a slight increase would be expected instead) is not explained so far and still under investigation. It should be noted that the corresponding orbit of diffuser 1 (nominal) has also been detected as an outlier in the modelling of the radiometric long-term trend with an unexpected excess of brightness.

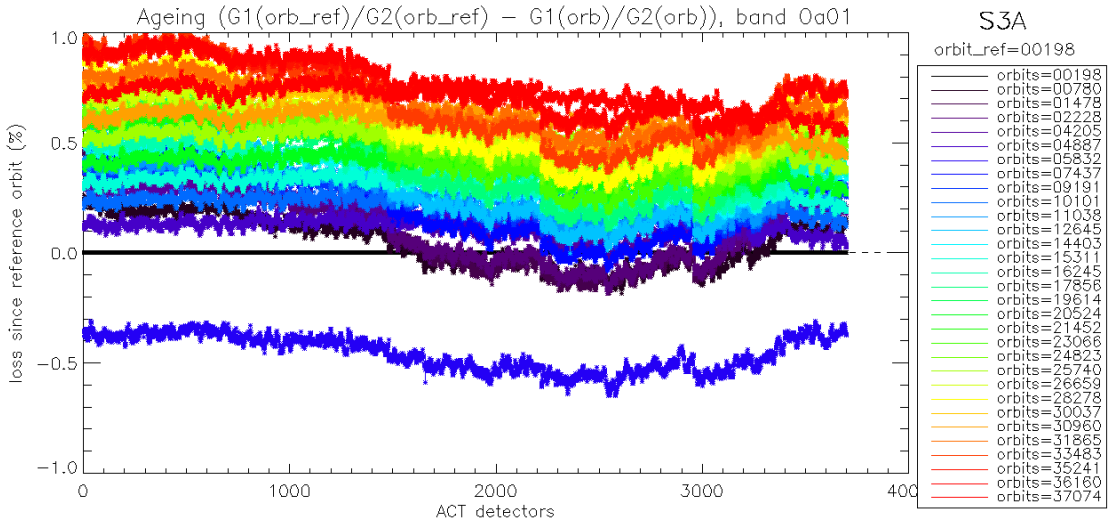

Figure 40: diffuser 1 ageing for spectral band Oa01. We see strong ACT low frequency structures that are due to residual of BRDF modelling.

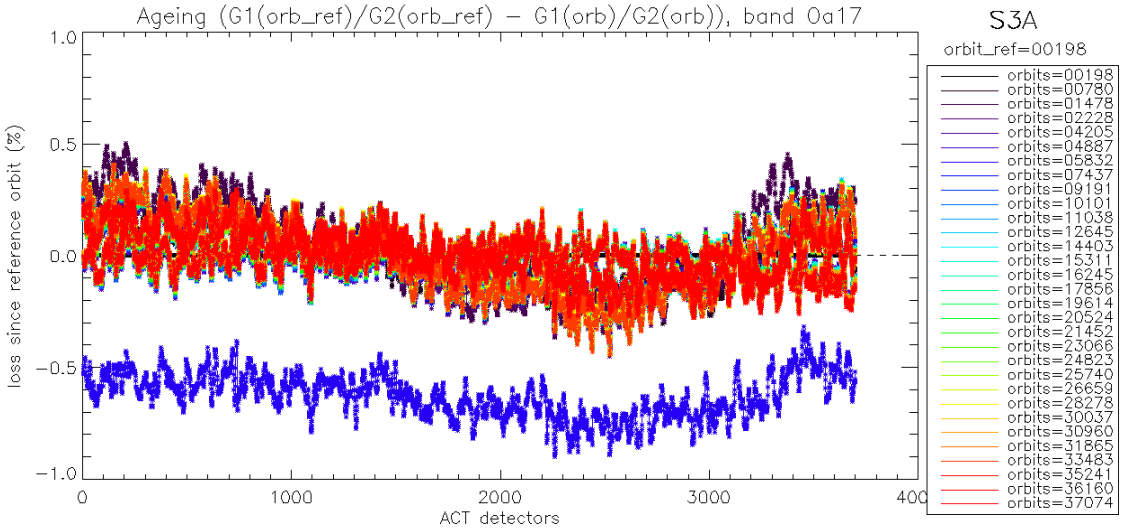

Figure 41: same as Figure 40 for spectral band Oa17. We use this band in order to normalize other bands and remove the ACT structures due to residual of BRDF modelling. Normalized curve for spectral band Oa01 is presented in Figure 42.

Figure 40 and Figure 41 show that the Ageing curves are impacted by a strong ACT pattern which is due to residuals of the bad modelling (on-ground) of the diffuser BRDF. This pattern is dependant of the azimuth angle. It is a 'white' pattern which means it is the same for all spectral bands. As such, we can remove this pattern by normalizing the ageing of all bands by the curve of band Oa17 which is expected not to be impacted by ageing because in the red part of the spectrum. We use an ACT smoothed version (window of 100 detectors) of band Oa17 in order to reduce the high frequency noise. Normalized ageing for spectral band Oa01 is represented in Figure 42 where we can see that this band is impacted by ageing of the diffuser.

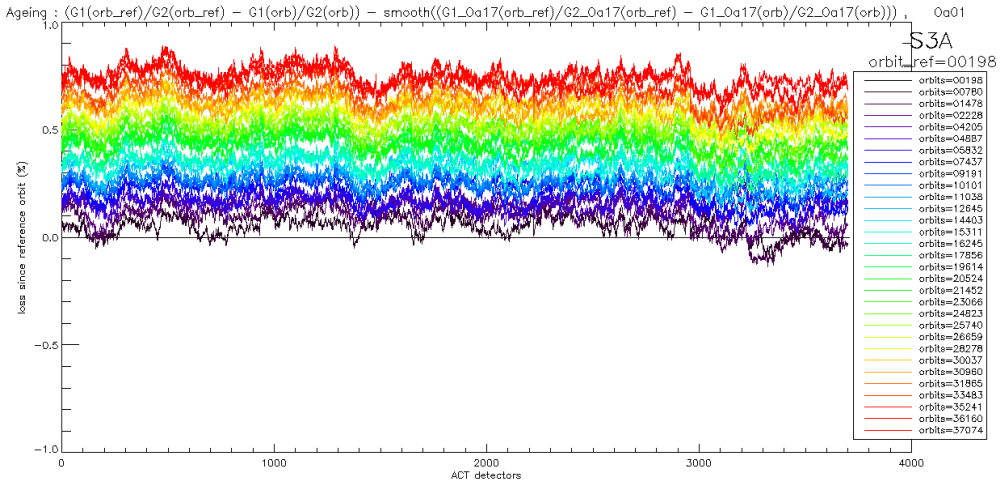

Figure 42: same as Figure 40 after normalization by band Oa17. Ageing of the diffuser 1 is now visible in the 5 cameras.

Camera averaged ageing (normalized by band Oa17) as a function of wavelength is represented in Figure 43 where we can see that ageing is stronger in the 'bluest' spectral bands (short wavelengths). Ageing is clearly visible only for the 6 first spectral bands so far in the OLCI mission life.

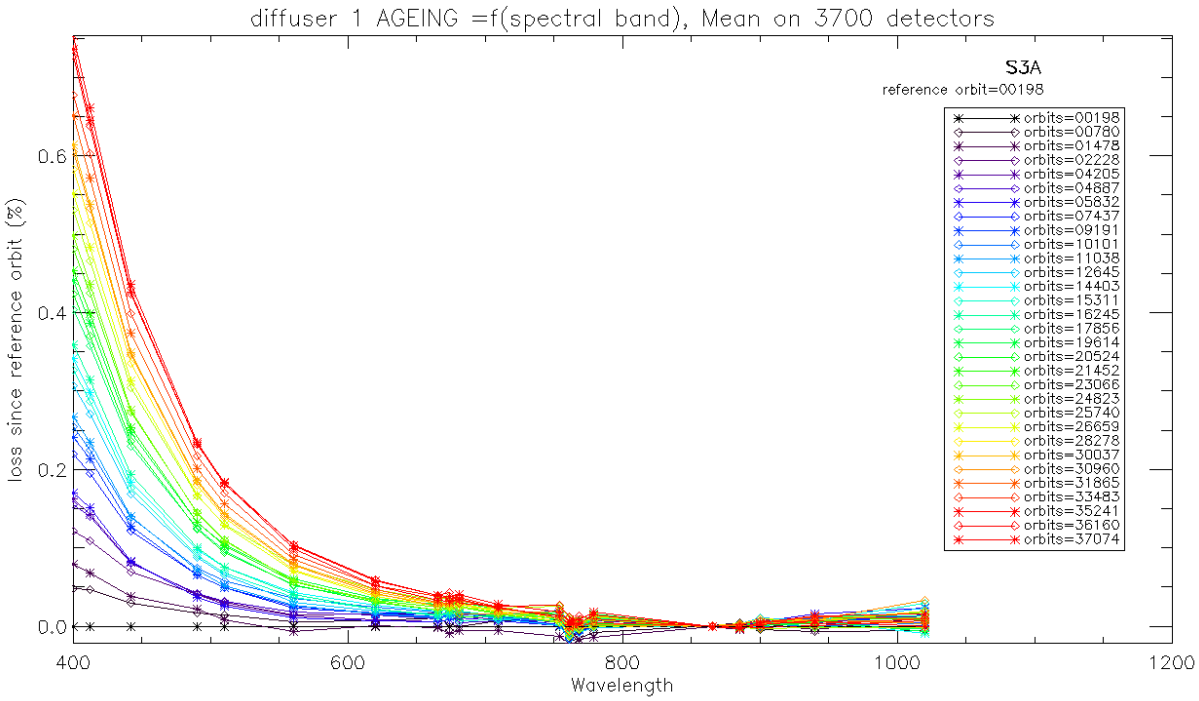

Figure 43: Diffuser 1 ageing as a function of wavelength (or spectral band). Ageing is clearly visible in spectral band #1 to #6. Note that all ageing sequences are plotted but in order to fit in the figure the box legend only displays 1 ageing sequence over 2 (including the most recent one).

Figure 44 shows the evolution, for spectral band Oa01, of the 5 cameras averaged ageing as a function of time.

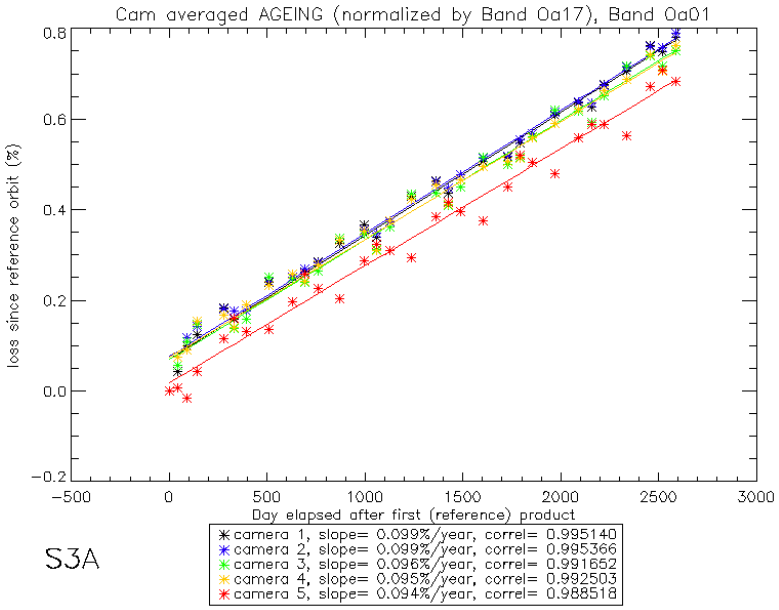

Figure 44: Camera averaged ageing for band Oa01 (normalized by band Oa17) as a function of elapsed time. Linear fit for each camera is plotted. The slope (% loss per year) and the correlation coefficient.

A model of diffuser ageing as a function of cumulated exposure time (i.e. number of acquisition sequence on nominal diffuser, regardless of the band setting) has been built and is described in Cyclic #23 Report. The results of this model confirm the need to model ageing against cumulated exposure rather than elapsed time, as it provides a more linear trend, even if not perfect (see Figure 21 of Cyclic #23 Report).

The slope of this ageing model (% of loss per exposure) as a function of wavelength is presented in Figure 45).

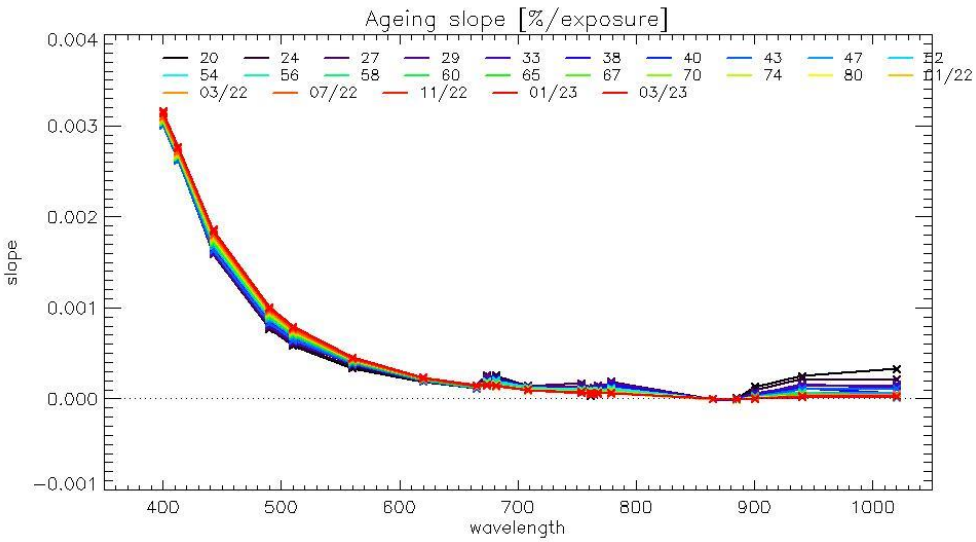

Figure 45: Slope of ageing fit (% of loss per exposure) vs wavelengths, using all the available ageing sequence at the time of the current reporting period (red curve) and at the time of previous reporting periods for which an ageing sequence was measured (see legend within the figure).

In Figure 45, we see that the Ageing slopes have not significantly changed between the current reporting period and the last 24 reporting periods containing a S05 sequence (month #202303, #202211, #202207, #202203, #202201, cycles #80, #74, #70, #67, #65, #60, #56, #58, #54, #52, #47, #43, #40, #38, #33, #29, #27, #24 and #20). Cycle #47 has been used to derive the Ageing Correction model used for the currently operational Gain Model. The exposure time dependent ageing model is used to derive the Gain Model, the most recent version of which has been put in operations in PDGS on 18th November 2021 (Processing Baseline 3.01).

2.2.4.2 OLCI-B

There has been one calibration sequence S05 (reference diffuser) for OLCI-B during acquisition Cycle 63:

- S05 sequence (diffuser 2) on 31/03/2023 04:39 to 04:41 (absolute orbit 25672)

with the associated S01 sequence in order to compute ageing:

- S01 sequence (diffuser 1) on 31/03/2023 02:58 to 03:00 (absolute orbit 25671)

The diffuser 1 Ageing is computed for each 3700 detector and each spectral band by formula:

Ageing(orb)=G1(orb)/G2(orb)- G1(orb_ref)/G2(orb_ref)

Where:

- G1 is the diffuser 1 (= nominal diffuser) Gain coefficients
- G2 is the diffuser 2 (= reference diffuser) Gain coefficients
- orb_ref is a reference orbit chosen at the beginning of the mission

Ageing is represented in Figure 46 for band Oa01 and in Figure 47 for band Oa17.

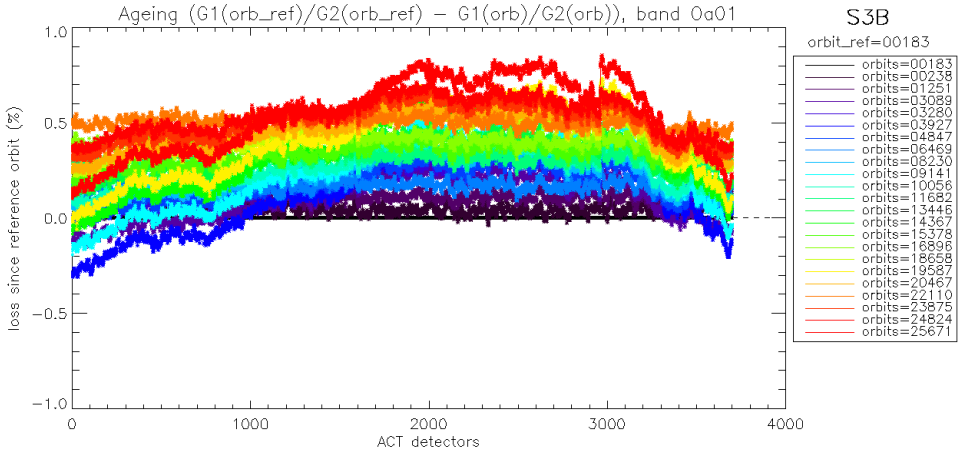

Figure 46: OLCI-B diffuser 1 ageing for spectral band Oa01. We see strong ACT low frequency structures that are due to residual of BRDF modelling.

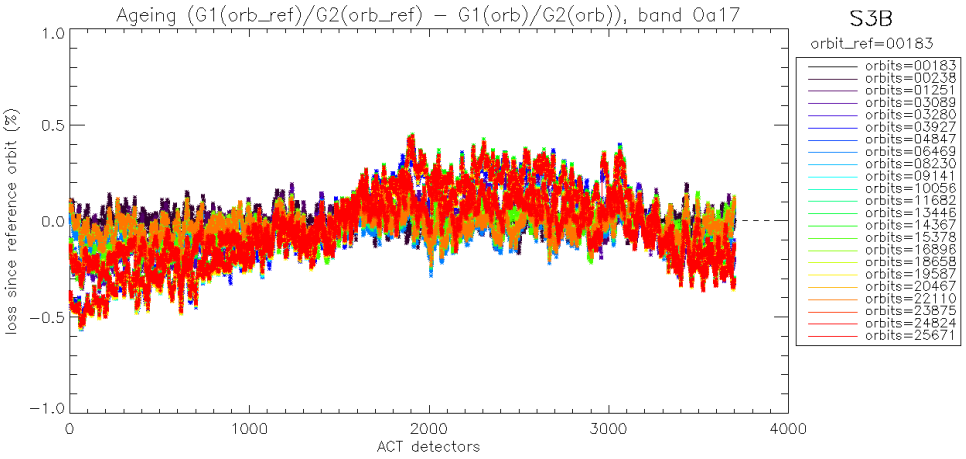

Figure 47: same as Figure 46 for spectral band Oa17. We use this band in order to normalize other bands and remove the ACT structures due to residual of BRDF modelling. Normalized curve for spectral band Oa01 is presented in Figure 48.

Figure 46 and Figure 47 show that the Ageing curves are impacted by a strong ACT pattern which is due to residuals of the bad modelling (on-ground) of the diffuser BRDF. This pattern is dependant of the azimuth angle. It is a 'white' pattern which means it is the same for all spectral bands. As such, we can remove this pattern by normalizing the ageing of all bands by the curve of band Oa17 which is expected not to be impacted by ageing because in the red part of the spectrum. We use an ACT smoothed version (window of 100 detectors) of band Oa17 in order to reduce the high frequency noise. Normalized ageing for spectral band Oa01 is represented in Figure 48 where we can see that this band is impacted by ageing of the diffuser.

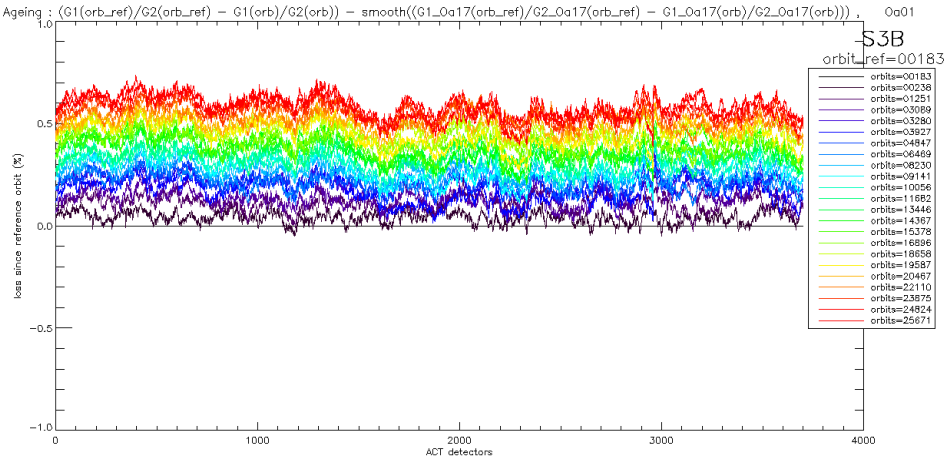

Figure 48: same as Figure 46 after normalization by band Oa17. Ageing of the diffuser 1 is now visible in the 5 cameras.

Camera averaged ageing (normalized by band Oa17) as a function of wavelength is represented in Figure 49 where we can see that ageing is stronger in the 'bluest' spectral bands (short wavelengths). Ageing is clearly visible only for the 5 first spectral bands so far in the OLCI-B mission life. We see a bump around 680 nm which is probably due to characterisation errors that are strongly geometry dependant and affect differently the various camera.

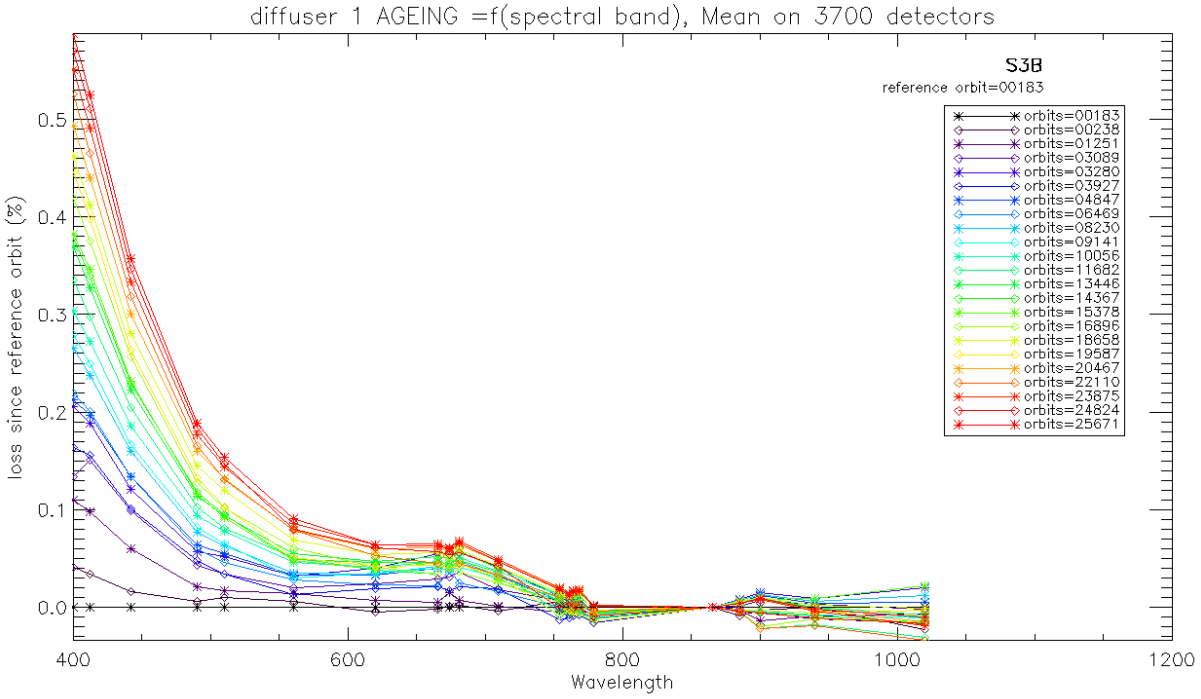

Figure 49: OLCI-B Diffuser 1 ageing as a function of wavelength (or spectral band). Ageing is clearly visible in spectral band #1 to #5.

As for OLCI-A, the OLCI-B Diffuser Ageing has been modelled as a function of cumulated exposure time (i.e. number of acquisition sequence on nominal diffuser, regardless of the band setting). The OLCI-A modelling methodology has been applied to OLCI-B. The results of this modelling, iterated at each new Ageing Sequence acquisition, expressed as the rate of ageing (% of loss per exposure) as a function of wavelength is presented in Figure 50.

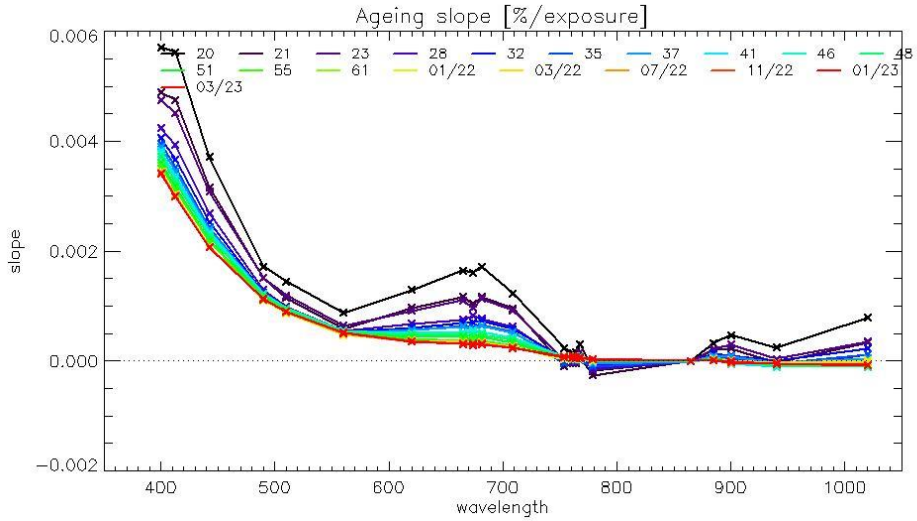

Figure 50: Slope of ageing fit (% of loss per exposure) vs wavelengths, using all the available ageing sequence at the time of the current reporting period (red curve) and at the time of previous reporting periods for which an ageing sequence was measured (see legend within the figure).

The general behaviour of the ageing assessment strongly differs to that of OLCI-A (Figure 45) in two ways: variability with time is much higher and the spectral shape is not as expected. This is interpreted as an unexpected dependency of the *ratio* of diffusers BRDF with illumination conditions. This justified the used of an alternative method using direct comparisons of two nominal diffuser observations, acquired under the same geometry (i.e. directly comparable) and the same day (i.e. with no significant instrument sensitivity evolution) but separated by 7 more exposures to light (during the Yaw Manoeuvres dedicated to the in-flight BRDF modelling). This is in theory the best ageing measurement but as composed of only one measure, it is subject to a large uncertainty. At the time it was derived, it showed a reliable spectral shape up to 850 nm and a good agreement with the nominal assessment in the blue (Figure 51), so that it was used until recently to derive the Radiometric Gain Models. It is referred to as the “YM model”.

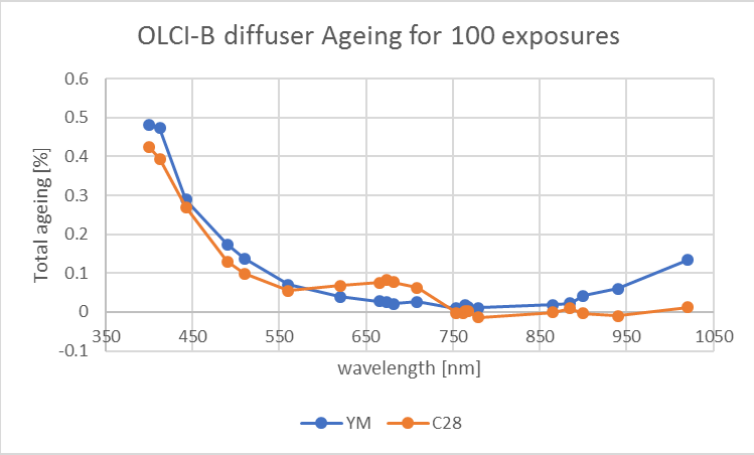

Figure 51: OLCI-B diffuser ageing (after 100 exposures, i.e. about two years) according to direct assessment from Yaw Manoeuvres (blue) and nominal method at Cycle 28 (orange).

The regular decrease of the ageing slopes according to the nominal method makes YM ageing model more and more overestimated, and a new method has been defined and presented in previous DQM. This method has been applied, including the latest ageing assessment mentioned above.

As the anomalous ageing estimated in the red have shown to be correlated with Sun illumination geometry, a reanalysis of the Ageing sequences has been done on sub-sets of sequences with equal or close illumination conditions. Once sorted by Sun azimuth angles, a set of 3 clusters (Figure 52) provide independent ageing estimates. The estimates quality can be inferred from in-FOV consistency, both inside each camera and between cameras, as the diffuser ageing is independent of the viewing direction. The final estimate is a weighted average of the clusters assessments.

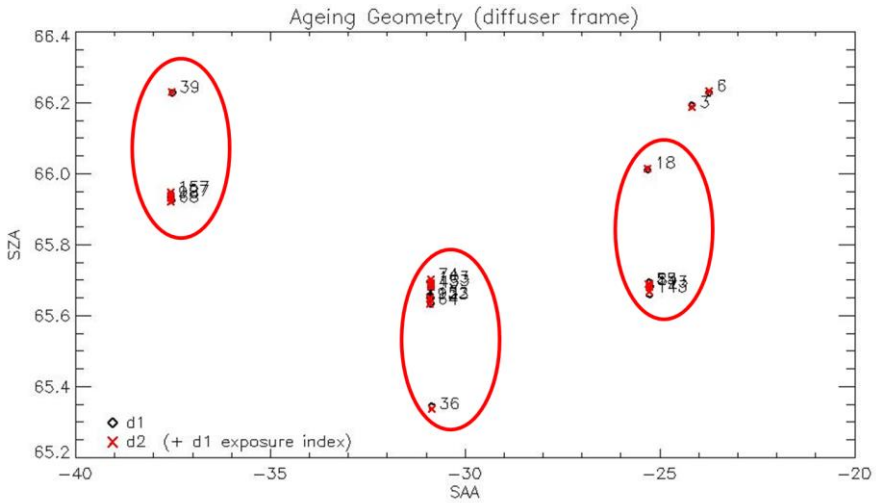

Figure 52: clustered Ageing sequences illumination geometries.

The results are quite satisfactory with good in-FOV consistency, well improved with respect to other methods, and a rather good inter-cluster consistency. The final results, together with those of the two other methods, are shown on Figure 53: the variation between the two Ageing slopes estimates of 20220331, 20221125 and 20230331 are extremely small.

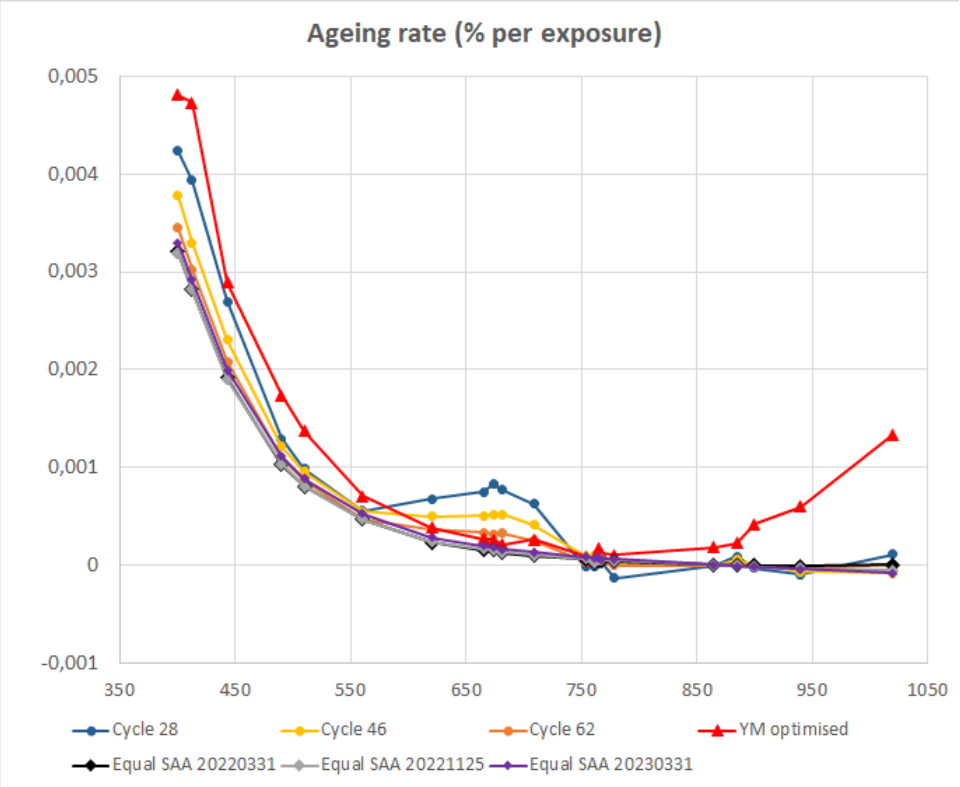

Figure 53: various estimates of the ageing rate, according to nominal method for cycles 28, 46 and 62, according to direct assessment during Yaw manoeuvres, and according to the Equal SAA clustering for data up to 03/2022, 11/2022 and 03/2023.

2.2.5 Updating of calibration ADF [OLCI-L1B-CV-260]

2.2.5.1 OLCI-A

No CAL_AX ADF has been delivered to PDGS during the report period for OLCI-A.

2.2.5.2 OLCI-B

No CAL_AX ADF has been delivered to PDGS during the report period for OLCI-B.

2.3 Spectral Calibration [OLCI-L1B-CV-400]

2.3.1 OLCI-A

There was no S02+S03 nor S09 Spectral Calibration for OLCI-A in the reporting period.

Consequently, the last spectral calibration results presented in January 2023 DQR stay valid.

2.3.2 OLCI-B

There was no S02+S03 nor S09 Spectral Calibration for OLCI-B in the reporting period.

Consequently, the last spectral calibration results presented in January 2023 DQR stay valid.

2.4 Signal to Noise assessment [OLCI-L1B-CV-620]

2.4.1 SNR from Radiometric calibration data

2.4.1.1 OLCI-A

SNR computed for all calibration data (S01, S04 and S05 sequences) as a function of band number is presented in Figure 54.

SNR computed for all calibration data as a function of orbit number for band Oa01 (the less stable band) is presented in Figure 55.

There is no significant evolution of this parameter during the current reporting period and the ESA requirement is fulfilled for all bands.

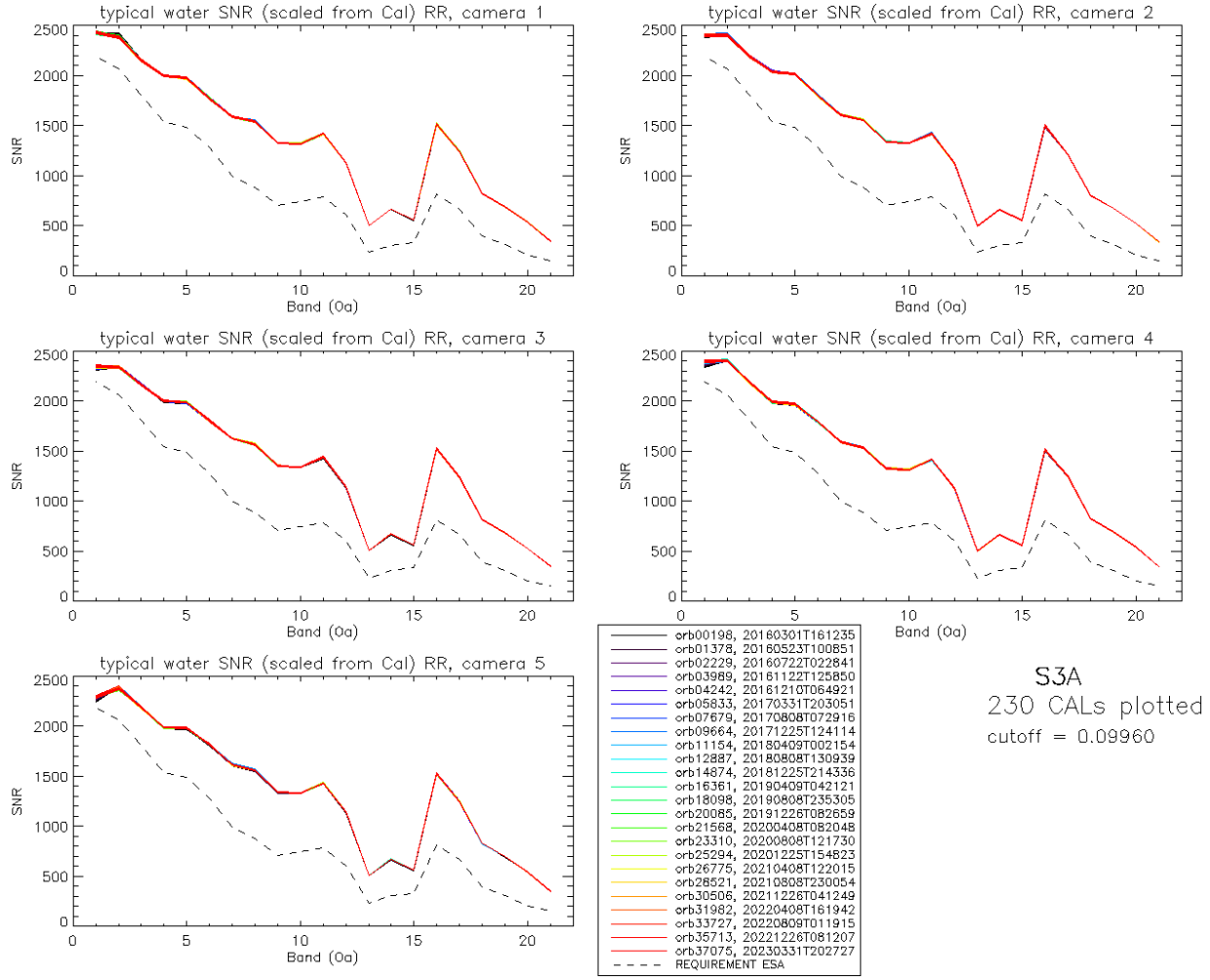

Figure 54: OLCI-A Signal to Noise ratio as a function of the spectral band for the 5 cameras. These results have been computed from radiometric calibration data. All calibrations except first one (orbit 183) are presents with the colours corresponding to the orbit number (see legend). The SNR is very stable with time: the curves for all orbits are almost superimposed. The dashed curve is the ESA requirement.

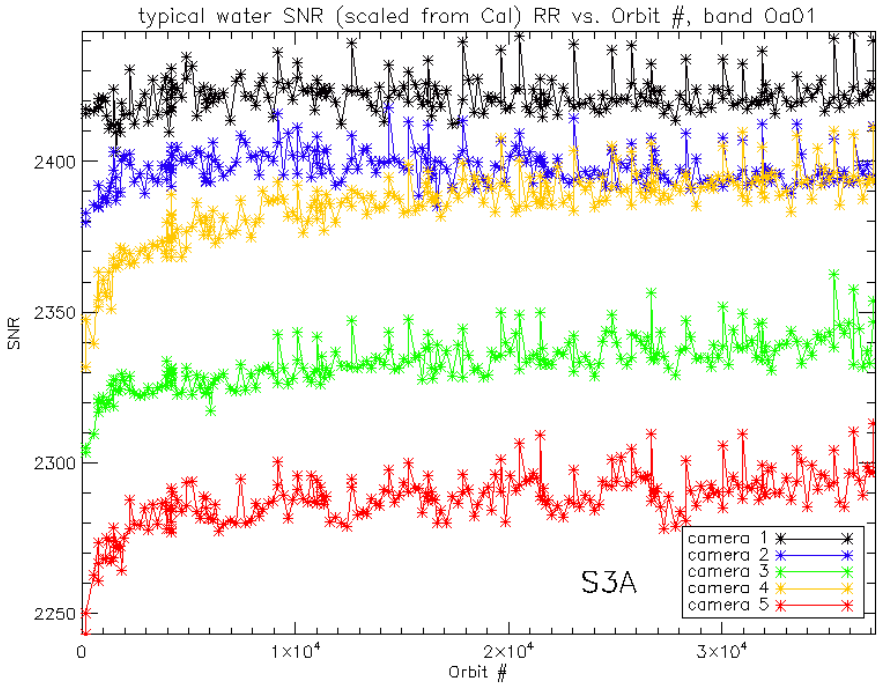

Figure 55: long-term stability of the SNR estimates from Calibration data, example of channel Oa1.

The mission averaged SNR figures are provided in Table 1 below, together with their radiance reference level. According to the OLCI SNR requirements, these figures are valid at these radiance levels and at Reduced Resolution (RR, 1.2 km). They can be scaled to other radiance levels assuming shot noise (CCD sensor noise) is the dominating term, i.e. radiometric noise can be considered Gaussian with its standard deviation varying as the square root of the signal; in other words: $SNR(L) = SNR(L_{ref}) \cdot \sqrt{\frac{L}{L_{ref}}}$. Following the same assumption, values at Full Resolution (300m) can be derived from RR ones as 4 times smaller.

Table 1: OLCI-A SNR figures as derived from Radiometric Calibration data. Figures are given for each camera (time average and standard deviation), and for the whole instrument. The requirement and its reference radiance level are recalled (in $mW.sr^{-1}.m^{-2}.nm^{-1}$).

	L_{ref}	SNR	C1		C2		C3		C4		C5		All	
nm	LU	RQT	avg	*std*	avg	*std*	avg	*std*	avg	*std*	avg	*std*	avg	*std*
400.000	63.0	2188	2422	6.3	2398	6.2	2333	8.3	2385	12.1	2287	9.4	2365	7.1
412.000	74.1	2061	2386	9.4	2403	7.5	2339	5.0	2401	5.0	2379	9.3	2381	5.8
442.000	65.6	1811	2157	6.0	2195	6.1	2163	5.0	2185	4.2	2193	5.9	2179	4.2
490.000	51.2	1541	1999	4.8	2036	4.7	1998	4.3	1984	4.4	1988	4.3	2001	3.2
510.000	44.4	1488	1979	5.2	2014	4.8	1986	4.5	1967	4.4	1985	4.2	1986	3.3
560.000	31.5	1280	1775	4.7	1802	4.1	1803	4.7	1794	3.8	1819	3.3	1799	3.0
620.000	21.1	997	1591	4.1	1608	4.3	1624	3.1	1593	3.2	1615	3.4	1606	2.5
665.000	16.4	883	1545	4.1	1557	4.5	1566	3.9	1533	3.5	1561	3.6	1552	3.0
674.000	15.7	707	1328	3.3	1336	3.7	1350	2.8	1323	3.2	1343	3.4	1336	2.4
681.000	15.1	745	1319	3.5	1325	3.3	1338	2.7	1314	2.5	1334	3.3	1326	2.1
709.000	12.7	785	1420	4.1	1420	4.0	1435	3.4	1414	3.5	1431	3.0	1424	2.7
754.000	10.3	605	1127	3.1	1121	2.8	1136	3.1	1125	2.5	1139	2.7	1130	2.2
761.000	6.1	232	502	1.1	498	1.1	505	1.1	501	1.1	508	1.3	503	0.8
764.000	7.1	305	663	1.5	658	1.5	668	2.0	662	1.5	670	2.0	664	1.3
768.000	7.6	330	558	1.4	554	1.3	563	1.3	557	1.3	564	1.3	559	1.0
779.000	9.2	812	1516	4.5	1498	4.4	1527	5.1	1512	4.8	1527	4.8	1516	4.0
865.000	6.2	666	1243	3.5	1213	3.4	1240	3.8	1247	3.5	1250	2.8	1239	2.7
885.000	6.0	395	823	1.7	801	1.5	814	1.9	824	1.5	831	1.6	819	1.1
900.000	4.7	308	690	1.6	673	1.3	683	1.6	693	1.6	698	1.4	688	1.0
940.000	2.4	203	534	1.2	522	1.1	525	1.0	539	1.1	542	1.3	532	0.7
1020.000	3.9	152	345	0.9	337	0.8	348	0.7	345	0.8	351	0.8	345	0.5

2.4.1.2 OLCI-B

SNR computed for all OLCI-B calibration data (S01, S04 (but not the dark-only S04) and S05 sequences) as a function of band number is presented in Figure 56.

SNR computed for all OLCI-B calibration data as a function of orbit number for band Oa01 (the less stable band) is presented in Figure 57.

As for OLCI-A the SNR is very stable in time. There is no significant evolution of this parameter during the current reporting and the ESA requirement is fulfilled for all bands.

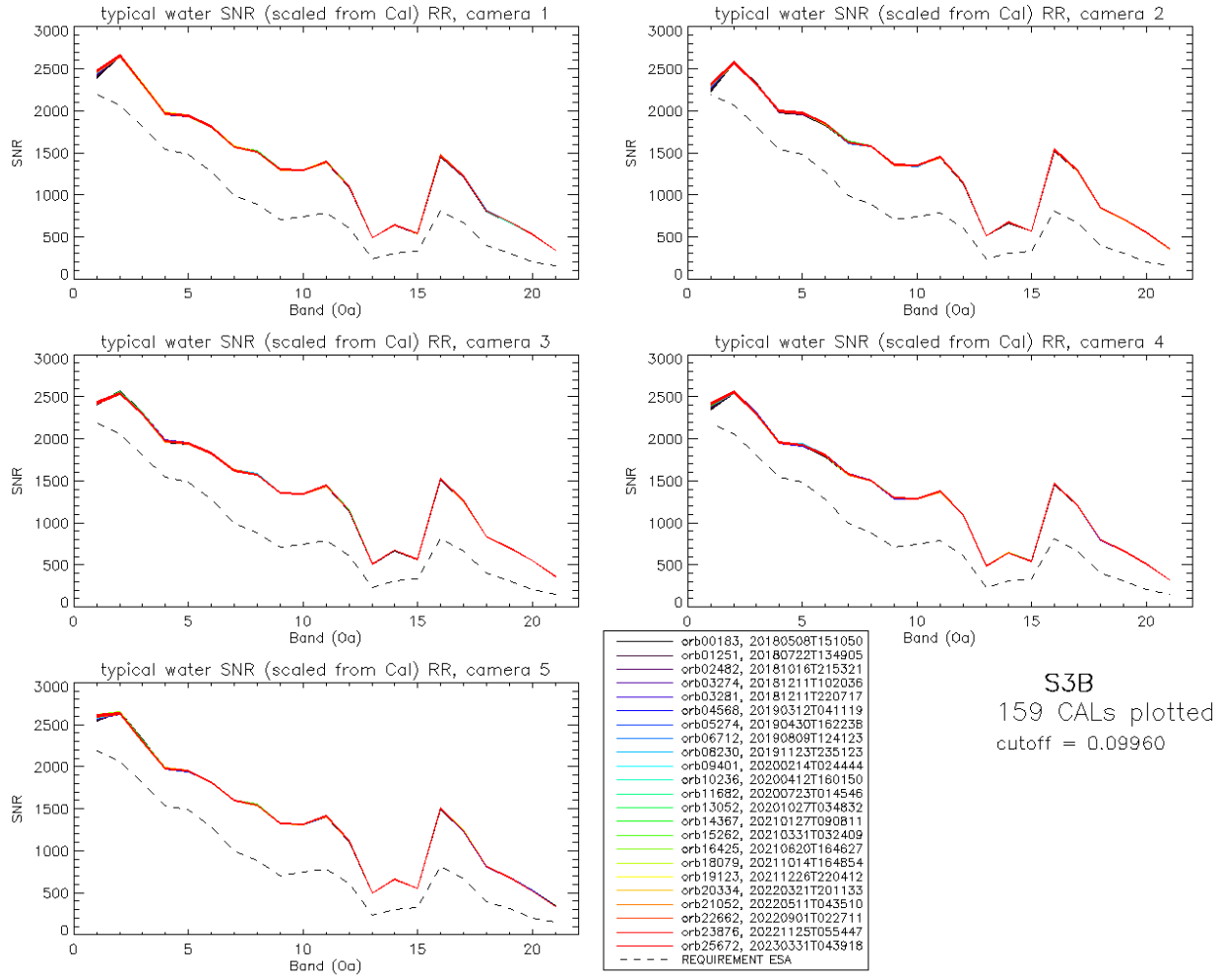

Figure 56: OLCI-B Signal to Noise ratio as a function of the spectral band for the 5 cameras. These results have been computed from radiometric calibration data. All calibrations except first one (orbit 167) are presents with the colours corresponding to the orbit number (see legend). The SNR is very stable with time: the curves for all orbits are almost superimposed. The dashed curve is the ESA requirement.

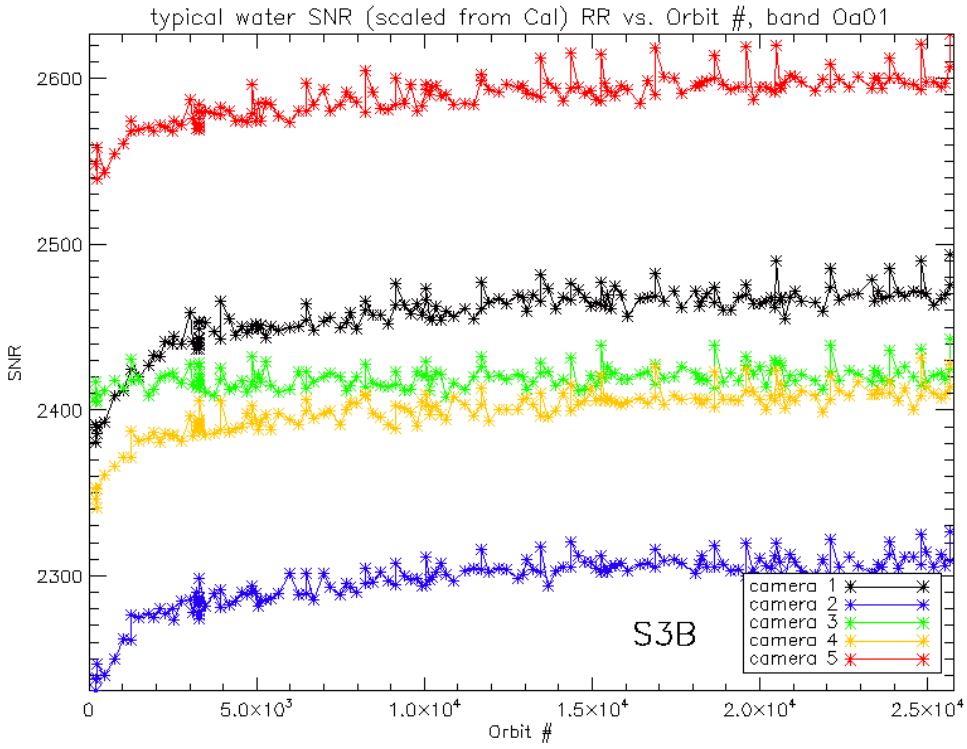

Figure 57: long-term stability of the OLCI-B SNR estimates from Calibration data, example of channel Oa1.

Table 2: OLCI-B SNR figures as derived from Radiometric Calibration data. Figures are given for each camera (time average and standard deviation), and for the whole instrument. The requirement and its reference radiance level are recalled (in $mW.sr^{-1}.m^{-2}.nm^{-1}$).

	L_{ref}	SNR	C1		C2		C3		C4		C5		All	
nm	LU	RQT	avg	*std*	avg	*std*	avg	*std*	avg	*std*	avg	*std*	avg	*std*
400.000	63.0	2188	2457	18.8	2297	16.6	2419	6.7	2399	14.1	2588	14.4	2432	13.2
412.000	74.1	2061	2654	6.9	2569	6.4	2543	8.6	2550	6.3	2637	7.6	2591	5.6
442.000	65.6	1811	2323	6.6	2316	6.3	2299	6.7	2302	6.9	2307	6.6	2309	5.7
490.000	51.2	1541	1966	4.9	1990	5.7	1971	5.1	1952	4.6	1979	4.5	1972	3.9
510.000	44.4	1488	1939	4.9	1968	6.1	1943	5.0	1925	5.0	1952	4.8	1945	4.1
560.000	31.5	1280	1813	4.7	1848	4.9	1829	4.7	1805	4.7	1817	4.0	1822	3.6
620.000	21.1	997	1572	4.2	1626	4.6	1624	3.9	1577	3.6	1601	3.4	1600	2.9
665.000	16.4	883	1513	4.1	1579	3.8	1573	3.7	1501	3.0	1546	3.7	1542	2.8
674.000	15.7	707	1300	3.8	1358	3.5	1353	3.2	1292	2.7	1328	2.9	1326	2.3
681.000	15.1	745	1293	3.5	1347	3.2	1343	3.0	1285	2.8	1316	2.9	1317	2.1
709.000	12.7	785	1390	4.0	1447	4.0	1443	4.0	1373	2.9	1412	3.6	1413	2.9
754.000	10.3	605	1096	3.6	1143	3.6	1142	3.3	1089	2.8	1116	3.2	1117	2.8
761.000	6.1	232	488	1.2	509	1.2	509	1.4	486	1.2	498	1.4	498	1.0
764.000	7.1	305	643	1.6	673	2.0	672	1.8	641	1.8	658	1.8	657	1.5
768.000	7.6	330	541	1.5	568	1.4	564	1.3	541	1.3	555	1.5	554	1.1
779.000	9.2	812	1467	4.1	1536	4.7	1527	5.2	1468	3.9	1507	4.2	1501	3.7
865.000	6.2	666	1221	3.5	1288	3.8	1258	3.6	1206	3.6	1238	2.8	1242	2.8
885.000	6.0	395	808	2.2	848	1.9	834	2.0	799	1.7	815	2.1	821	1.5
900.000	4.7	308	679	1.5	714	1.9	704	1.7	670	1.5	683	1.5	690	1.2
940.000	2.4	203	527	1.3	549	1.5	551	1.3	510	1.1	522	1.3	532	0.9
1020.000	3.9	152	336	0.8	358	1.2	358	0.8	318	0.7	338	0.9	342	0.6

2.5 Geometric Calibration/Validation

2.5.1 OLCI-A

OLCI-A georeferencing performance is compliant since the introduction of MPC Geometric Calibration, put in production on the 14th of March 2018. It has however significantly improved after its last full revision of GCMs (Geometric Calibration Models, or platform to instrument alignment quaternions) and IPPVMs (Instrument Pixels Pointing Vectors) both derived using the GeoCal Tool and put in production on 30/07/2019.

The following figures (Figure 58 to Figure 63) show time series of the overall RMS performance (requirement criterion) and of the across-track and along-track biases for each camera. New plots (Figure 64 and Figure 65) introduce monitoring of the performance homogeneity within the field of view: georeferencing errors in each direction at camera transitions (difference between last pixel of camera N and first pixel of camera N+1) and within a given camera (maximum bias minus minimum inside each camera). The performance improvement since the 30/07/2019 is significant on most figures: the global RMS value decreases form around 0.35 to about 0.2 (Figure 58), the across-track biases decrease significantly for all cameras (Figure 59 to Figure 63), the along-track bias reduces for at least camera 3 (Figure 61) and the field of view homogeneity improves drastically (Figure 64 and Figure 65, but also reduction of the dispersion – distance between the ± 1 sigma lines – in Figure 59 to Figure 63).

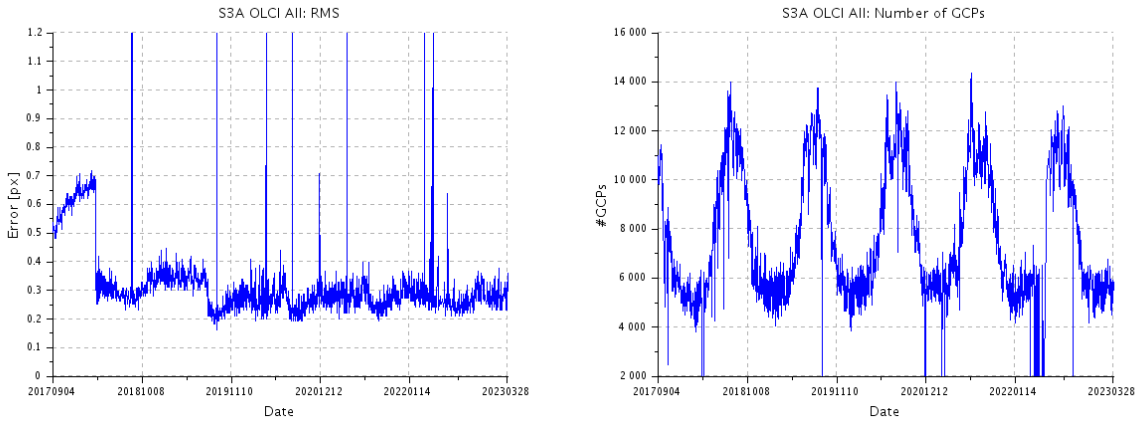

Figure 58: overall OLCI-A georeferencing RMS performance time series (left) and number of validated control points corresponding to the performance time series (right) over the whole monitoring period

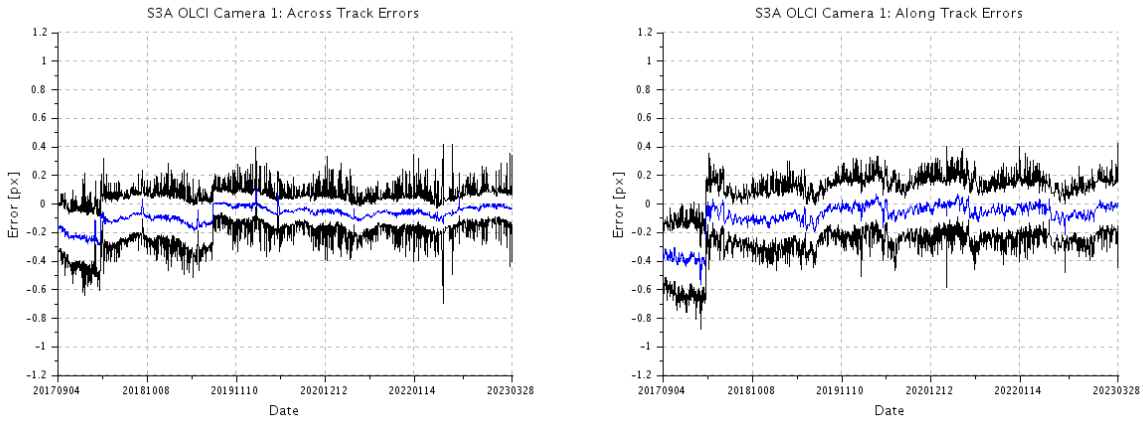

Figure 59: across-track (left) and along-track (right) OLCI-A georeferencing biases time series for Camera 1. Blue line is the average, black lines are average plus and minus 1 sigma.

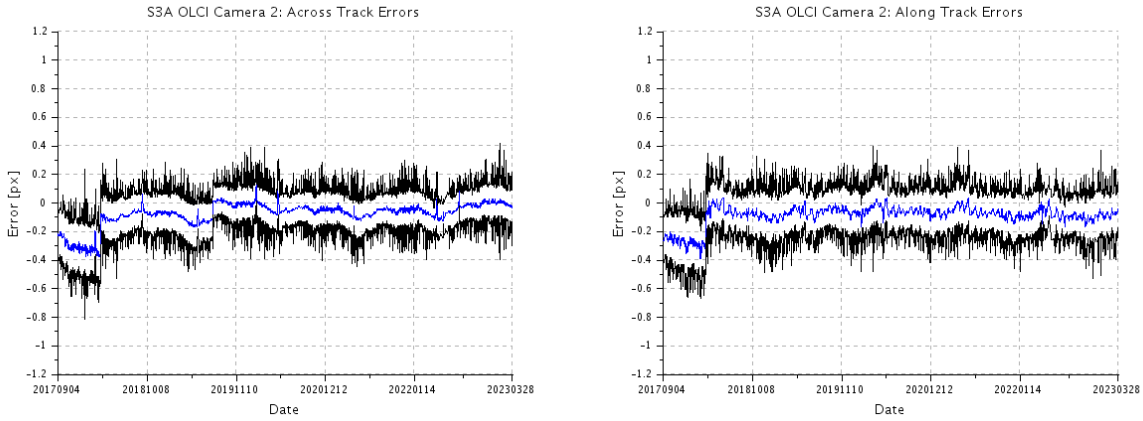

Figure 60: same as Figure 59 for Camera 2.

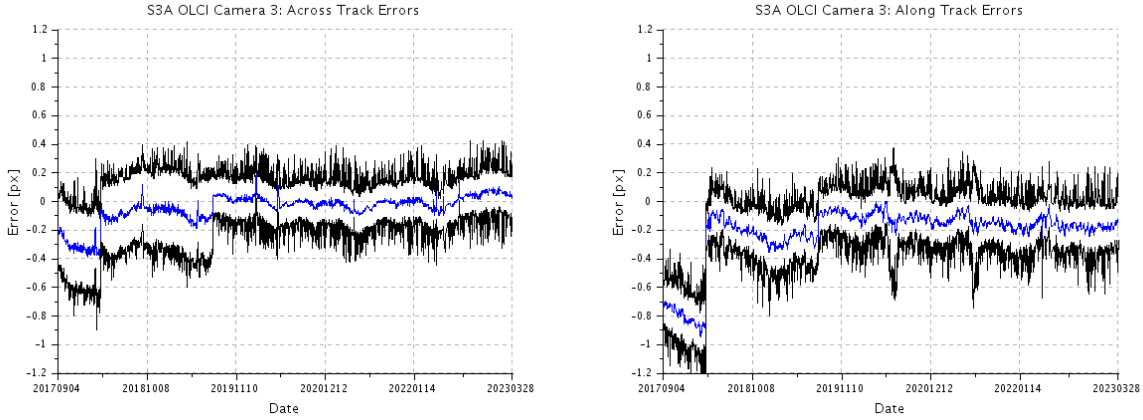

Figure 61: same as Figure 59 for Camera 3.

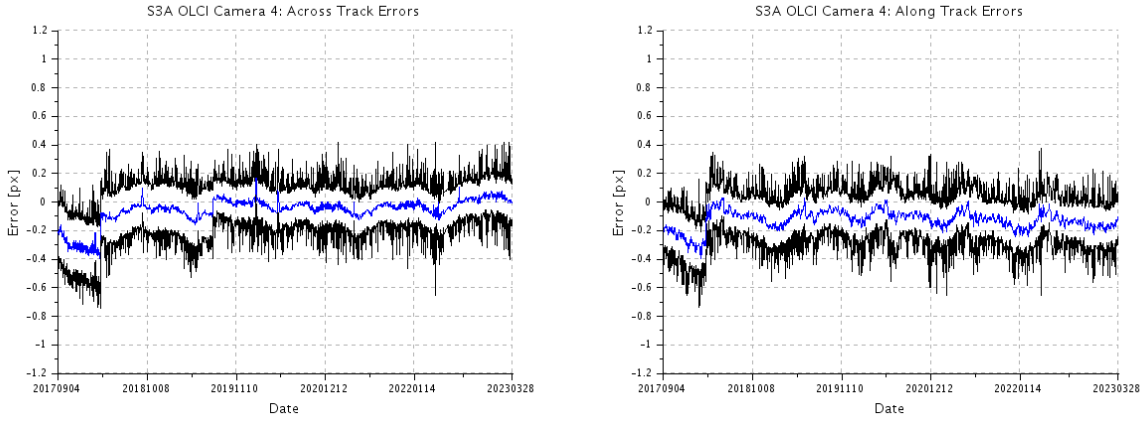

Figure 62: same as Figure 59 for Camera 4.

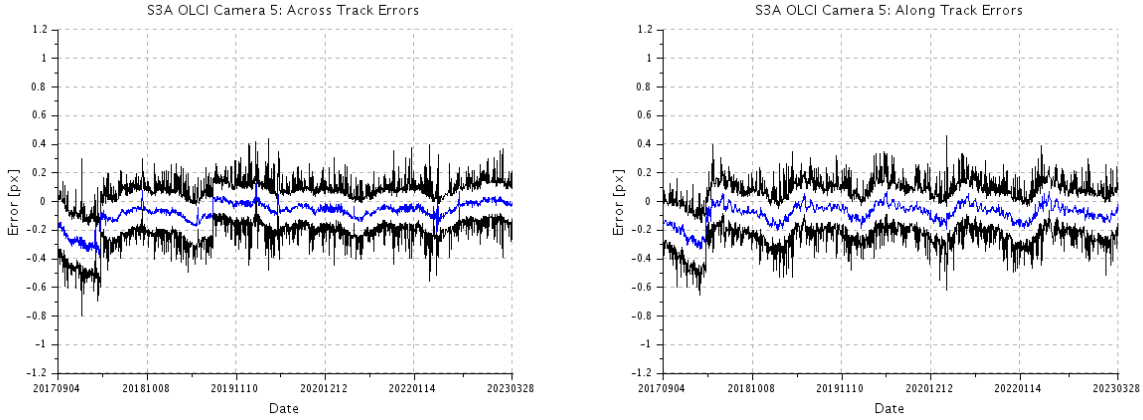

Figure 63: same as Figure 59 for Camera 5.

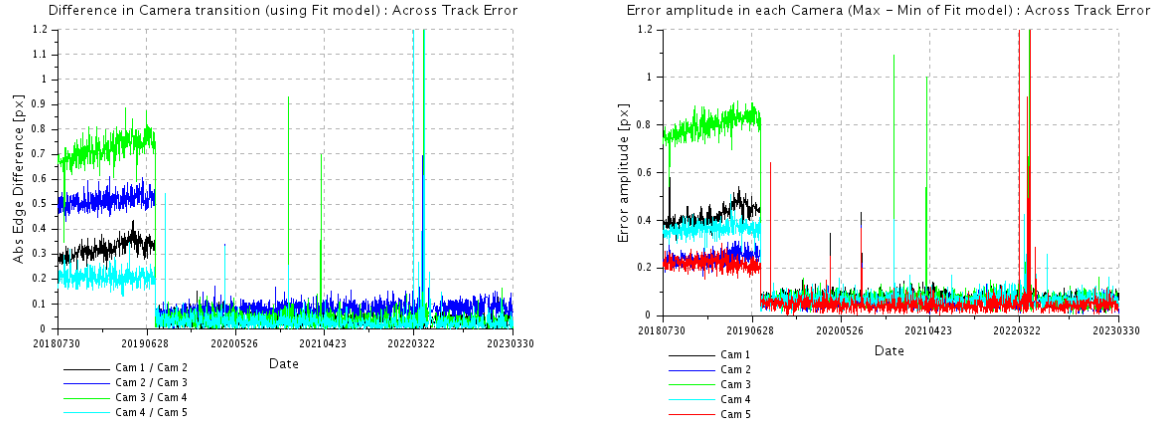

Figure 64: OLCI-A spatial across-track misregistration at each camera transition (left) and maximum amplitude of the across-track error within each camera (left).

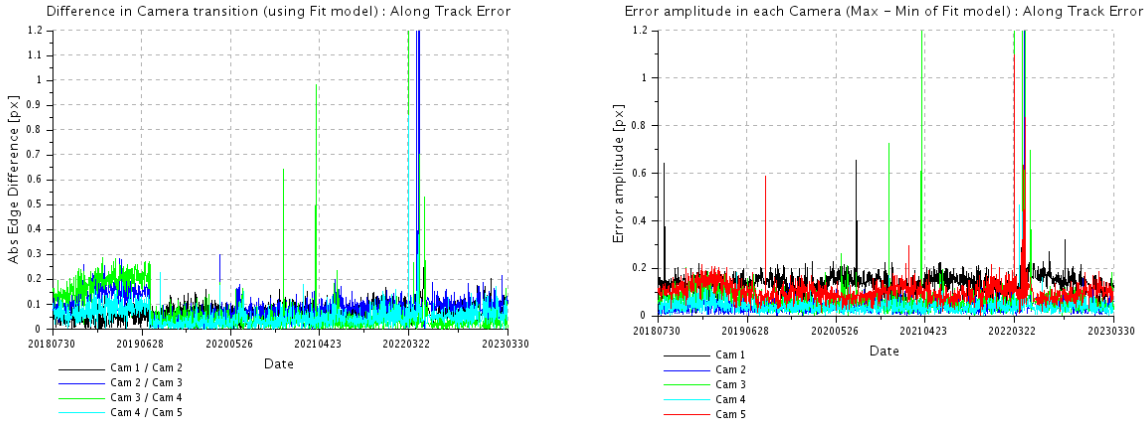

Figure 65: OLCI-A spatial along-track misregistration at each camera transition (left) and maximum amplitude of the along-track error within each camera (left).

2.5.2 OLCI-B

Georeferencing performance of OLCI-B improved significantly with the fourth geometric calibration introduced the 30/07/2019. However, the instrument pointing is still evolving, in particular for camera 2 (Figure 72) and a new geometric calibration has been done and introduced in the processing chain on the 16th of April 2020. Its impact is significant on the along-track biases of all cameras (Figure 67 to Figure 71), but also on the continuity at camera interfaces (Figure 72, left) and on intra-camera homogeneity (Figure 72, right). Since then, further adjustments to the geometric calibration have been introduced, mainly to correct the along-track drifts. The most recent was put in production on 29/07/2021 and its effect can be seen e.g. on left graphs of Figure 68, Figure 69 and Figure 71 (across-track biases of cameras 2, 3 & 5).

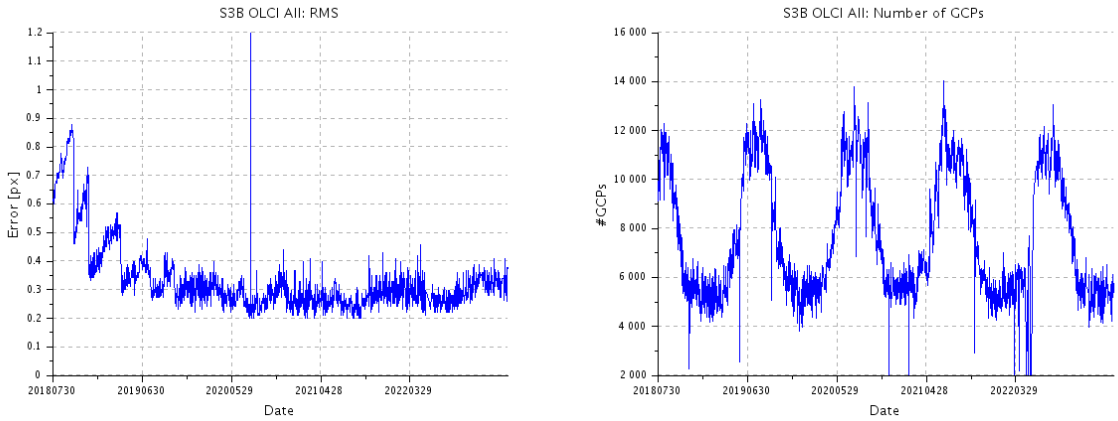

Figure 66: overall OLCI-B georeferencing RMS performance time series over the whole monitoring period (left) and corresponding number of validated control points (right)

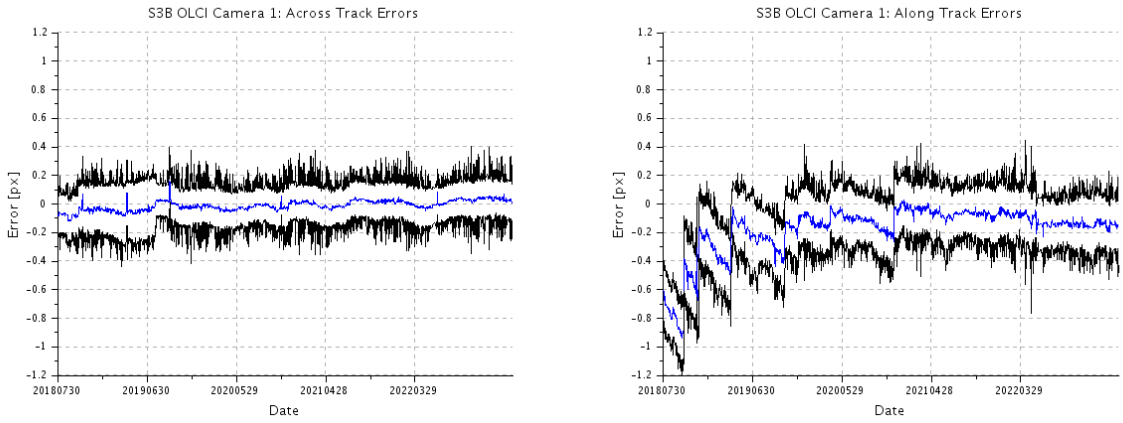

Figure 67: across-track (left) and along-track (right) OLCI-B georeferencing biases time series for Camera 1.

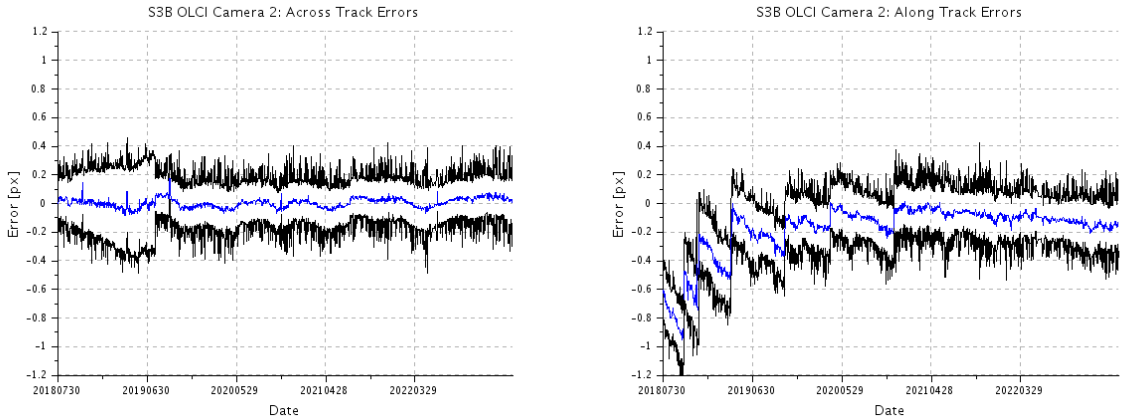

Figure 68: same as Figure 67 for Camera 2.

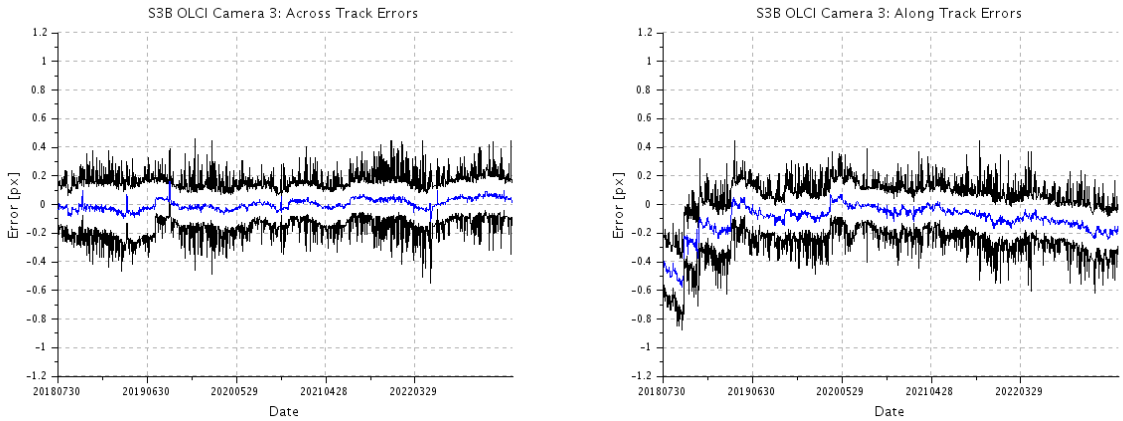

Figure 69: same as Figure 67 for Camera 3.

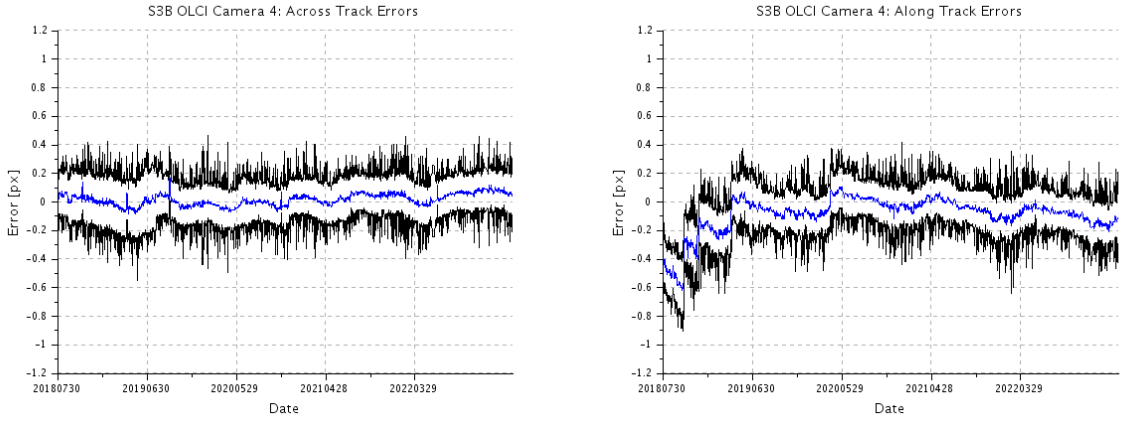

Figure 70: same as Figure 67 for Camera 4.

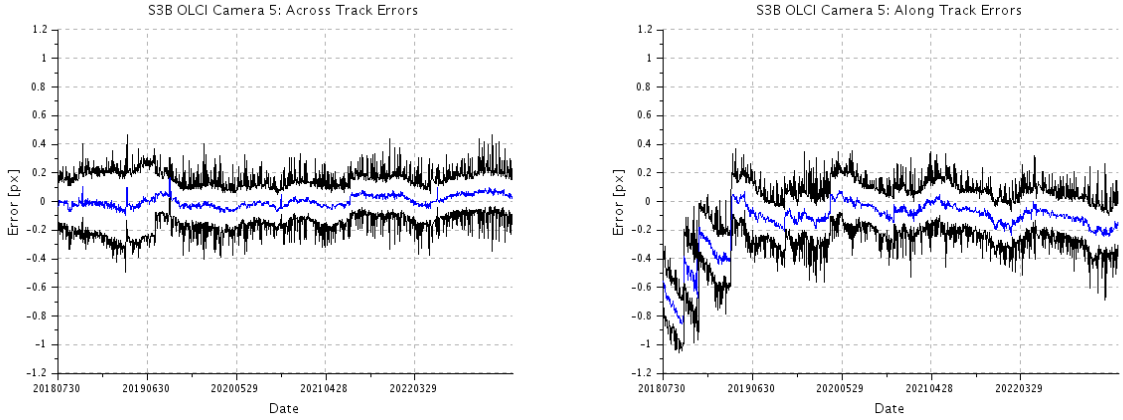

Figure 71: same as Figure 67 for Camera 5.

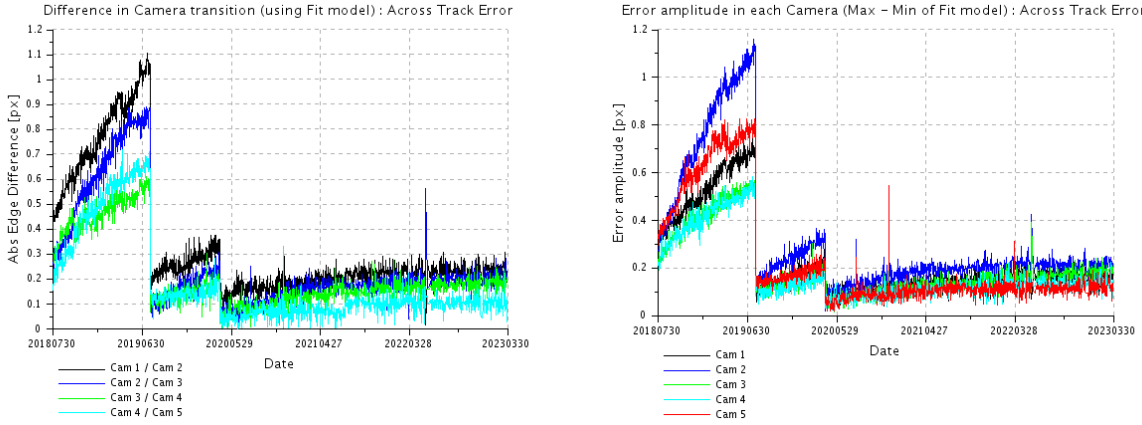

Figure 72: OLCI-B spatial across-track misregistration at each camera transition (left) and maximum amplitude of the across-track error within each camera (left).

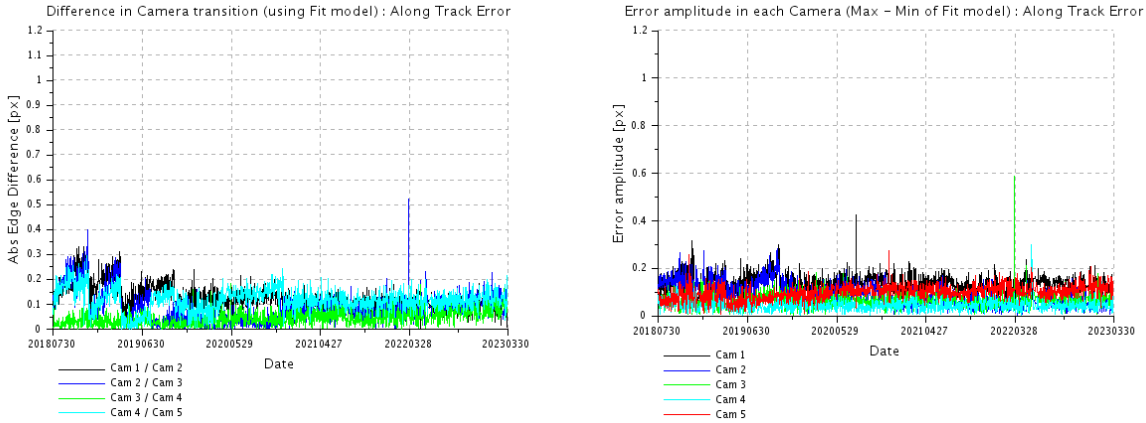

Figure 73: OLCI-B spatial along-track misregistration at each camera transition (left) and maximum amplitude of the along-track error within each camera (left).

3 OLCI Level 1 Product validation

3.1 [OLCI-L1B-CV-300], [OLCI-L1B-CV-310] – Radiometric Validation

3.1.1 S3ETRAC Service

Activities done

The S3ETRAC service extracts OLCI L1 RR and SLSTR L1 RBT data and computes associated statistics over 49 sites corresponding to different surface types (desert, snow, ocean maximizing Rayleigh signal, ocean maximizing sunglint scattering and deep convective clouds). The S3ETRAC products are used for the assessment and monitoring of the L1 radiometry (optical channels) by the ESLs.

All details about the S3ETRAC/OLCI and S3ETRAC/SLSTR statistics are provided on the S3ETRAC website http://s3etrac.acri.fr/index.php?action=generalstatistics.

- Number of OLCI products processed by the S3ETRAC service
- Statistics per type of target (DESERT, SNOW, RAYLEIGH, SUNGLINT and DCC)
- Statistics per sites
- Statistics on the number of records

For illustration, we provide below statistics on the number of S3ETRAC/OLCI records generated per type of targets (DESERT, SNOW, RAYLEIGH, SUNGLINT and DCC) for both OLCI-A (Figure 74) and OLCI-B (Figure 75).

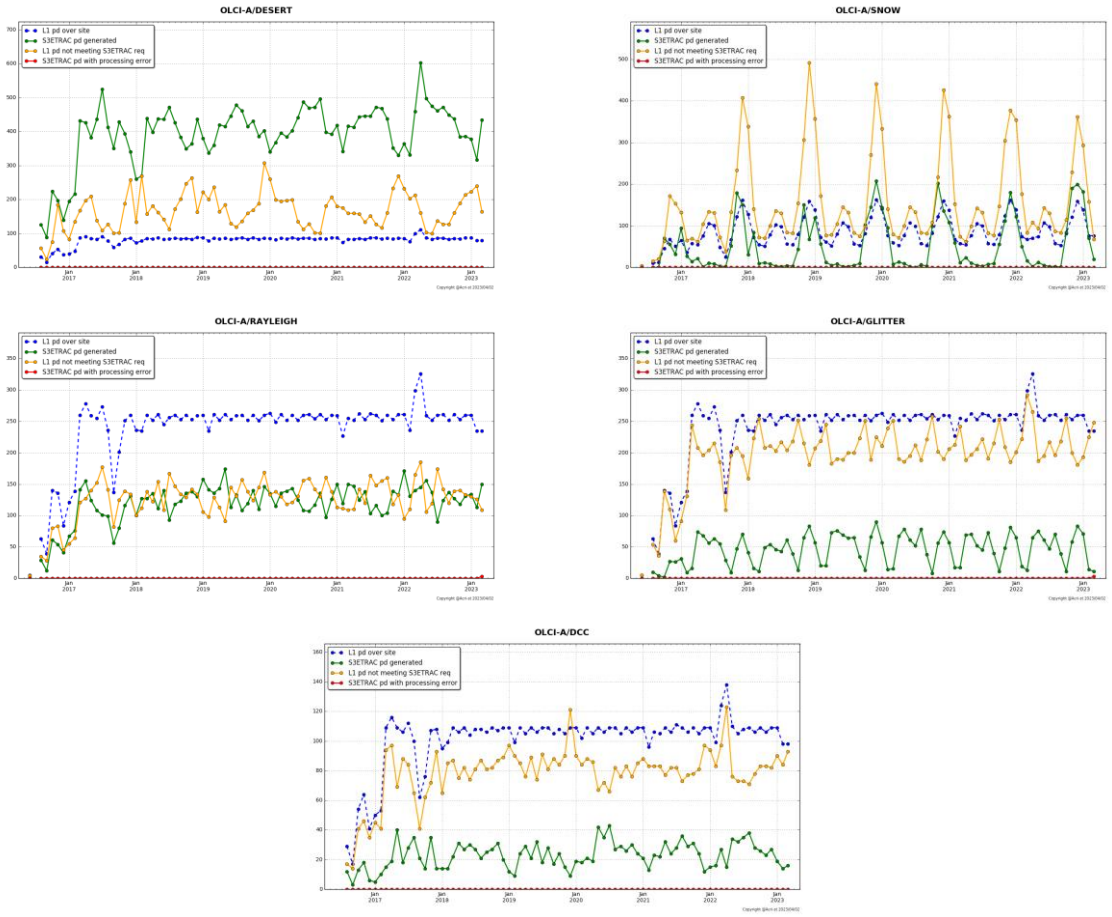

Figure 74: summary of S3ETRAC products generation for OLCI-A (number of OLCI-A L1 products Ingested, blue – number of S3ETRAC extracted products generated, green – number of S3ETRAC runs without generation of output product (data not meeting selection requirements), yellow – number of runs ending in error, red, one plot per site type).

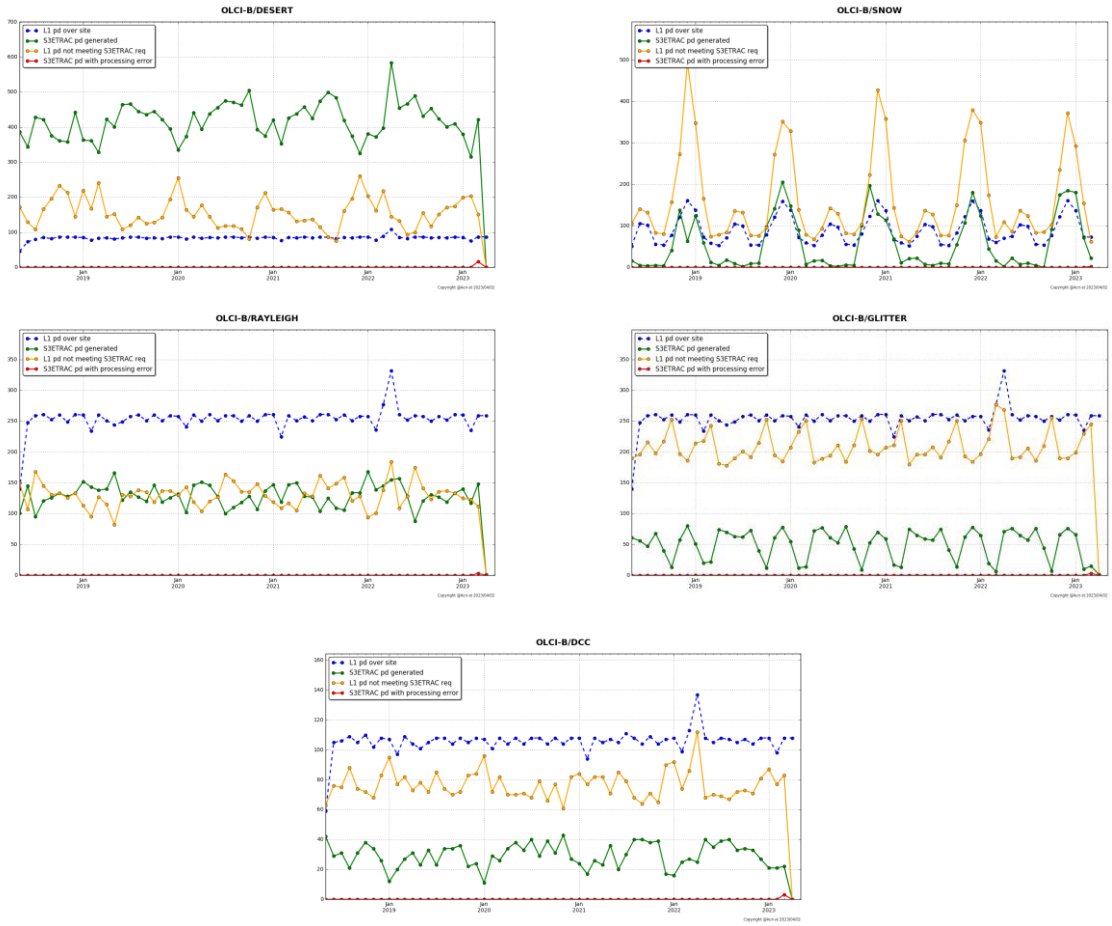

Figure 75: summary of S3ETRAC products generation for OLCI-B (number of OLCI-B L1 products Ingested, yellow – number of S3ETRAC extracted products generated, blue – number of S3ETRAC runs without generation of output product (data not meeting selection requirements), green – number of runs ending in error, red, one plot per site type).

3.1.2 Radiometric validation with DIMITRI

OLCI-A and OLCI-B L1B radiometry verification has been processed as follow:

- The verification is performed over Ocean-sites and over Desert-sites **until the 25th of March 2023.**
- All results from OLCI-A and OLCI-B over Rayleigh, Glint and PICS are consistent with the previous reporting period over the used CalVal sites.
- Good stability of both sensors OLCI-A and OLCI-B could be observed, nevertheless the time-series average shows higher reflectance from OLCI-A.
- Bands with high gaseous absorption are excluded.

Verification and Validation over PICS

1. The ingestion of all the available L1B-LN1-NT products from OLCI-A and OLCI-B over the 6 desert CalVal-sites (Algeria3 & 5, Libya 1 & 4 and Mauritania 1 & 2) has been performed until the **25th of March 2023**.
2. The results are consistent over all the six used PICS sites (Figure 76 and Figure 77). Both sensors show a good stability over the analysed period.
3. The temporal average over the period **January 2022 - 25th of March2023** of the elementary ratios (observed reflectance to the simulated one) for **OLCI-A** shows gain values between 2-4% over all the VNIR bands (Figure 78). Unlikely, the temporal average over the same period of the elementary ratios for **OLCI-B** shows gain values within 2% (mission requirements) over the VNIR spectral range (Figure 78). The spectral bands with significant absorption from water vapor and O_2 (Oa11, Oa13, Oa14, Oa15 and Oa20) are excluded.

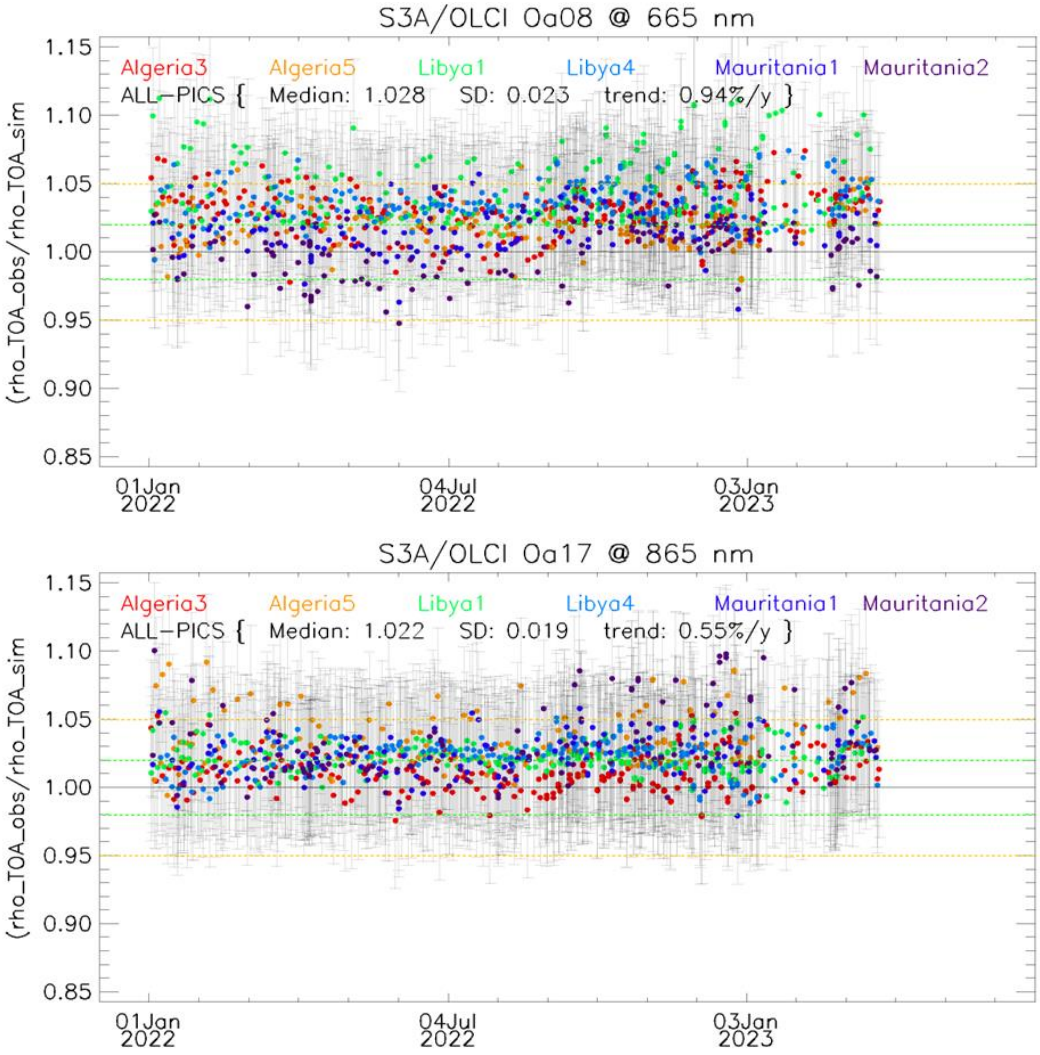

Figure 76: Time-series of the elementary ratios (observed/simulated) signal from OLCI-A for (top to bottom) bands Oa03 and Oa17 respectively over January 2022-March 2023 from the six PICS Cal/Val sites. Dashed-green and orange lines indicate the 2% and 5% respectively. Error bars indicate the desert methodology uncertainty.

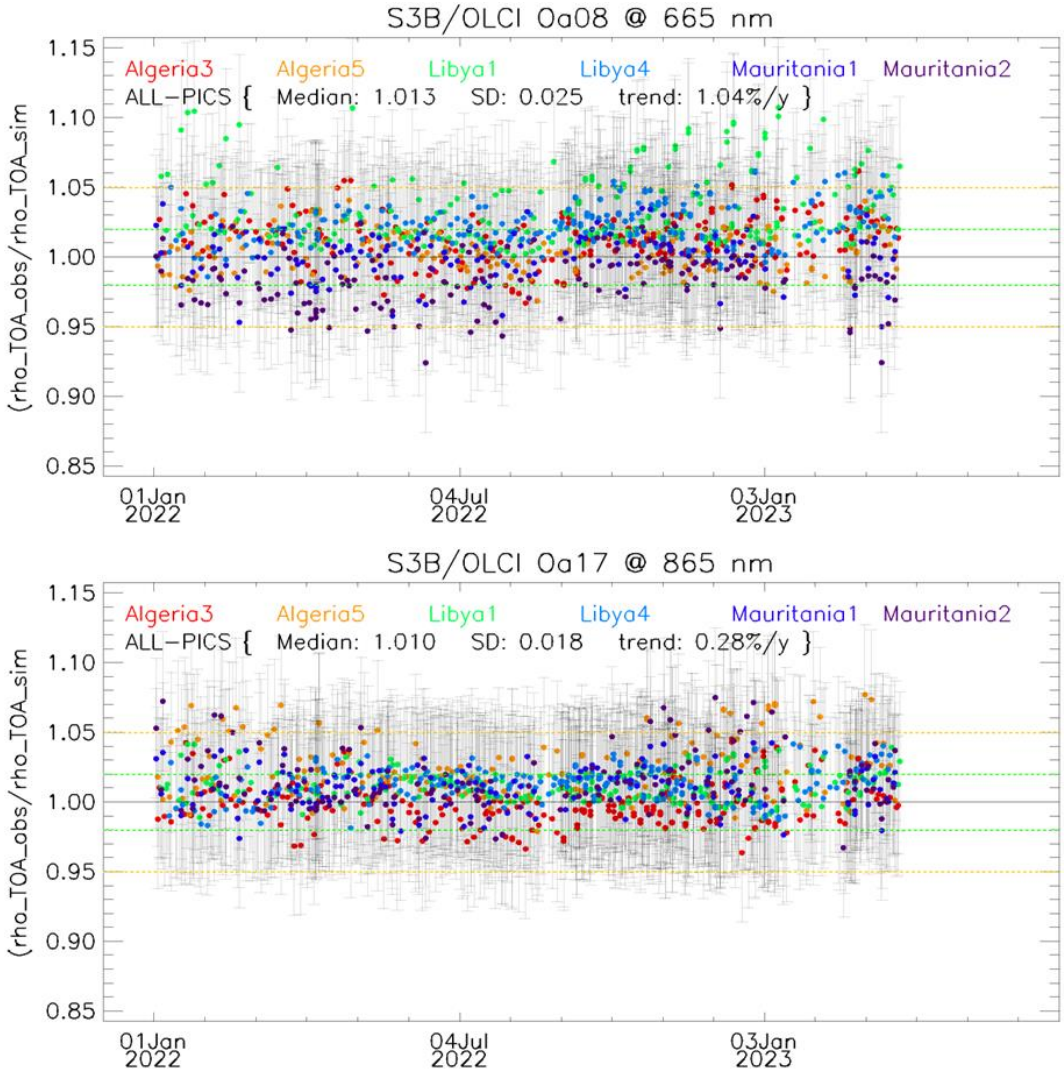

Figure 77: Time-series of the elementary ratios (observed/simulated) signal from OLCI-B for (top to bottom) bands Oa08 and Oa17 respectively over January 2022- March 2023 from the six PICS Cal/Val sites. Dashed-green and orange lines indicate the 2% and 5% respectively. Error bars indicate the desert methodology uncertainty.

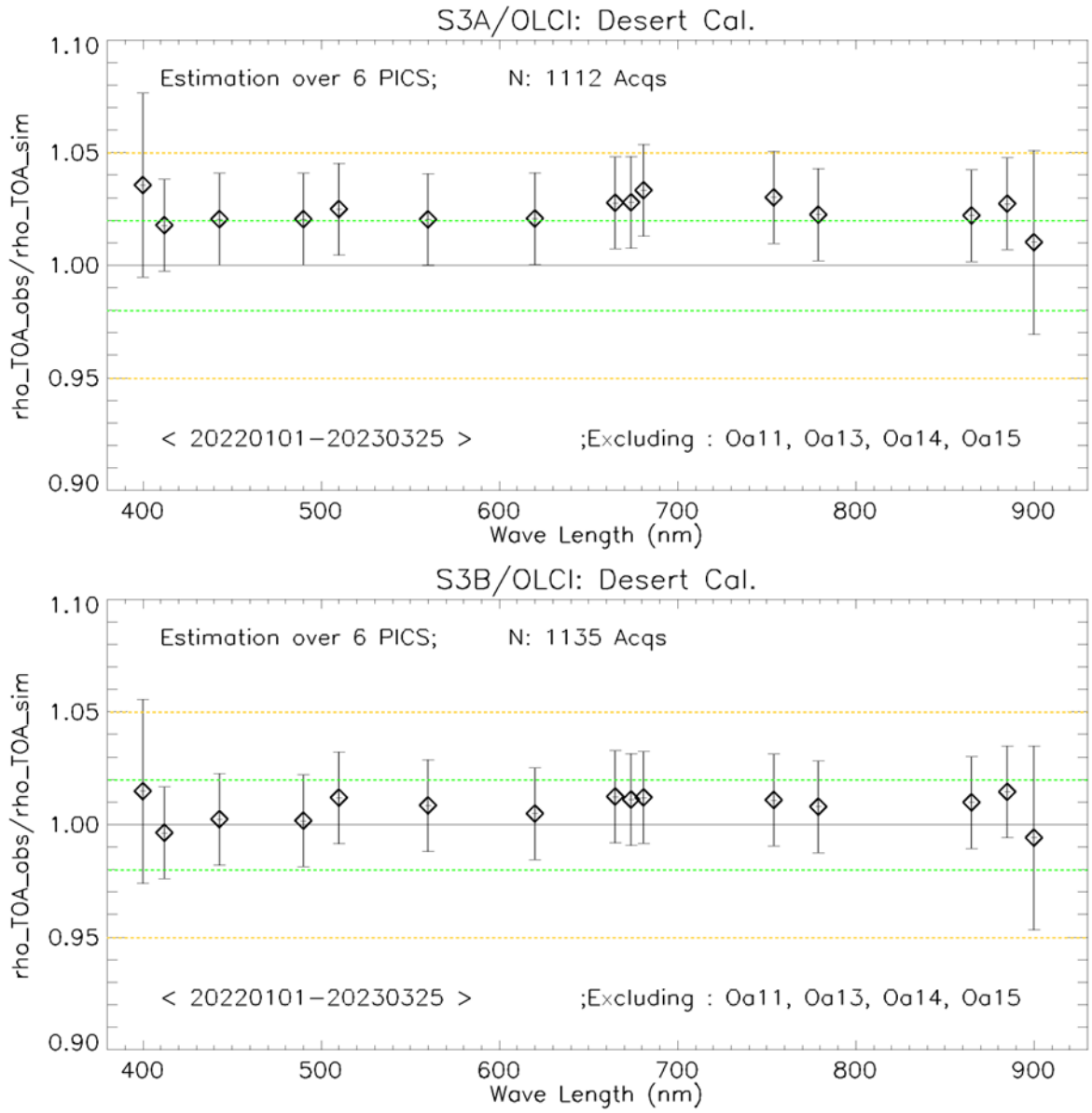

Figure 78: The estimated gain values for OLCI-A and OLCI-B over the 6 PICS sites identified by CEOS over the period January 2022- March 2023 as a function of wavelength. Dashed-green and orange lines indicate the 2% and 5% respectively. Error bars indicate the desert methodology uncertainty.

Validation over Rayleigh

Rayleigh method has been performed from the available mini-files over the period **January 2022- End March 2023** for OLCI-A and OLCI-B. The results were produced with the configuration (ROI-AVERAGE). The gain coefficients of OLCI-A are consistent with the previous results. Bands Oa01-Oa05 display biases values between 3%-5% while bands Oa06-Oa09 exhibit biases between about 2%, just within the mission requirement (Figure 79). The gain coefficients of OLCI-B are lower than OLCI-A ones, where bands Oa01-Oa05 display biases values about 2-5%, when bands Oa6-Oa9 exhibit biases around the 2% mission requirement (Figure 79).

Validation over Glint and synthesis

Glint calibration method with the configuration (ROI-PIXEL) has been performed over the period **January 2022- end March 2023** for OLCI-A and OLCI-B. The outcome of this analysis shows a good consistency with the desert and Rayleigh outputs over the NIR spectral range Oa06-Oa09 for both sensors. Glint results from OLCI-A show that the NIR bands are within 3% (slightly above the 2% mission requirements), except Oa21 which shows higher biases more than ~5% for both sensors (see Figure 79). Again, the glint gain from OLCI-B looks slightly lower than OLCI-A one with most bands within the 2% mission requirement if ignoring the Rayleigh results in the blue-green region.

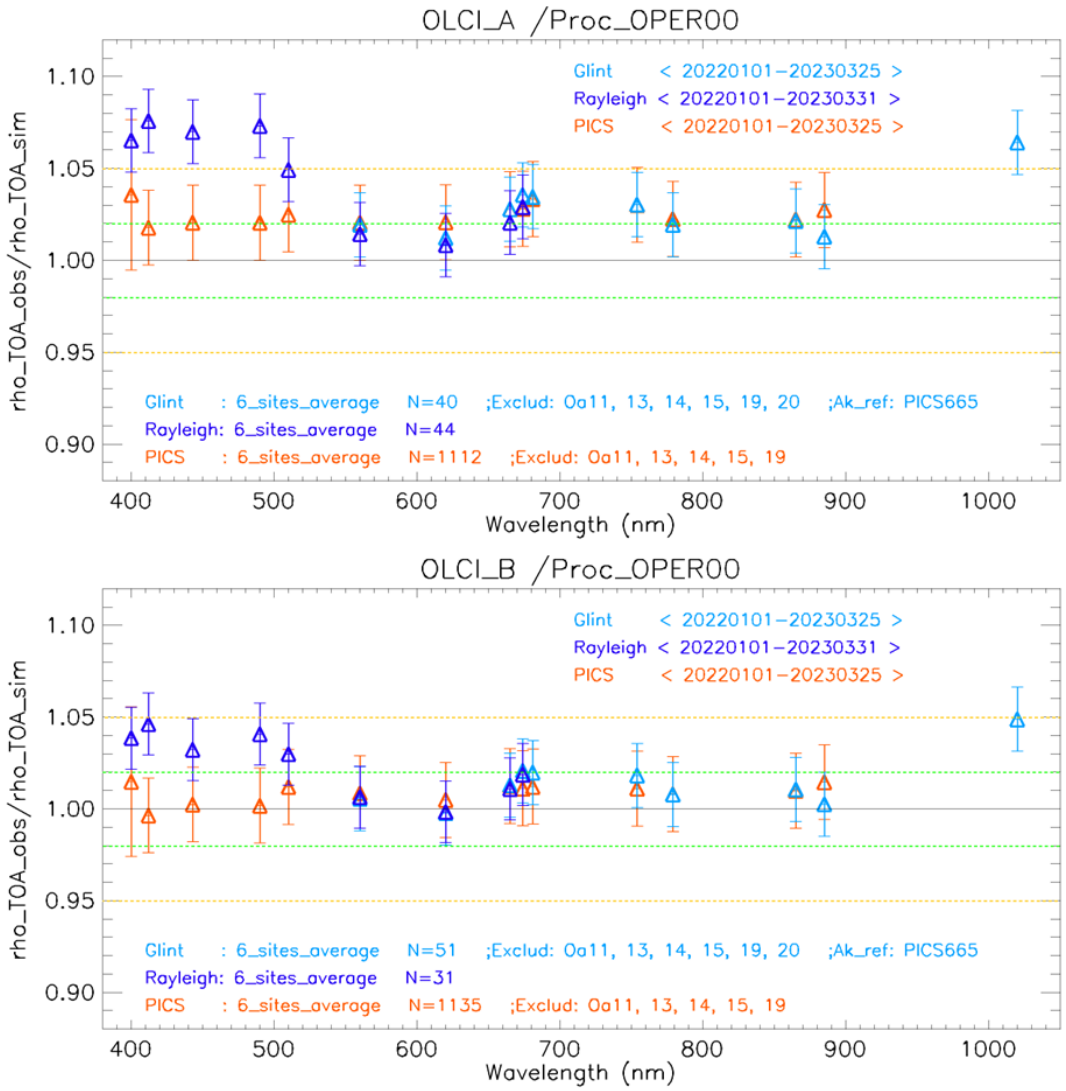

Figure 79: The estimated gain values for OLCI-A and OLCI-B from Glint, Rayleigh and PICS methods over the past twelve months as a function of wavelength. We use the gain value of Oa8 from PICS-Desert method as reference gain for Glint method. Dashed-green and orange lines indicate the 2% and 5% respectively. Error bars indicate the method uncertainties.

Cross-mission Intercomparison over PICS:

X-mission Intercomparison between OLCI-A, OLCI-B, MSI-A, MSI-B, SLSTR-A and SLSTR-B with MERIS as a reference has been performed until December 2022 (November for MSI).

Figure 80 shows the estimated gain over different time-series for different sensors over PICS. The spectral bands with significant absorption from water vapor and O2 are excluded. OLCI-A seems to have higher gain wrt the other sensors (except SLSTR-A/B), and of about 1-2% higher gain wrt to OLCI-B over VNIR spectral range.

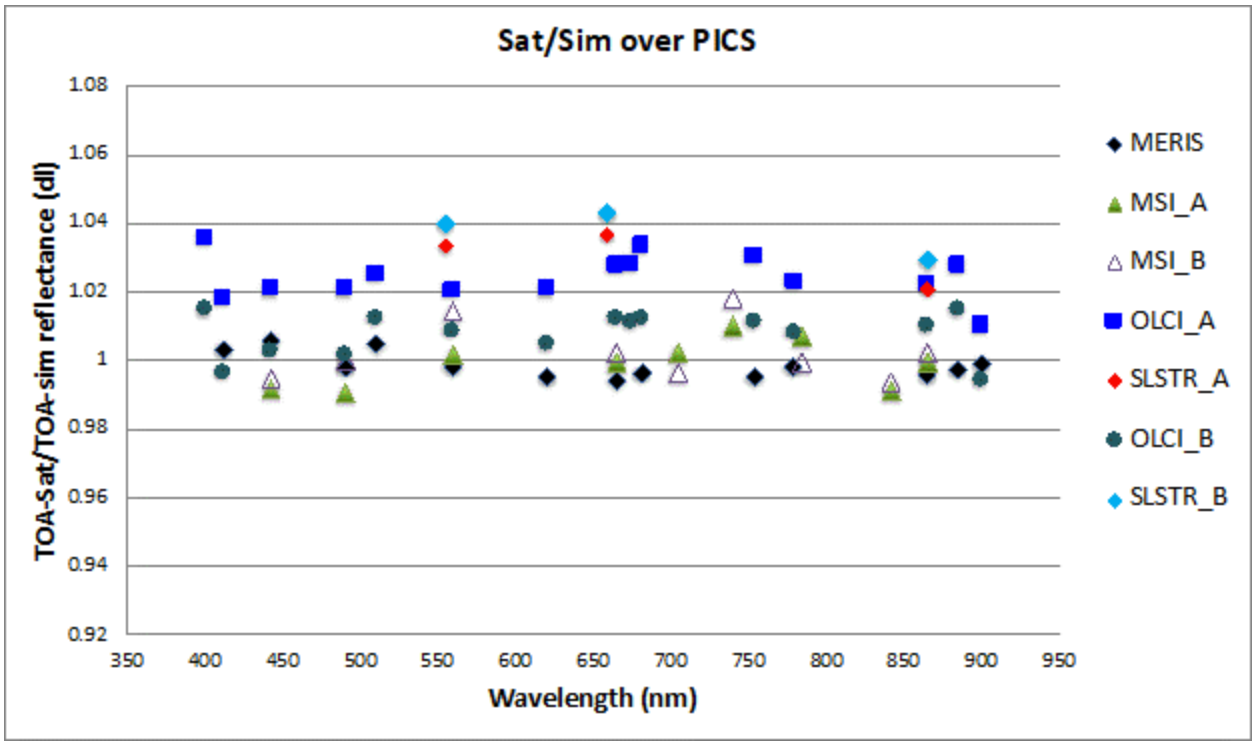

Figure 80: Ratio of observed TOA reflectance to simulated one for (black) MERIS, (pale-green) S2A/MSI, (white) S2B/MSI, (blue) S3A/OLCI, (green) S3B/OLCI, (red) S3A/SLSTR-NADIR, and (cyan) S3B/SLSTR-NADIR averaged over the six PICS test sites over different periods as a function of wavelength.

3.1.3 Radiometric validation with OSCAR

OSCAR Rayleigh results

The OSCAR Rayleigh have been applied to the S3A and S3B S3ETRAC data from the 6 oceanic calibration sites (Table 3) using a new chlorophyll climatology which has been derived from the CMEMS OLCI monthly CHL products from considering the years 2017, 2018 and 2019.

Table 3: S3ETRAC Rayleigh Calibration sites

Site Name	Ocean	North Latitude	South Latitude	East Longitude	West Longitude
PacSE	South-East of Pacific	-20.7	-44.9	-89	-130.2
PacNW	North-West of Pacific	22.7	10	165.6	139.5
PacN	North of Pacific	23.5	15	200.6	179.4
AtlN	North of Atlantic	27	17	-44.2	-62.5
AtlS	South of Atlantic	-9.9	-19.9	-11	-32.3
IndS	South of Indian	-21.2	-29.9	100.1	89.5

In Figure 81 the average OSCAR OLCI-A and OLCI-B Rayleigh results are given for March 2023. In Figure 82 and Table 4, the same results are given for all acquisitions of 2023.

In the lower wavelengths, S3A/OLCI remains significantly brighter than S3B/OLCI.

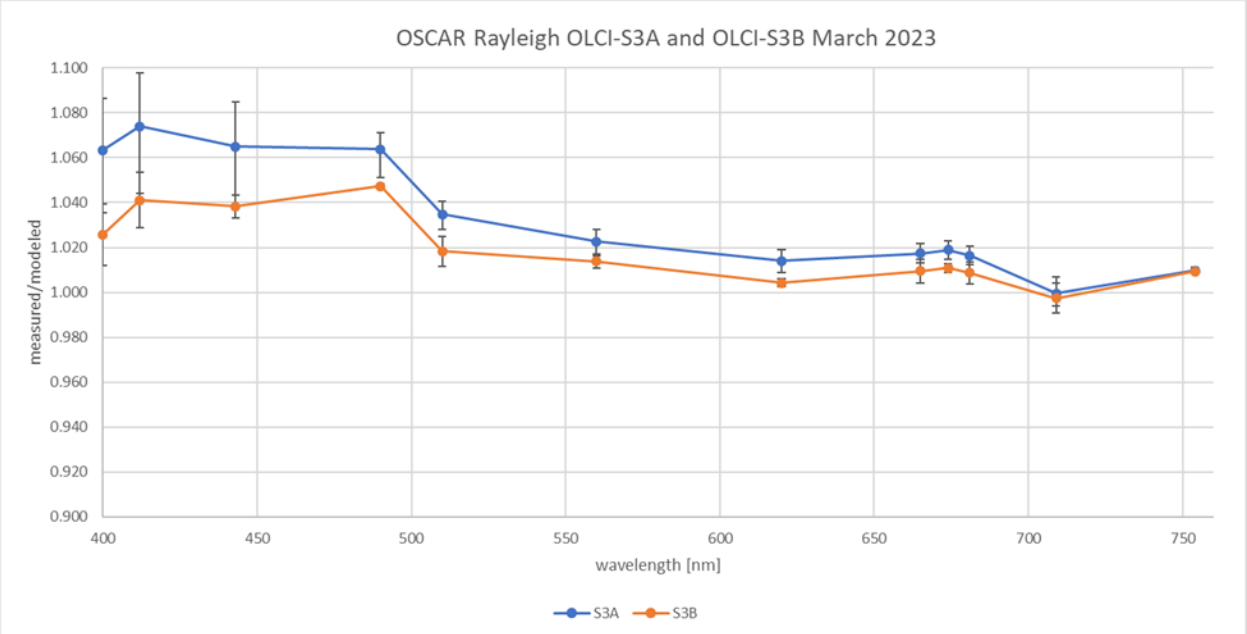

Figure 81: OSCAR Rayleigh S3A and S3B Calibration results as a function of wavelength for March 2023. The results are obtained with a new climatology derived from CMEMS OLCI monthly CHL products.

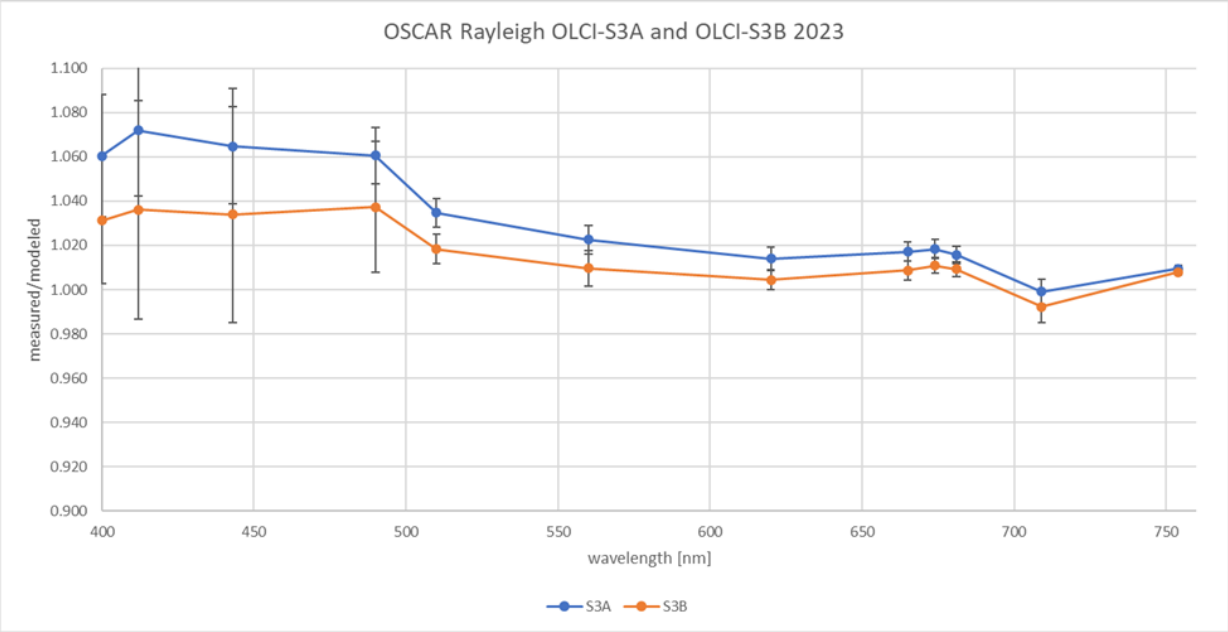

Figure 82: OSCAR Rayleigh OLCI-A and OLCI-B Calibration results as a function of wavelength for all acquisitions of 2023. The results are obtained with a new climatology derived from CMEMS OLCI monthly CHL products.

Table 4. OSCAR Rayleigh calibration results for S3A and S3B (average and standard deviation over all 2023 acquisitions) over all scenes currently (re)processed with the new climatology and observed difference (in %) between OLCIA and OLCIB

OLCI band	Wavelength (nm)	Oscar Rayleigh OLCIA		Oscar Rayleigh OLCIB		% difference OLCIA and OLCIB
		avg	stdev	avg	stdev	
Oa01	400	1.060	0.028	1.031	0.029	2.76%
Oa02	412	1.072	0.030	1.036	0.049	3.35%
Oa03	443	1.065	0.026	1.034	0.049	2.89%
Oa04	490	1.061	0.013	1.037	0.030	2.19%
Oa05	510	1.035	0.007	1.018	0.007	1.59%
Oa06	560	1.023	0.006	1.010	0.008	1.26%
Oa07	620	1.014	0.005	1.004	0.004	0.95%
Oa08	665	1.017	0.004	1.009	0.004	0.83%
Oa09	674	1.018	0.004	1.011	0.004	0.74%
Oa10	681	1.016	0.004	1.009	0.003	0.64%
Oa11	709	0.999	0.006	0.992	0.007	0.67%
Oa12	754	1.010	0.001	1.008	0.001	0.16%

OSCAR Glitter results

The OSCAR Glitter have been applied to all S3ETRAC glitter data for March 2023. Both OLCI-A and OLCI-B data was processed. The plots in Figure 83 are the glitter results for OLCI-A and OLCI-B for the period of March 2023 and on Figure 84 for all results of 2023 (also provided in Table 5). The values are in absolute terms, since all bands are referenced to the Rayleigh result of band Oa8. The glitter method is a relative inter-band calibration method, since the Oa8 band is used to estimate windspeed. By multiplying all band results with the Rayleigh calibration factor for the same period, the results are referenced to the results of this method.

For this month, only 10 (S3A) and 7 (S3B) individual glitter results are available, therefore the differences between both sensors are larger than expected and compared to the values of the entire 2023 dataset.

For all results of 2023, the difference between OLCI-A and OLCI-B (Table 5, in %) is below 1% for all bands, except for bands Oa04 and Oa05. It also indicates a brighter OLCI-A compared to OLCI-B.

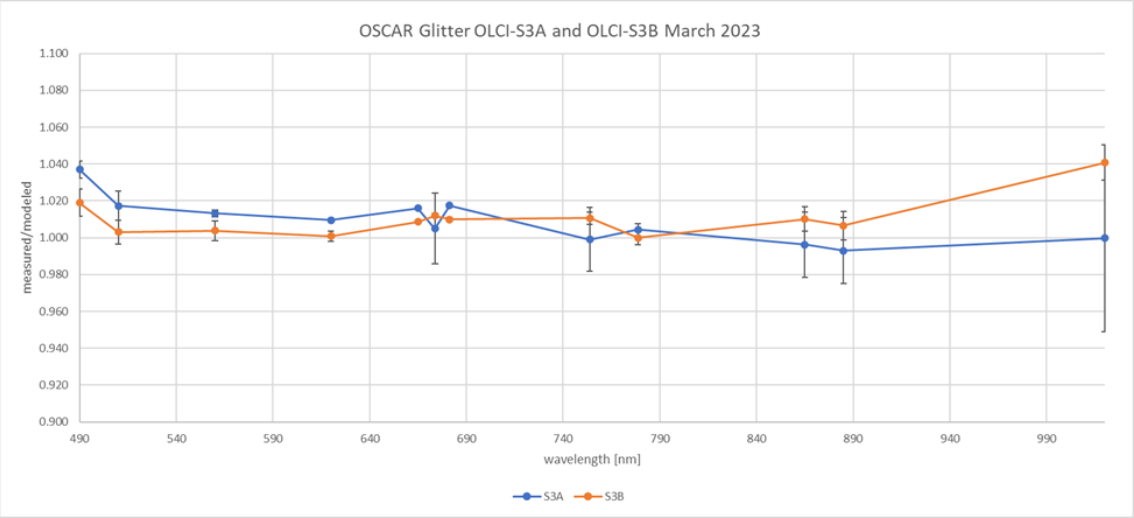

Figure 83: OSCAR Glitter OLCI-A & OLCI-B Calibration results as a function of wavelength for March 2023. The results are obtained with a new climatology derived from CMEMS OLCI monthly CHL products.

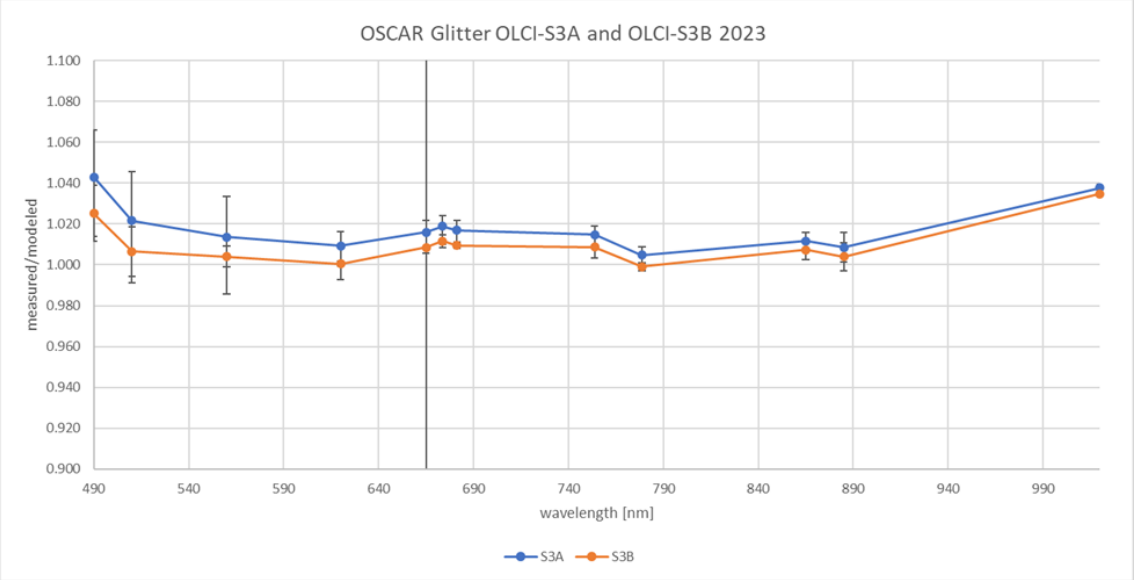

Figure 84: OSCAR Glitter OLCI-A & OLCI-B Calibration results as a function of wavelength for all acquisitions of 2023. The results are obtained with a new climatology derived from CMEMS OLCI monthly CHL products.

Table 5: OSCAR Glitter calibration results for OLCI-A and OLCI-B (average and standard deviation over all acquisitions of 2023) currently processed with the new climatology and observed difference (in %)

OLCI band	Wavelength (nm)	Oscar Glitter OLCIA		Oscar Glitter OLCIB		% difference OLCIA and OLCIB
		avg	stdev	avg	stdev	
Oa04	490	1.043	0.007	1.025	0.007	1.72%
Oa05	510	1.022	0.004	1.006	0.004	1.48%
Oa06	560	1.014	0.003	1.004	0.003	0.94%
Oa07	620	1.009	0.001	1.000	0.001	0.87%
Oa08	665	1.016	0.000	1.009	0.000	0.73%
Oa09	673.75	1.019	0.001	1.012	0.001	0.71%
Oa10	681.25	1.017	0.001	1.010	0.001	0.72%
Oa12	753.75	1.015	0.002	1.009	0.004	0.61%
Oa16	778.75	1.005	0.002	0.999	0.003	0.57%
Oa17	865	1.012	0.004	1.007	0.007	0.43%
Oa18	885	1.009	0.004	1.004	0.008	0.45%
Oa21	1020	1.038	0.006	1.035	0.013	0.29%

3.1.4 Radiometric validation with Moon observations

There has been no new result during the reporting period. Last figures (reported in Data Quality Report for February 2022) are considered valid.

4 Level 2 Land products validation

4.1 [OLCI-L2LRF-CV-300]

4.1.1 Routine extractions

- The focus for this time period has been on the rolling archive Non Time Critical (NT) data until the 31st of July 2022. More data available for statistical analysis as a concatenation procedure for all available data in the MERMAID processing has been implemented.
- Concatenated time series of OLCI Global Vegetation Index and OLCI Terrestrial Chlorophyll Index have been regenerated on the current rolling archive availability including previous extractions since June 2016 and April 2018 for S3A and S3B respectively.

4.1.1.1 OLCI-A

Figure 85 to Figure 94 below present the Core Land Sites OLCI-A time series over the current period.

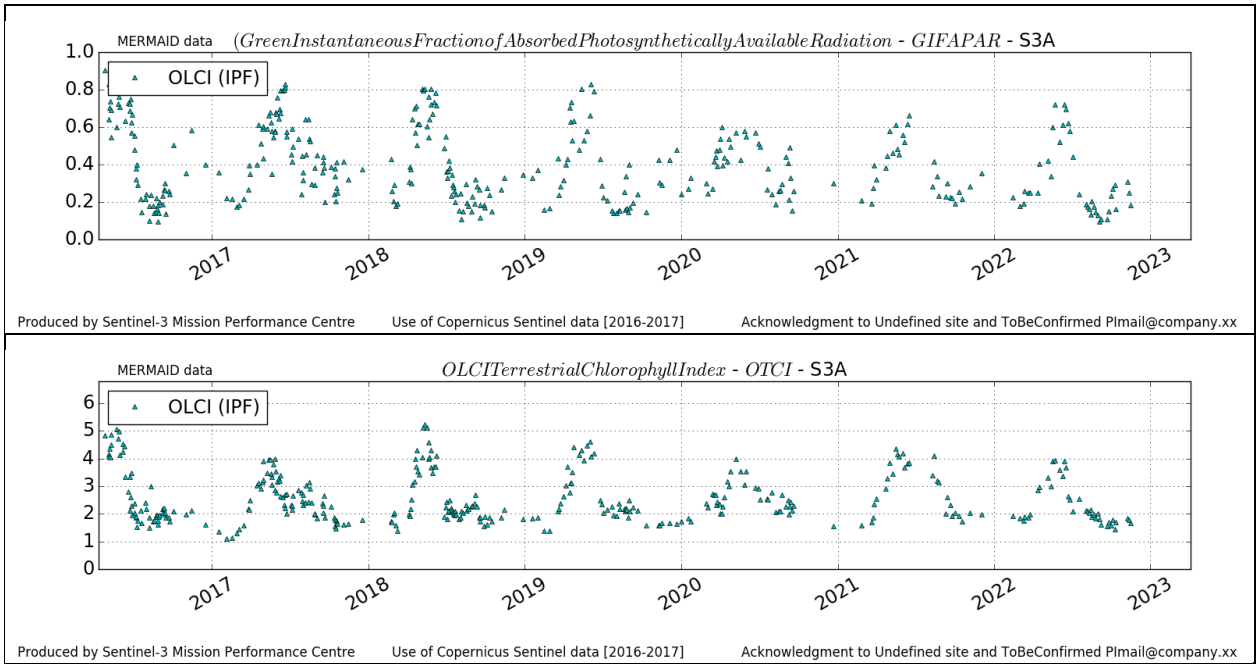

Figure 85: DeGeb time series over current report period

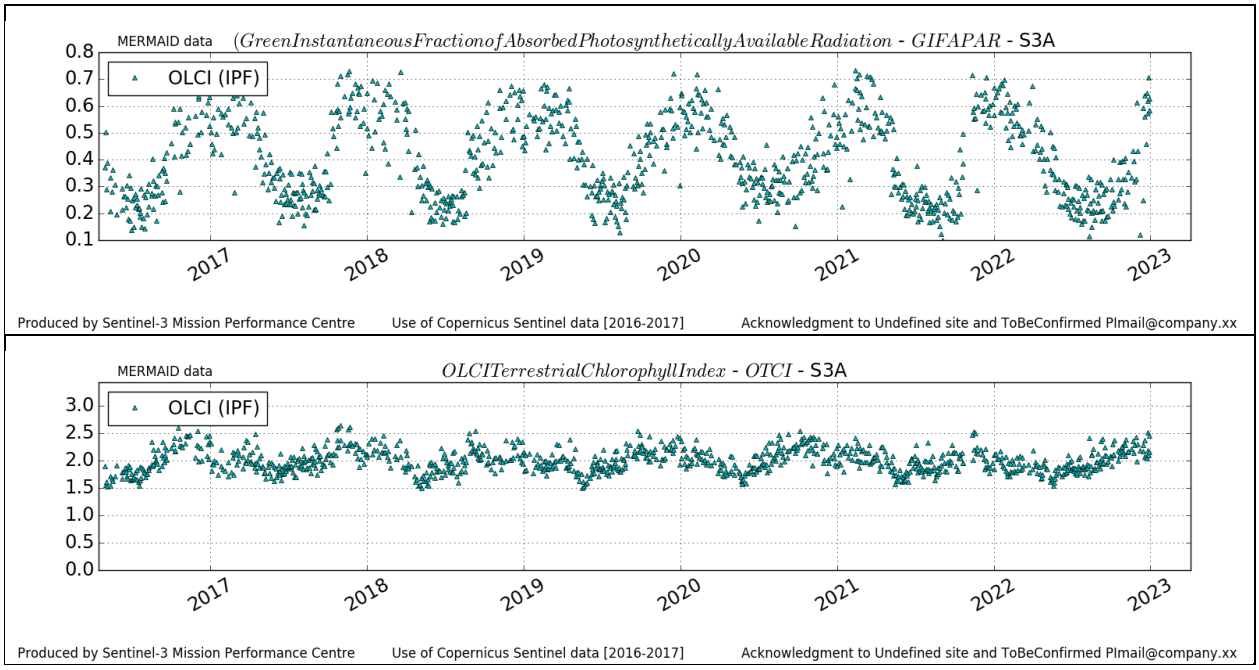

Figure 86: ITCat time series over current report period

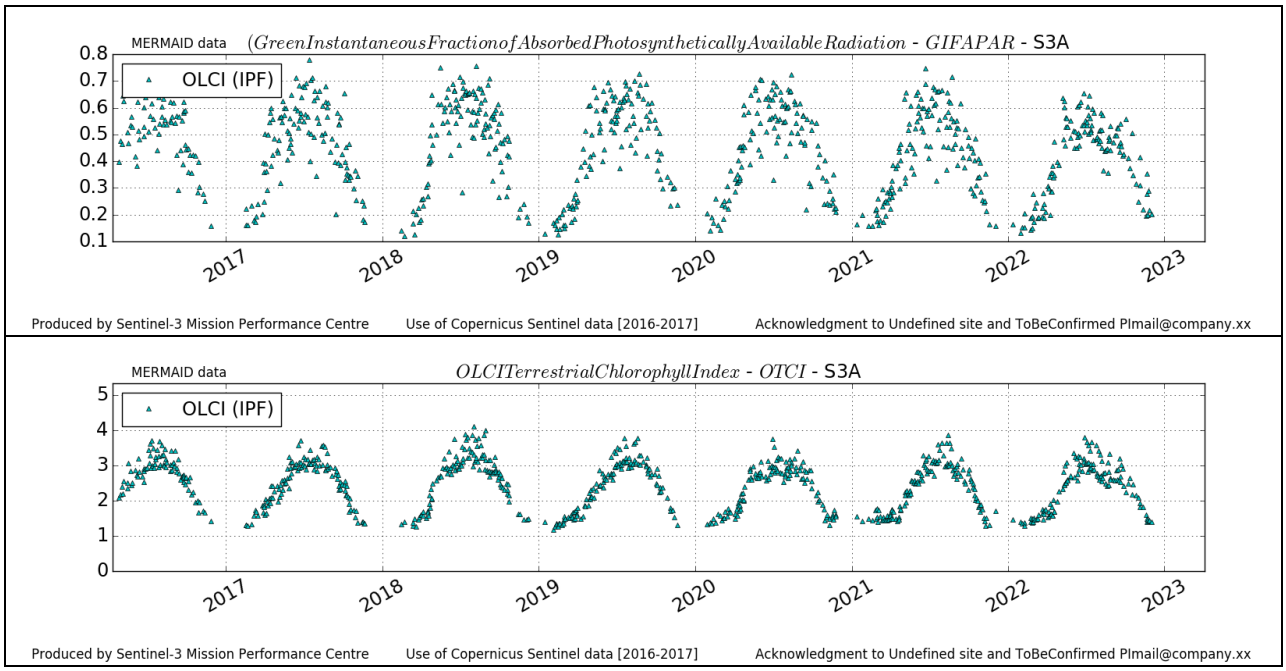

Figure 87: ITIsp time series over current report period

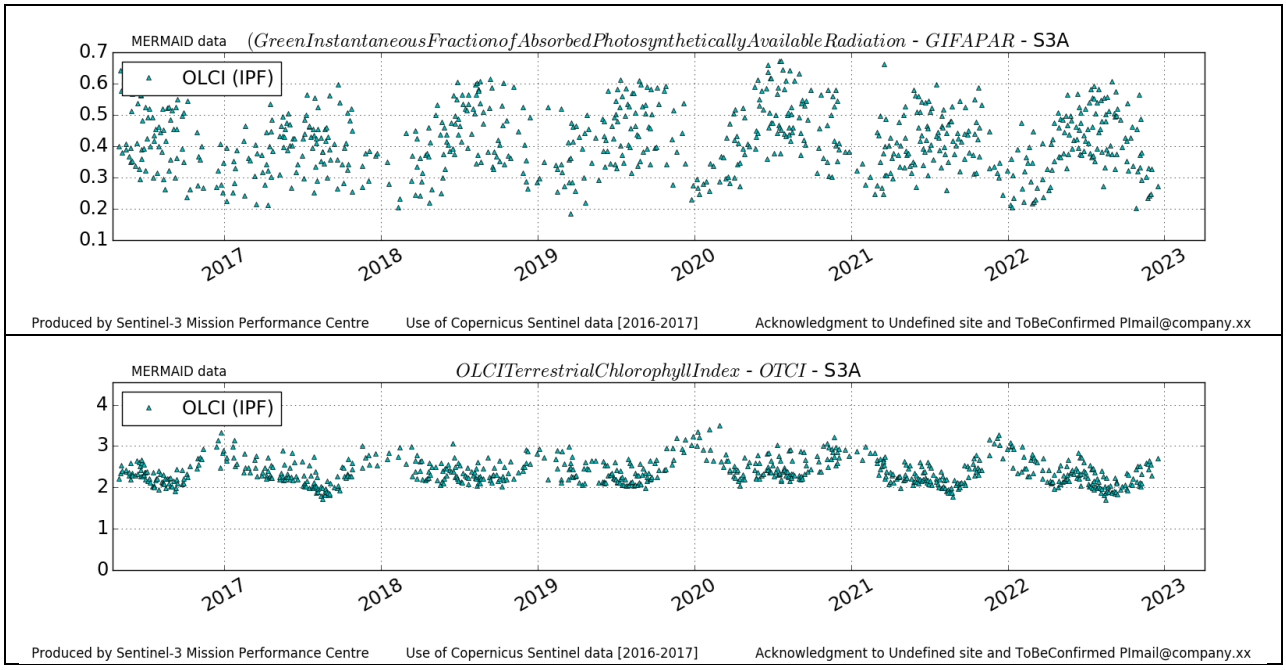

Figure 88: ITSro time series over current report period

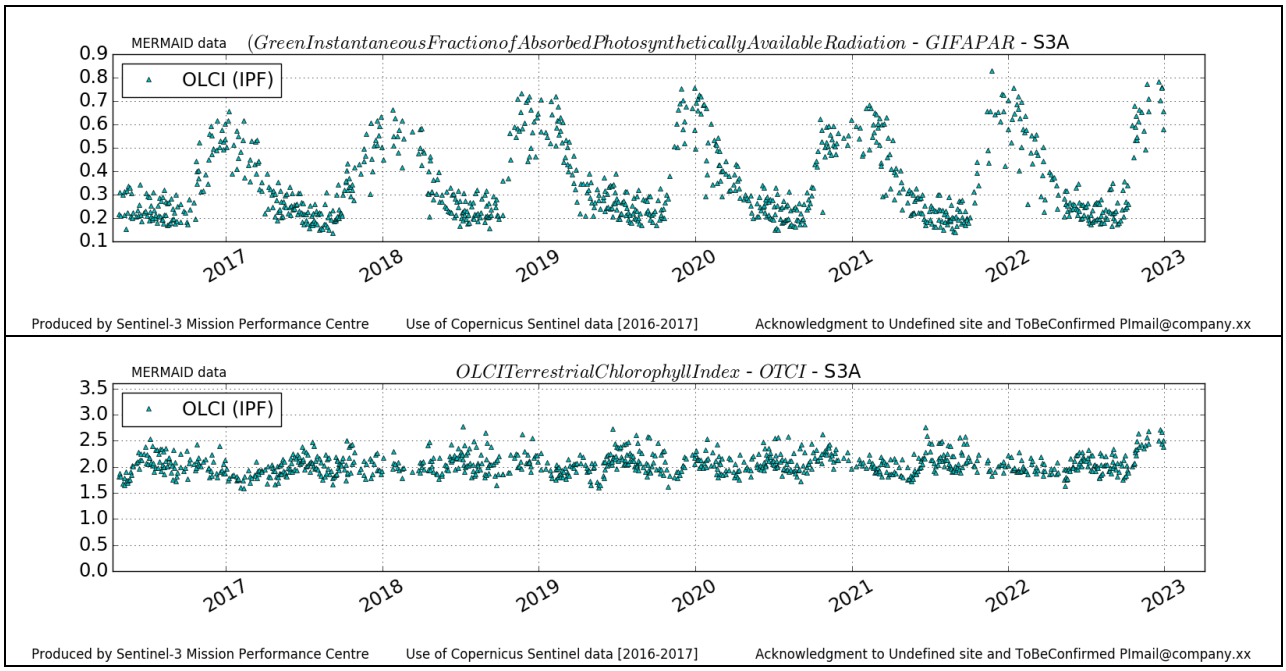

Figure 89: ITTra time series over current report period

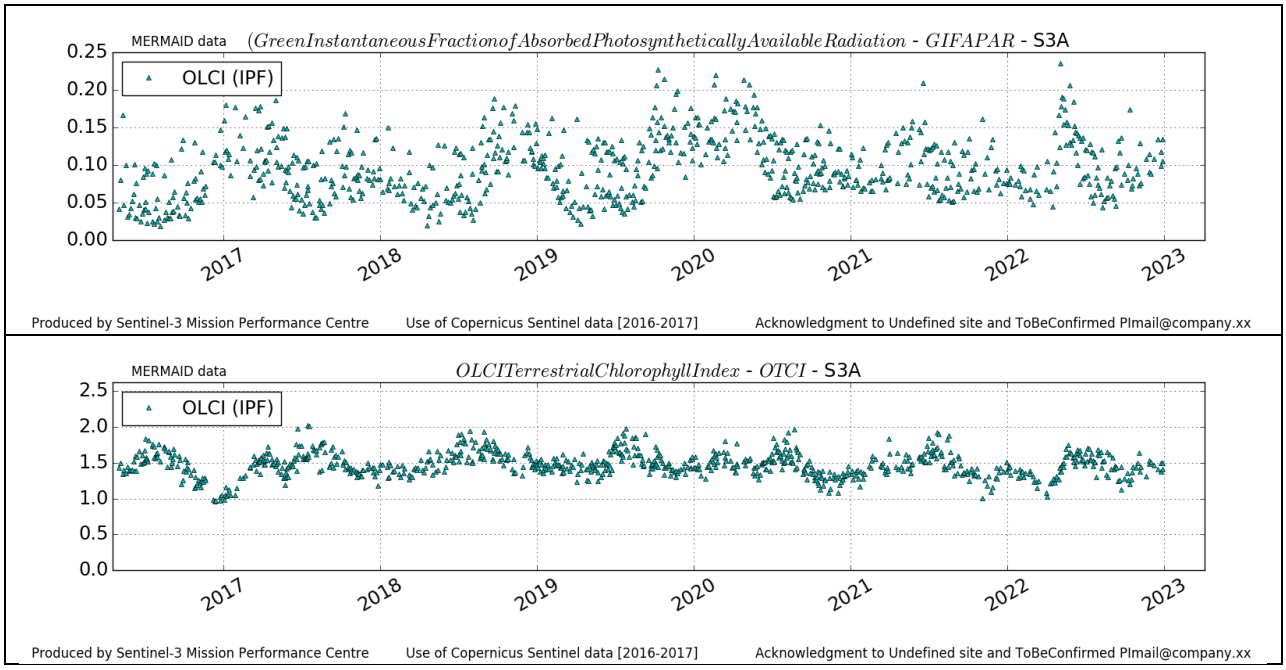

Figure 90: SPAli time series over current report period

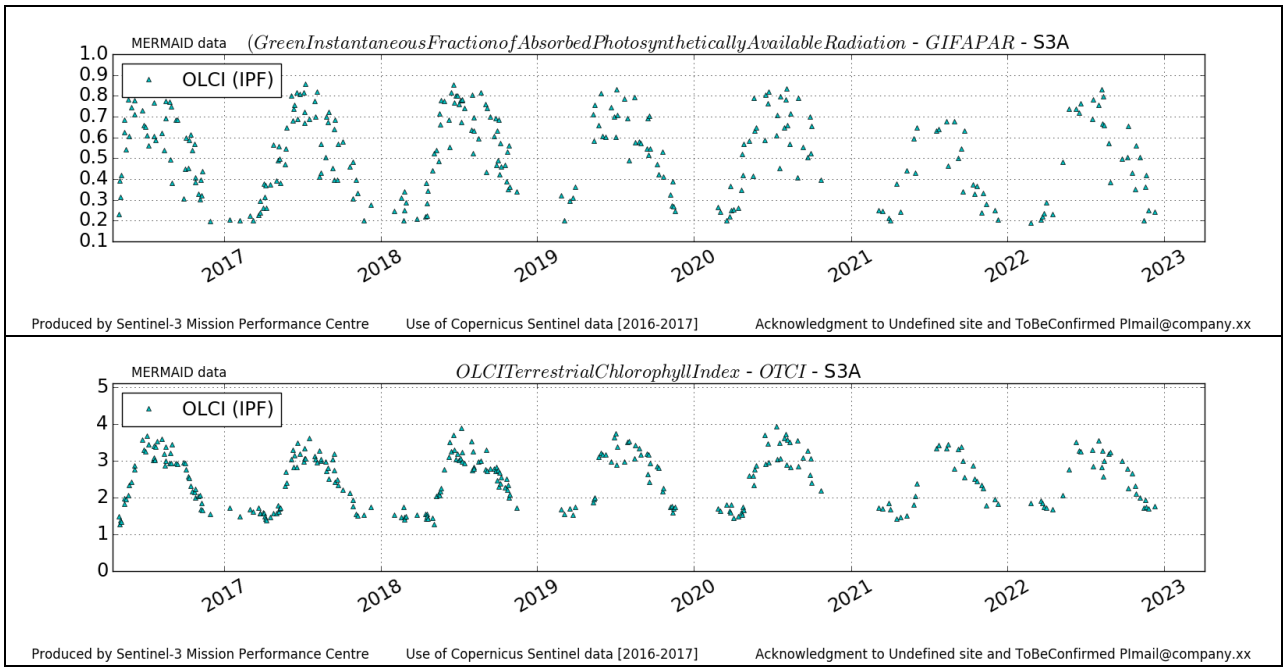

Figure 91: UKNFo time series over current report period

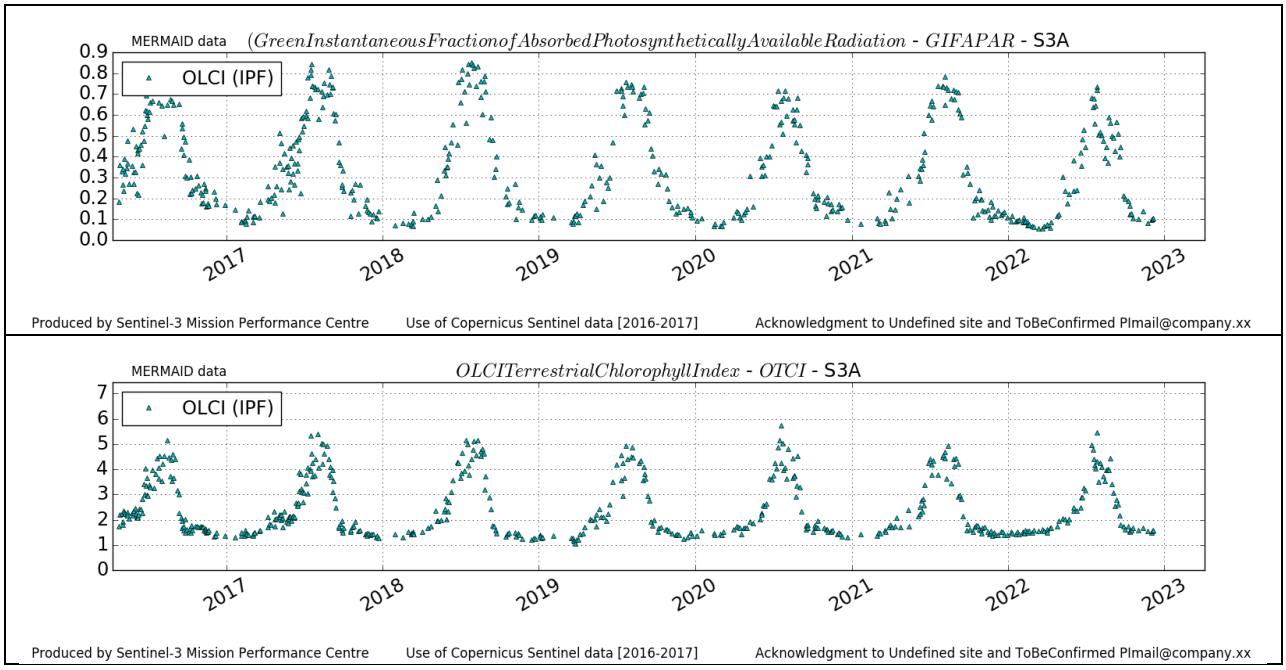

Figure 92: USNe1 time series over current report period

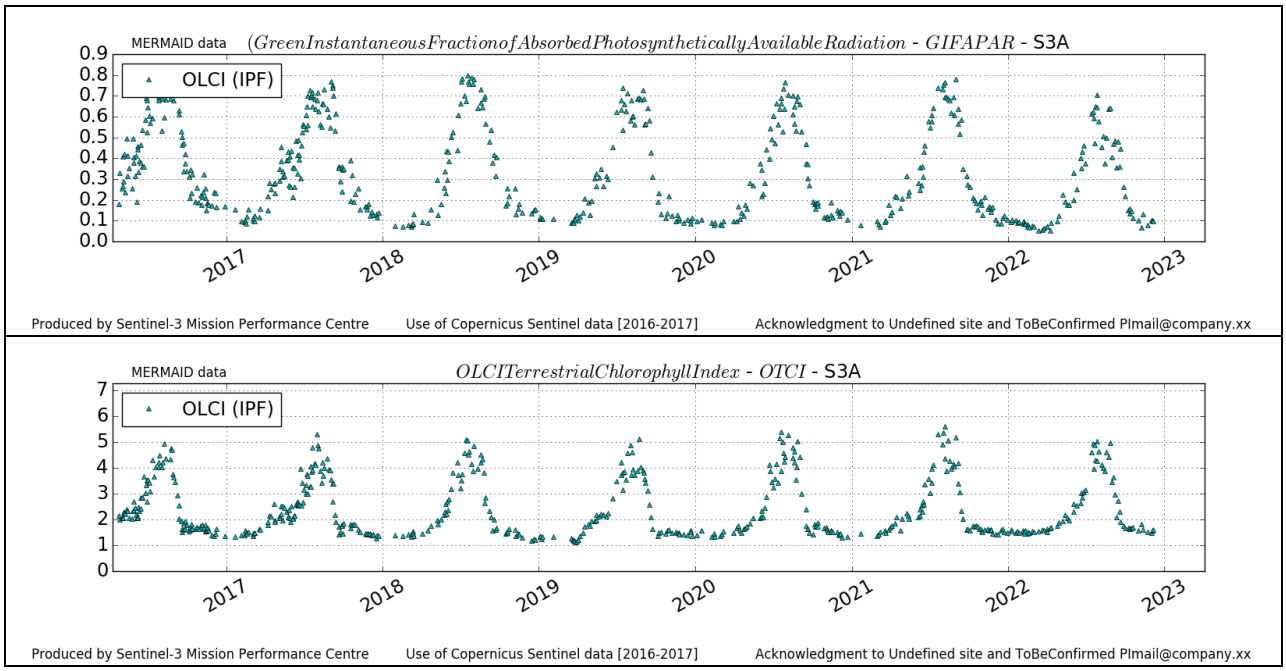

Figure 93: USNe2 time series over current report period

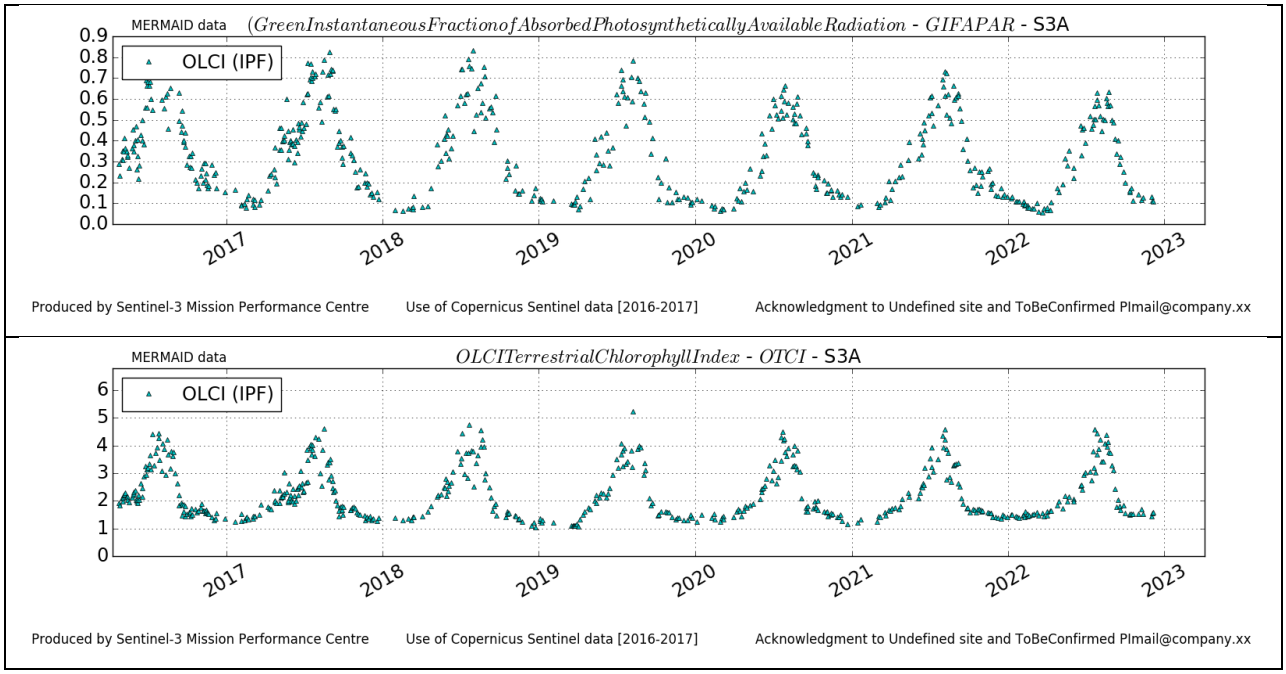

Figure 94: USNe3 time series over current report period

4.1.1.2 OLCI-B

Figure 95 to Figure 104 below present the Core Land Sites OLCI-B time series over the current period.

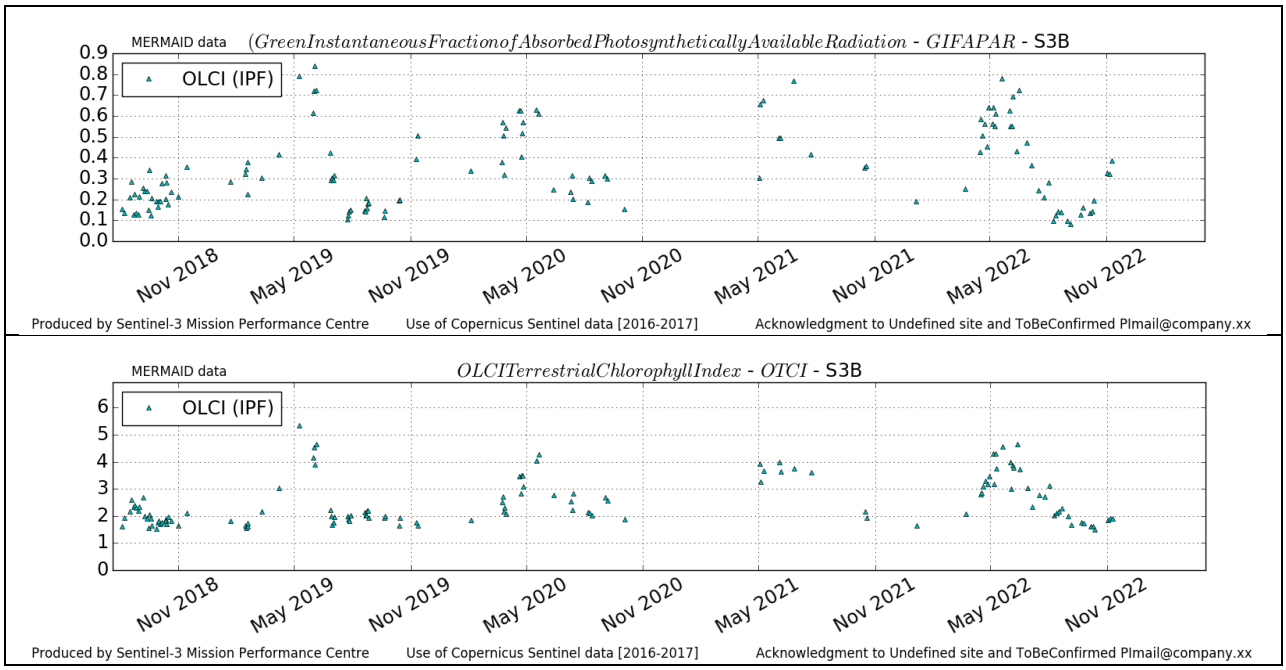

Figure 95: DeGeb time series over current report period

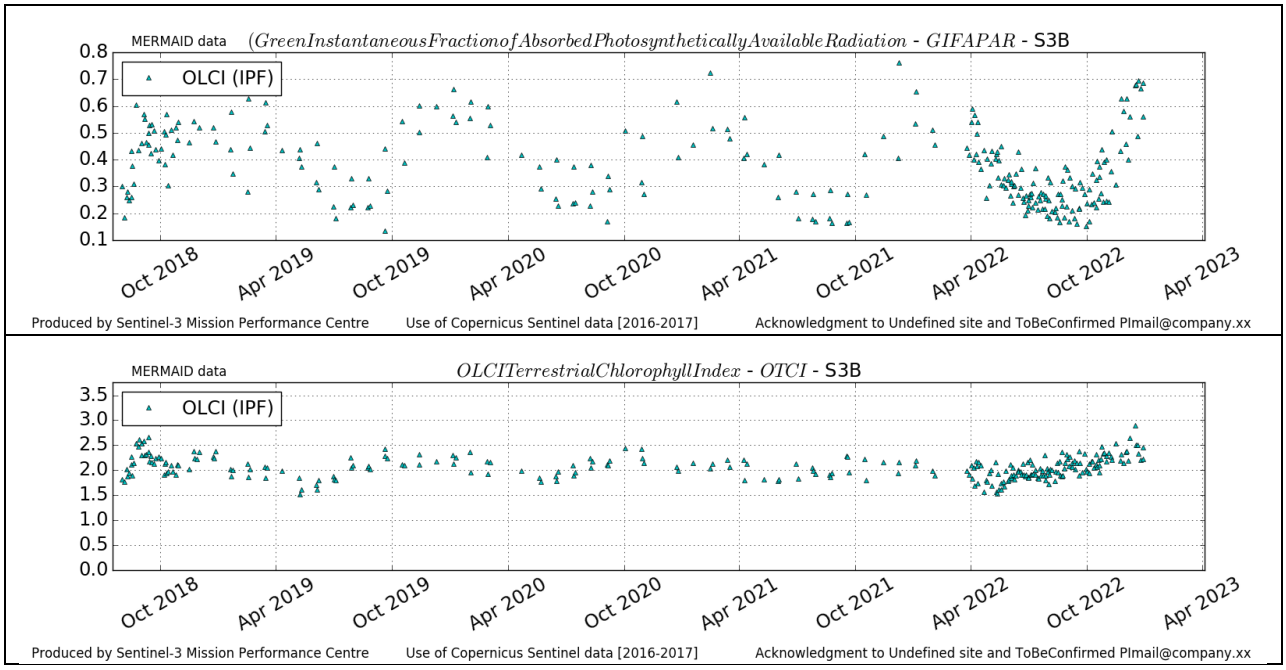

Figure 96: ITCat time series over current report period

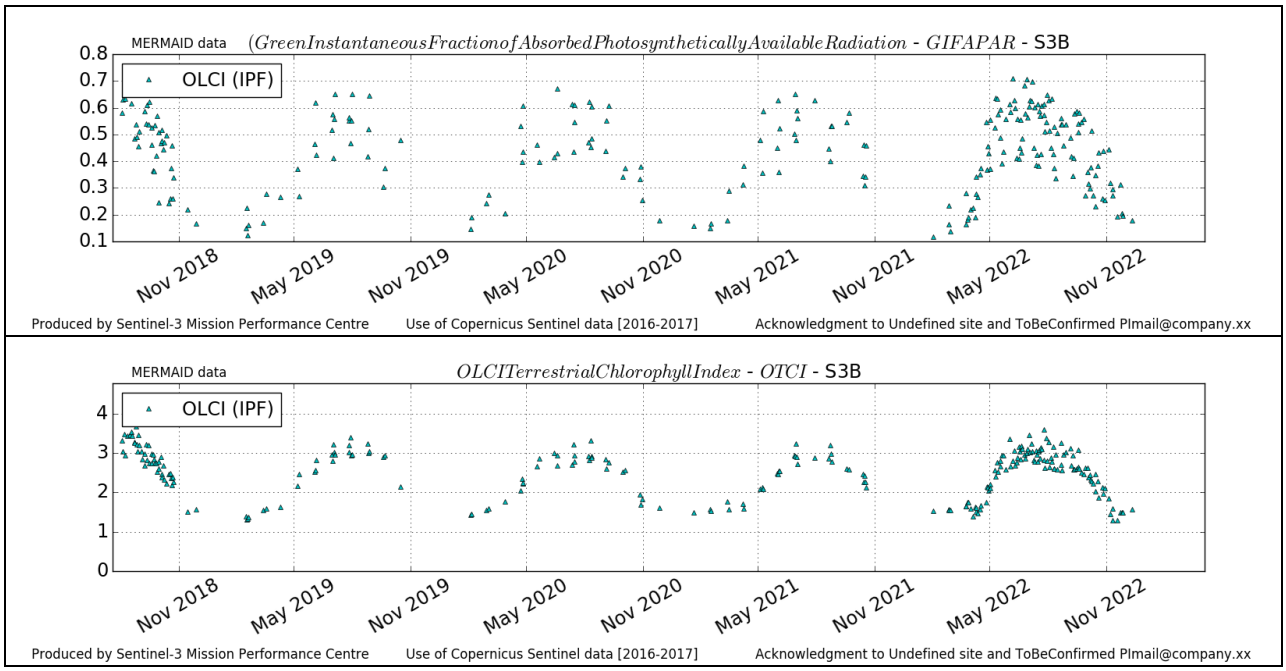

Figure 97: ITIsp time series over current report period

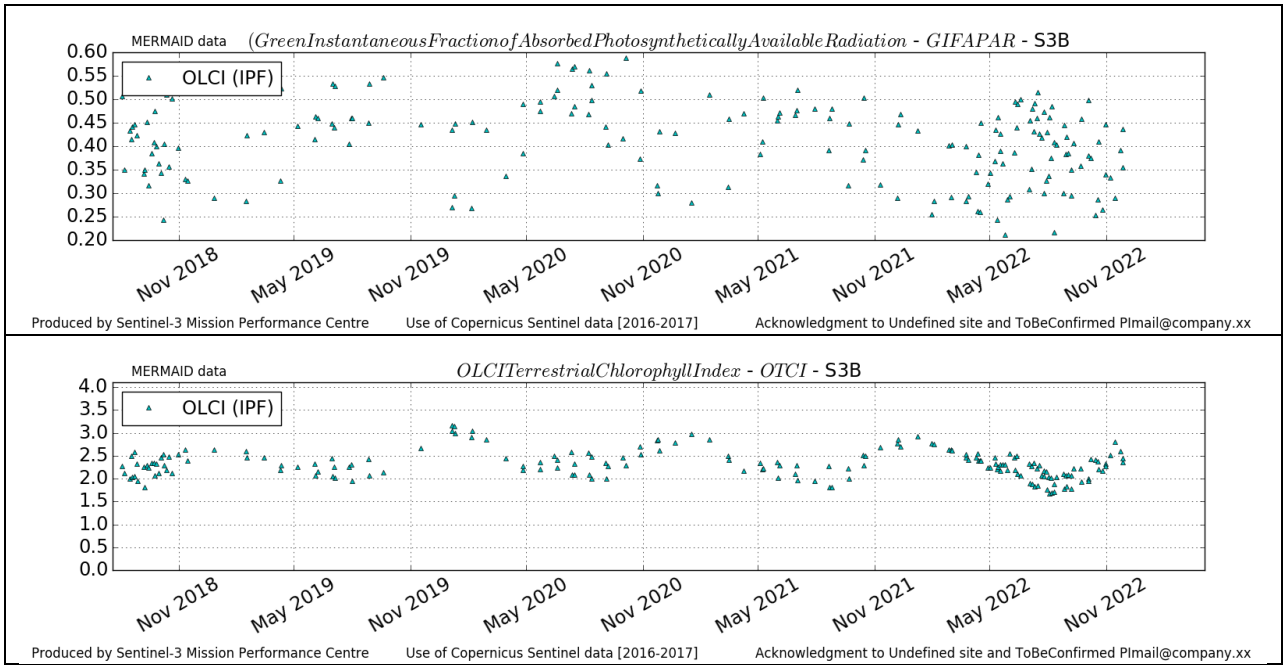

Figure 98: ITSro time series over current report period

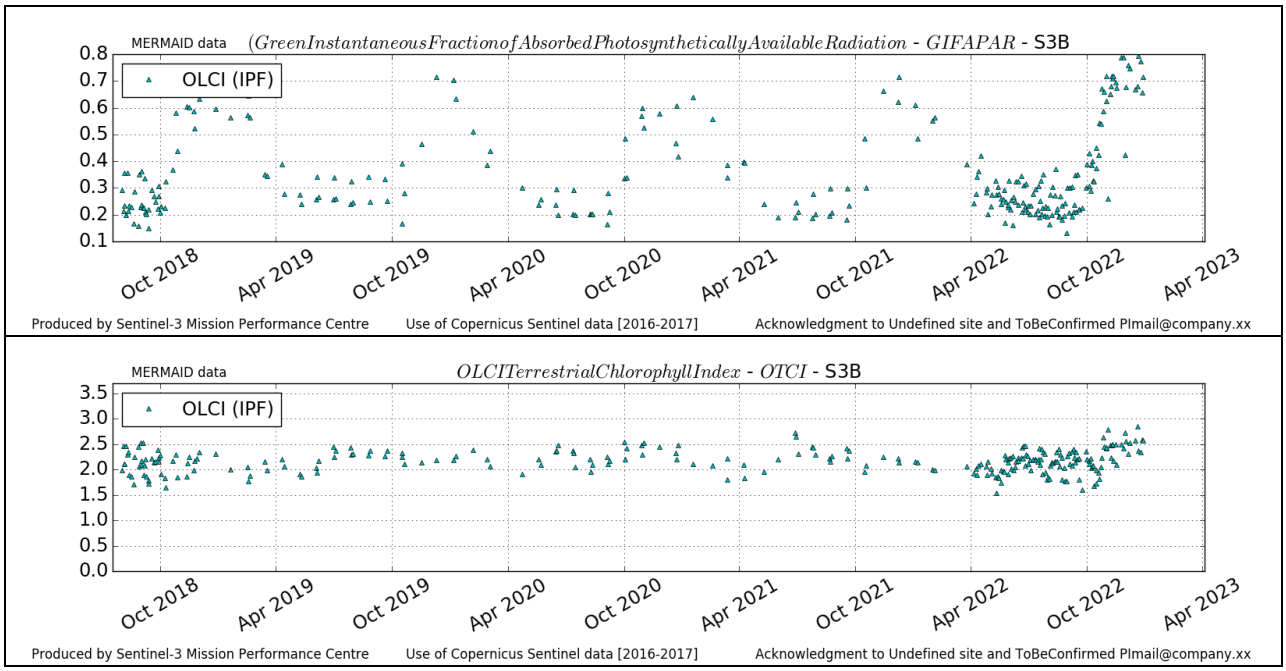

Figure 99: ITTra time series over current report period

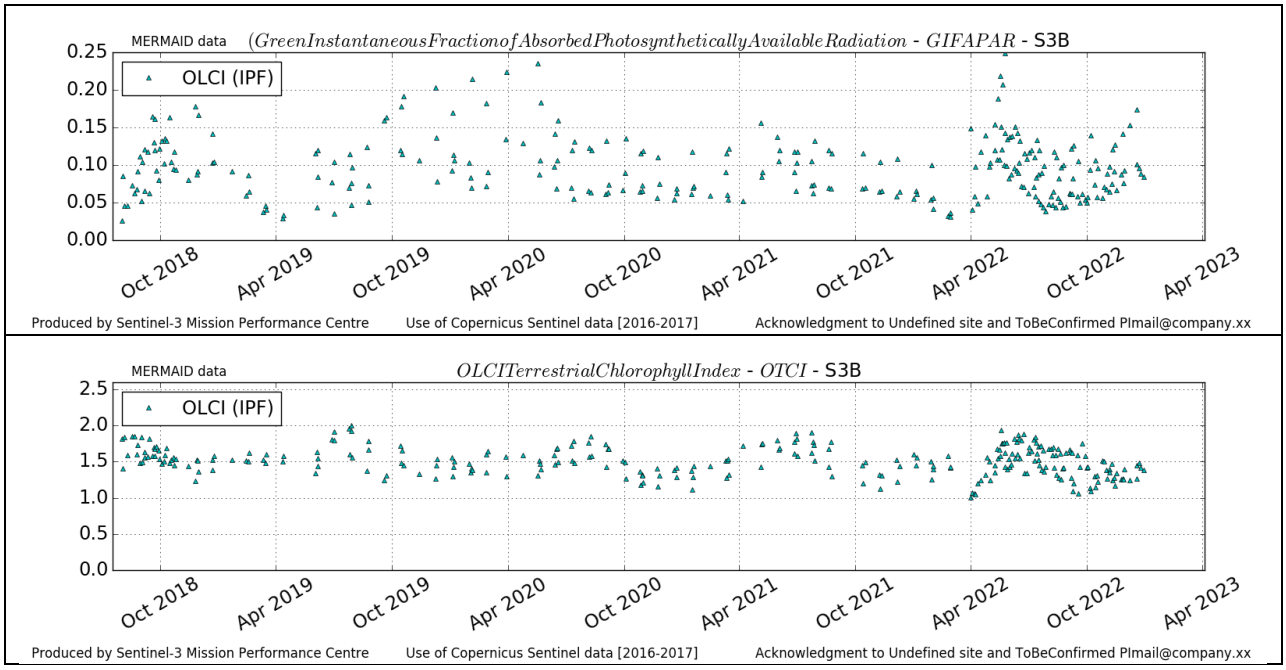

Figure 100: SPAli time series over current report period

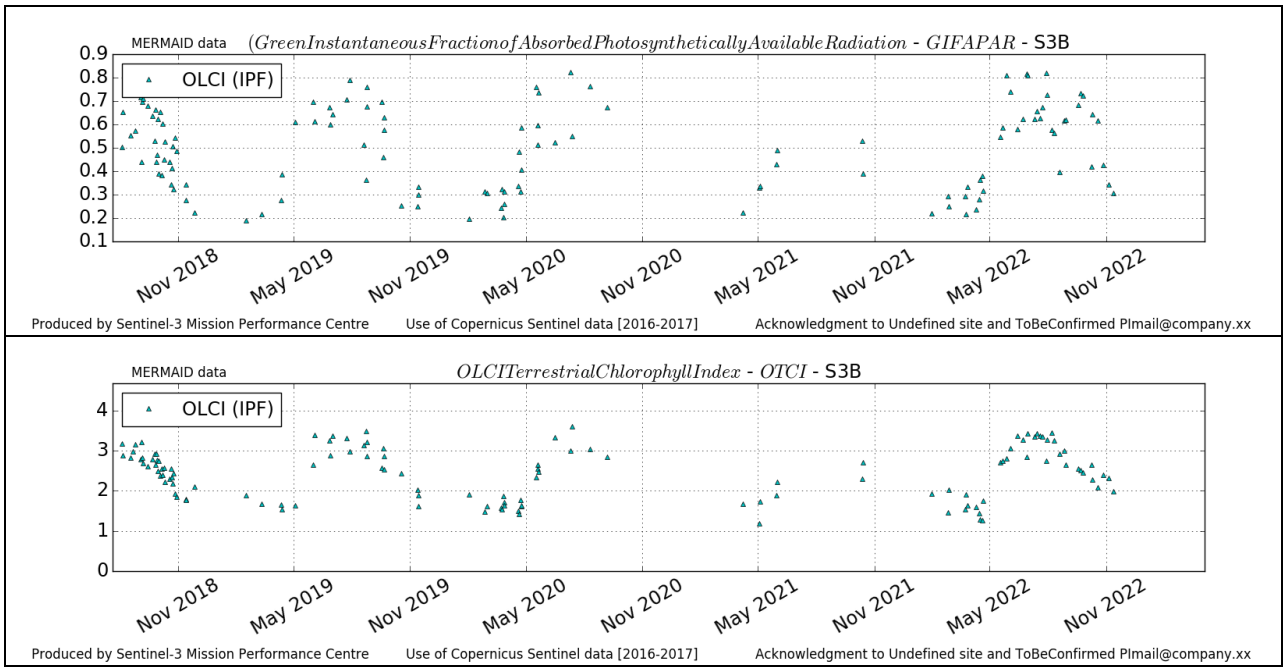

Figure 101: UKNFo time series over current report period

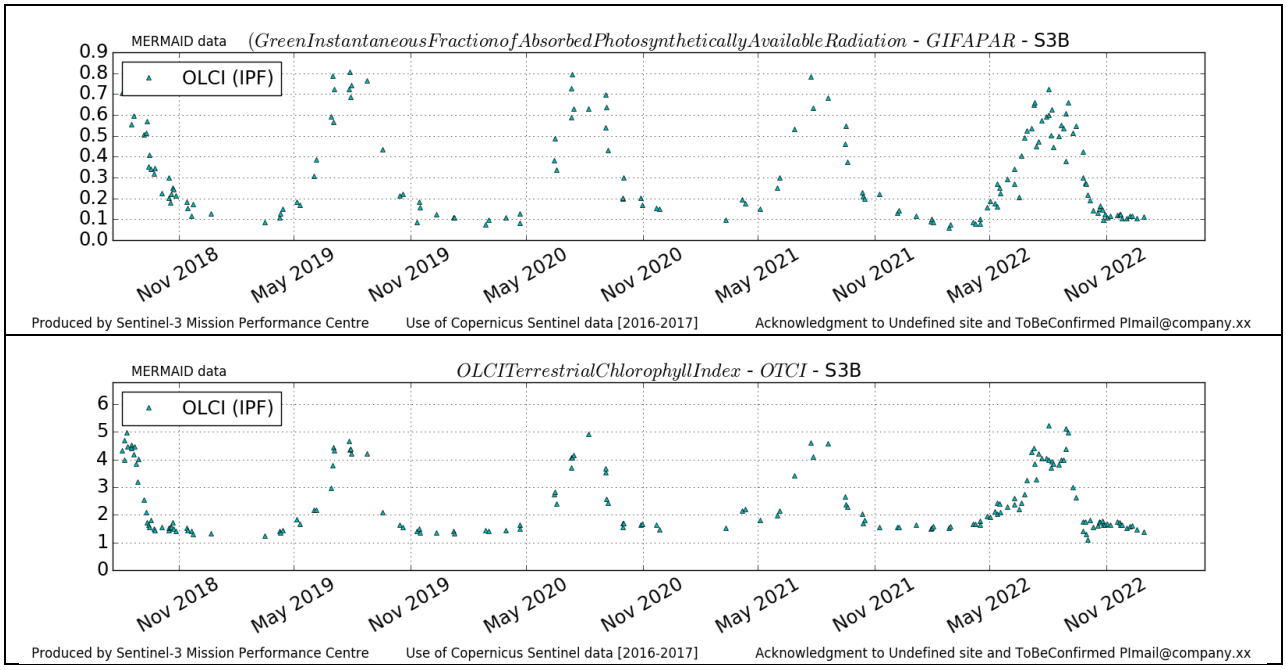

Figure 102: USNe1 time series over current report period

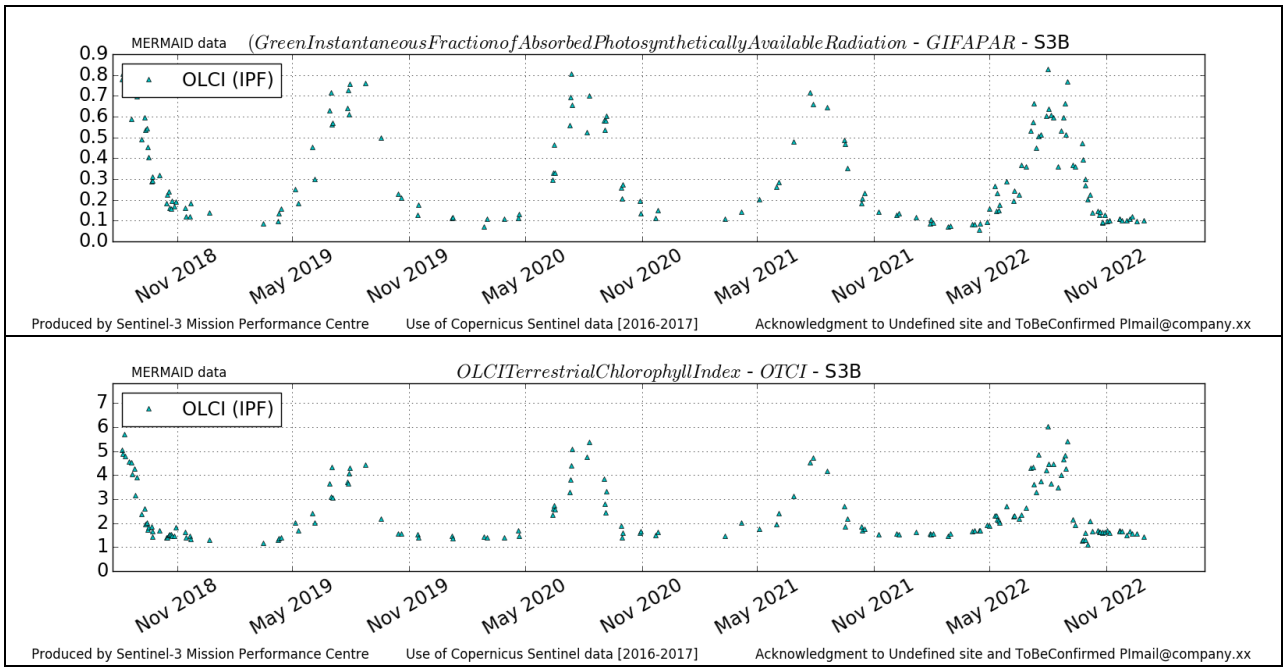

Figure 103: USNe2 time series over current report period

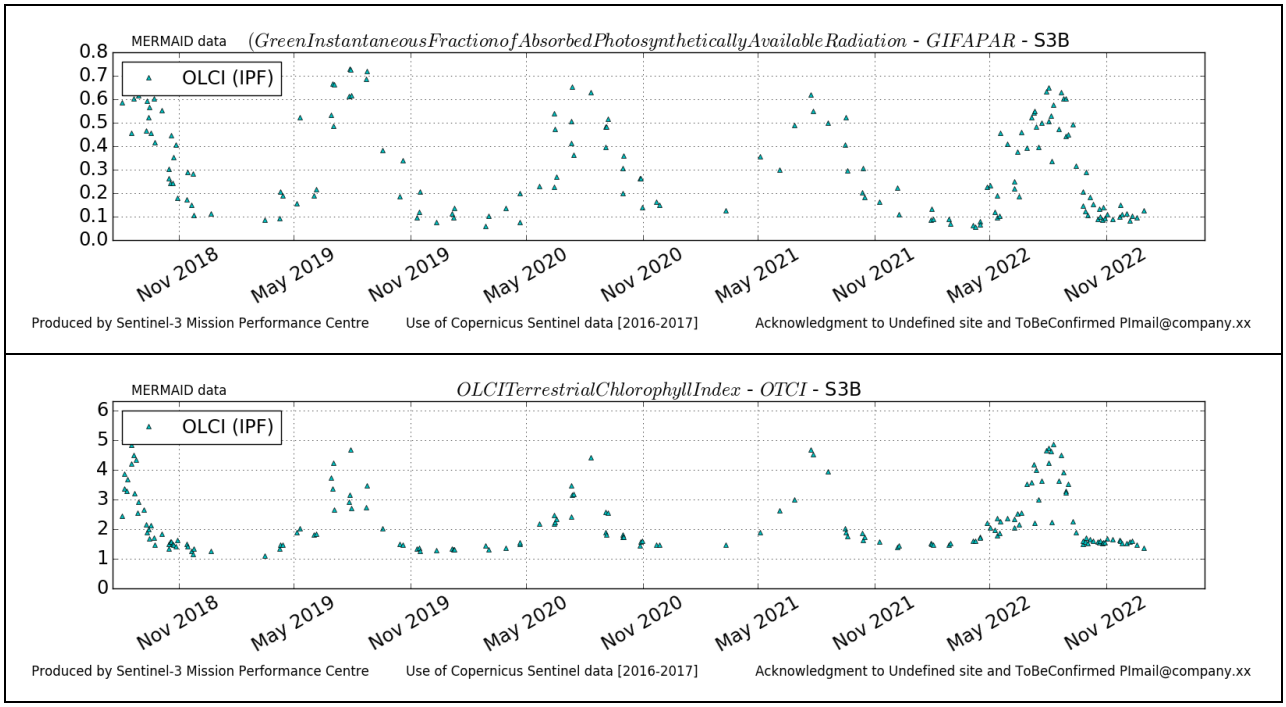

Figure 104: USNe3 time series over current report period

4.1.2 Comparisons with MERIS MGVI and MTCI climatology

There has been no new result during the reporting period. Last figures (reported in OLCI Data Quality Report covering May 2022) are considered valid.

4.1.3 Comparisons with GBOV (Ground-Based Observations for Validation) data v3

There has been no new result during the reporting period. The last figures (reported in OLCI Data Quality Report covering January 2023) are considered valid.

4.1.4 Sentinel-3A and 3B biophysical variables inter-annual variability results

There has been no new result during the reporting period. The last figures (reported in OLCI Data Quality Report covering February 2023) are considered valid.

4.2 [OLCI-L2LRF-CV-410 & OLCI-L2LRF-CV-420] – Cloud Masking & Surface Classification for Land Products

4.2.1 Sky Camera based validation – prototype results for January 2023

According to the methodology presented in DQR of July 2022, the cloud masking validation results based on Sky Cameras. For the March 2023 reporting a few changes have been made. The prototype validation

results for OLCI cloud mask using sky cameras (SC) are now based on two sites, currently validated independently. The site at La Sapienza University in Rome, Italy is now accompanied by a second SC set at the University of Valencia in Spain.

For the Rome site the validation was switched to SC 2, which is located a few hundred meters away from SC 1. Sky camera 1 had shown some instabilities in azimuth location. Meaning, the camera rotated horizontally over time. The source for this is currently under investigation. SC 2 is stable since the beginning and thus is now used for validation. The coordinates of SC 2 are:

- Lat: 41.90148
- Lon: 12.51575

The coordinates of the location of SC 1 at University of Valenica are:

- Lat: 39.50832
- Lon: -0.42084

Besides the switch of the SC in Rome, new classifiers for the SCs have been trained. The classifiers are now based on a ANN instead of a random forest (RF) classifier, previously used. The accuracy of the ANN classifier is a bit better compared to the RF classifier. Nevertheless, the sun being close to nadir in the SC image still leads to overestimation of clouds in the SC data. A method to hopefully reduce this effect is currently in development.

4.2.1.1 Rome

Figure 113 and Figure 114 show the prototype validation results for the Rome site in March 2023. The weather in March around Rome got a lot more arid with only half of the month's days being clouded (see Figure 105). The average rainfall for March is between 3 to 8 days, with 4 days between 1st and 31st of March 2023 (see Figure 106).

Figure 105: Temperature and cloud cover Rome, March 2023 (source: https://world-weather.info/forecast/italy/rome/March-2023/)

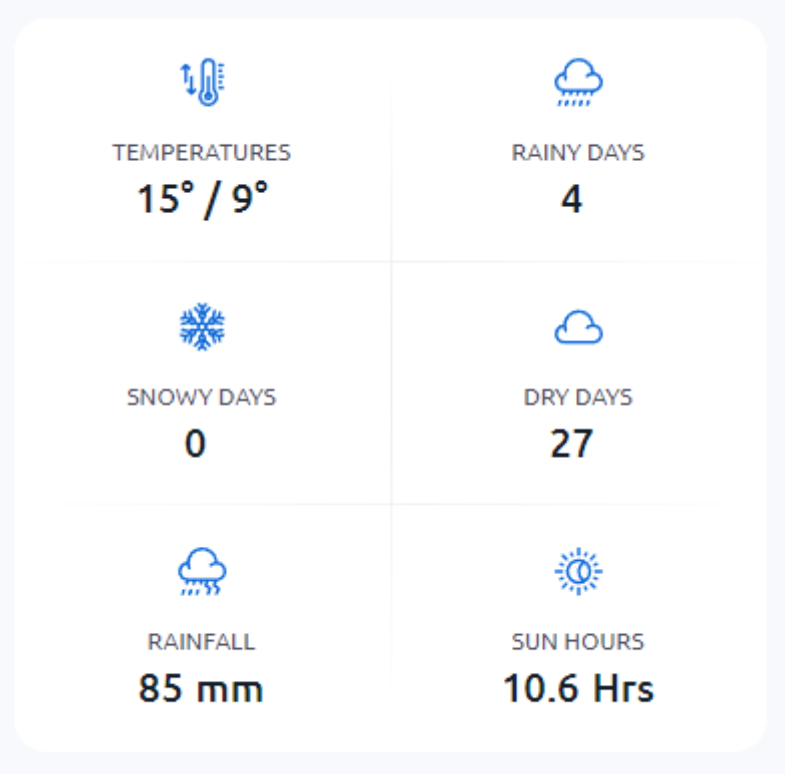

Figure 106: Average temperature, rainy days, and rainfall over Rome, March 2023 (source: https://www.weather25.com/europe/italy/lazio/rome?page=month&month=March)

Since the February 2022 analysis a few changes have been made to the prototype SC validation. First it was switched to SC 2 instead of SC 1, due to some geometrical instabilities. Then the classifier was switched to using an ANN instead of a random forest classifier. Additionally, new training data was collected to improve the results of the NN.

A little below 50% of the SC observation show clear sky conditions (see Figure 107). Some SC classifications, like on 13th, 15th or 16th of March seem to overestimate cloud coverage from the SC classification due to sun interference. Making the March reference a bit cloud sky biased.

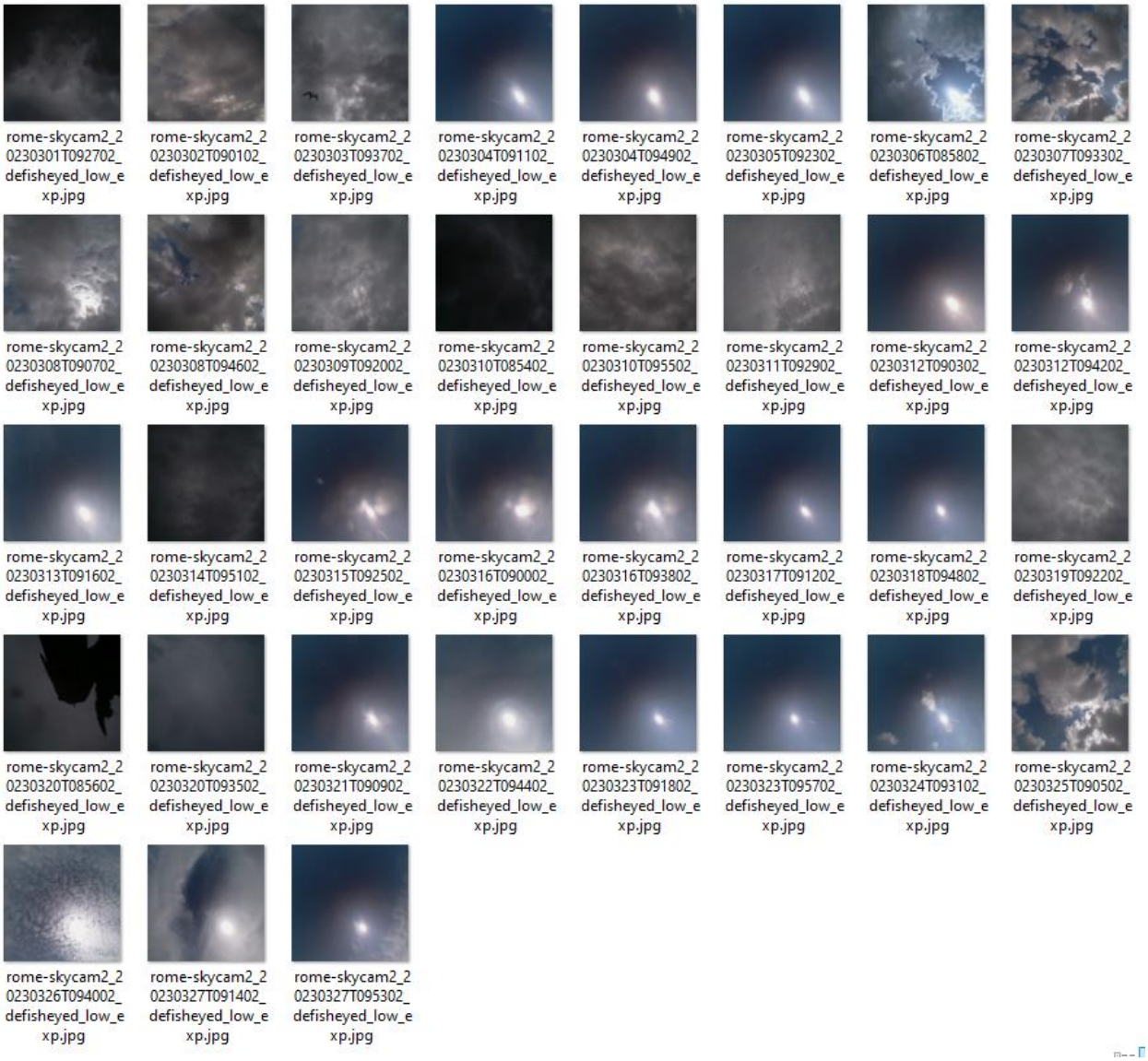

Figure 107: Sky camera acquisitions over Rome during Sentinel-3 OLCI overpass

Figure 108: Classified sky camera acquisitions over Rome during Sentinel-3 OLCI overpass

Figure 109 to Figure 112 show comparisons between OLCI L1, the sky camera (SC) image and the SC classification. Where Figure 111 shows an example of over detection of clouds with the SC approach, the other comparisons show that there is a good amount of thin transparent clouds present in the OLCI acquisitions. Therefore, the SC classification seems explainable, even though it is also caused by the sun interference, it is a combination of this effect and the thin clouds in the atmosphere.

Figure 109: Comparison between OLCI L1 (SC position marked as Pin1), SC image and SC classification for 13th of March overpass of OLCI-A

Figure 110: Comparison between OLCI L1 (SC position marked as Pin1), SC image and SC classification for 15th of March overpass of OLCI-B

Figure 111: Comparison between OLCI L1 (SC position marked as Pin1), SC image and SC classification for 16th of March overpass of OLCI-B

Figure 112: Comparison between OLCI L1 (SC position marked as Pin1), SC image and SC classification for 16th of March overpass of OLCI-A

The distribution between clear and cloud observations is a bit uneven during March. But as described above, the SC classification seems to have a small cloud bias.

Figure 113 shows the validation results for the OLCI cloud flags including the margin. Only OLCI observations with a OZA below 30 have been considered to lower the influence of parallax between the OLCI observation and the SC observation. This time the SC suffers a little bit from a cloud bias as explained above.

When neglecting the margin (see Figure 114) the performance is equal this time. This seems to be mostly caused by reducing the comparisons to OLCI observations with OZA below 30 degrees.

ɔme SC 2 autom. classif. vs. OLCI L2 LFR Cloud & Ambiguous & Margin - March 202

Sky Camera 1

OLCI L2 LFR	Clear	Cloud	Sum	U A	E
CLEAR	3	6	9	33.3	66.7
CLOUD	0	11	11	100.0	0.0
Sum	3	17	20		
P A	100.0	64.7		OA:	70.0
E	0.0	35.3		BOA:	82.35

Scotts Pi: 0.285
Krippendorfs alpha: 0.303
Cohens kappa: 0.354

Figure 113: Confusion matrix showing validation results for OLCI L2 cloud screening including margin against SC1 automated classification.

Rome SC 2 autom. classif. vs. OLCI L2 LFR Cloud & Ambiguous - March 2023

Sky Camera 1

OLCI L2 LFR

Class	Clear	Cloud	Sum	U A	E
CLEAR	3	6	9	33.3	66.7
CLOUD	0	11	11	100.0	0.0
Sum	3	17	20		
P A	100.0	64.7		OA:	70.0
E	0.0	35.3		BOA:	82.35

Scotts Pi: 0.285
Krippendorfs alpha: 0.303
Cohens kappa: 0.354

Figure 114: Confusion matrix showing validation results for OLCI L2 cloud screening excluding margin against SC1 automated classification.

4.2.1.2 Valencia

Figure 119 and Figure 120 show the prototype validation results for the Valencia site in March 2023. The weather in March around Valencia is very arid, but with a good amount of cloud covered days (see Figure 115). The average rainfall for March is between 3 to 8 days, with 0 days between 1st and 31st of March 2023 (see Figure 116).

Figure 115: Temperature and cloud cover Valencia, March 2023 (source: https://world-weather.info/forecast/spain/valencia/march-2023/)

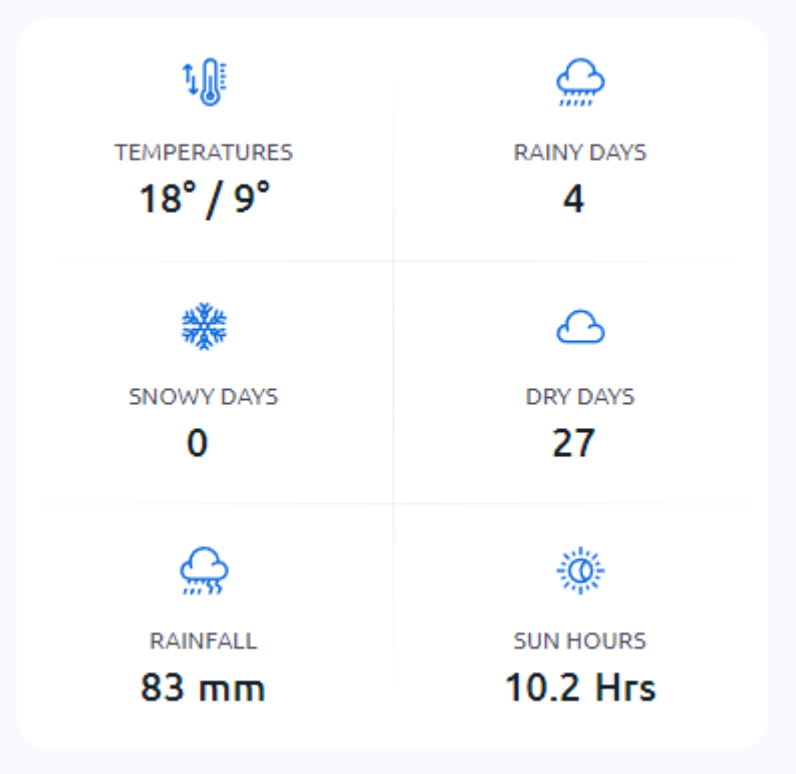

Figure 116: Average temperature, rainy days, and rainfall over Valencia, March 2023 (source: https://www.weather25.com/europe/spain/comunidad-valenciana/valencia?page=month&month=March)

The Valencia site is reported for the first time in this report. The classifier is also based on an ANN. Training data was collected specifically for the camera to train the NN.

Around 60% of the SC observations show clear sky conditions (see Figure 117). One observation is blocked by a bird. Even though, there is the sun close to the centre of all acquisitions, the SC classification (see Figure 118) does not show a huge cloud bias. Therefore, the NN of the Valencia SC1 seems quite robust against sun interference.

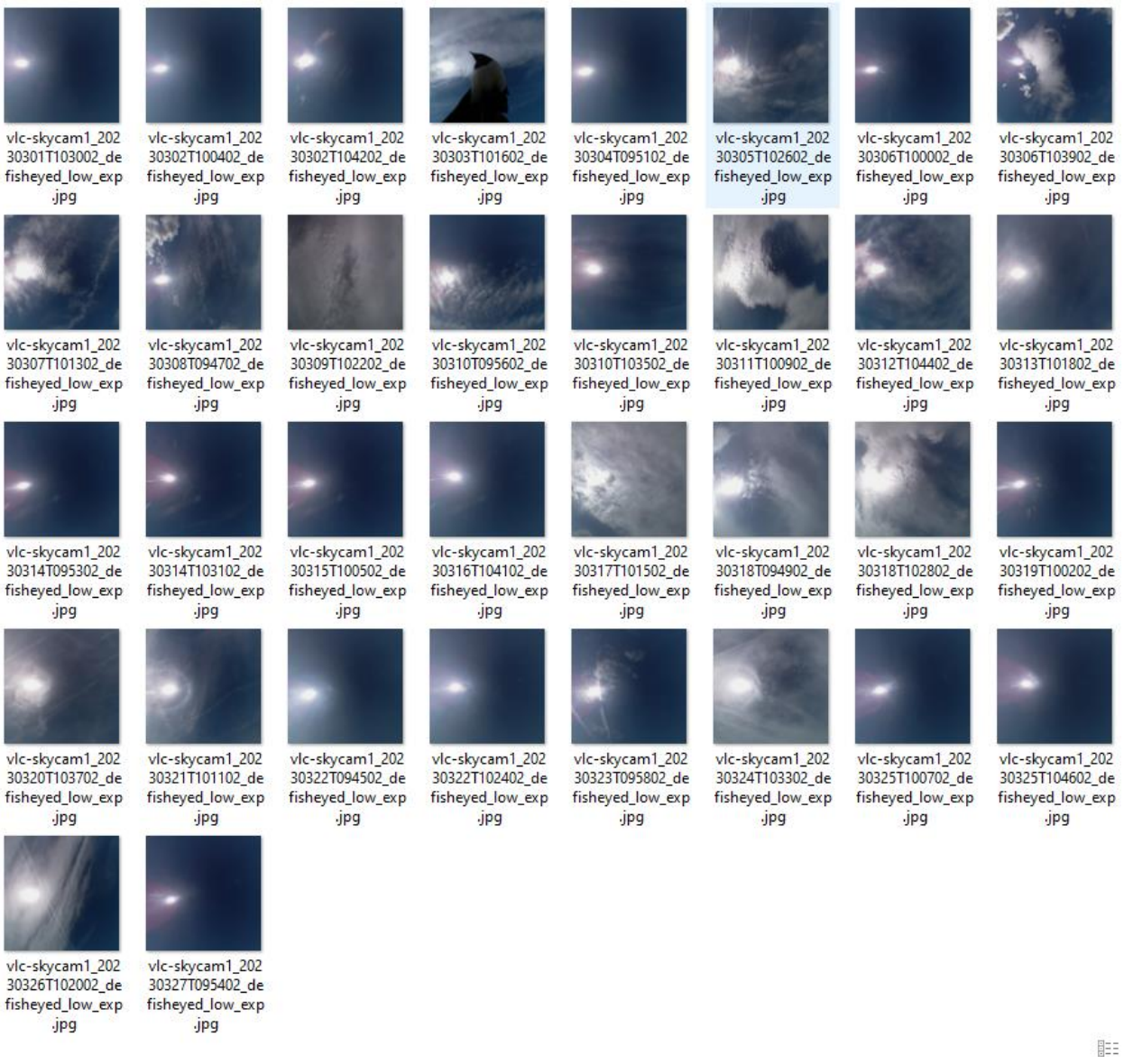

Figure 117: Sky camera acquisitions over Rome during Sentinel-3 OLCI overpass

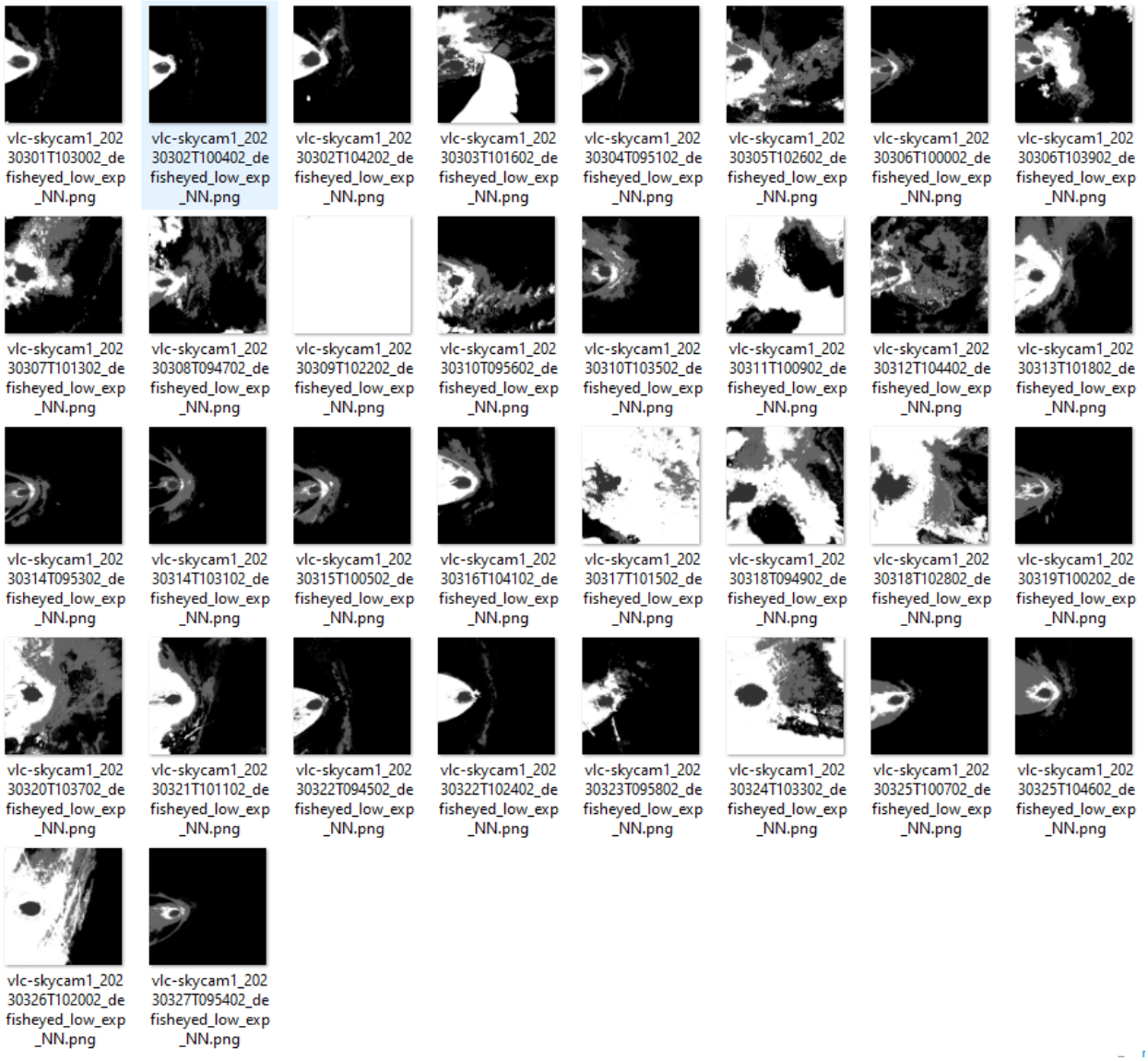

Figure 118: Classified sky camera acquisitions over Rome during Sentinel-3 OLCI overpass

Figure 119 shows the validation results for the OLCI cloud flags including the margin. Only OLCI observations with a OZA below 30 have been considered to lower the influence of parallax between the OLCI observation and the SC observation. When including the margin, the OLCI and SC classifications match 100%

When neglecting the margin (see Figure 120) one of the cloud observations is missed.

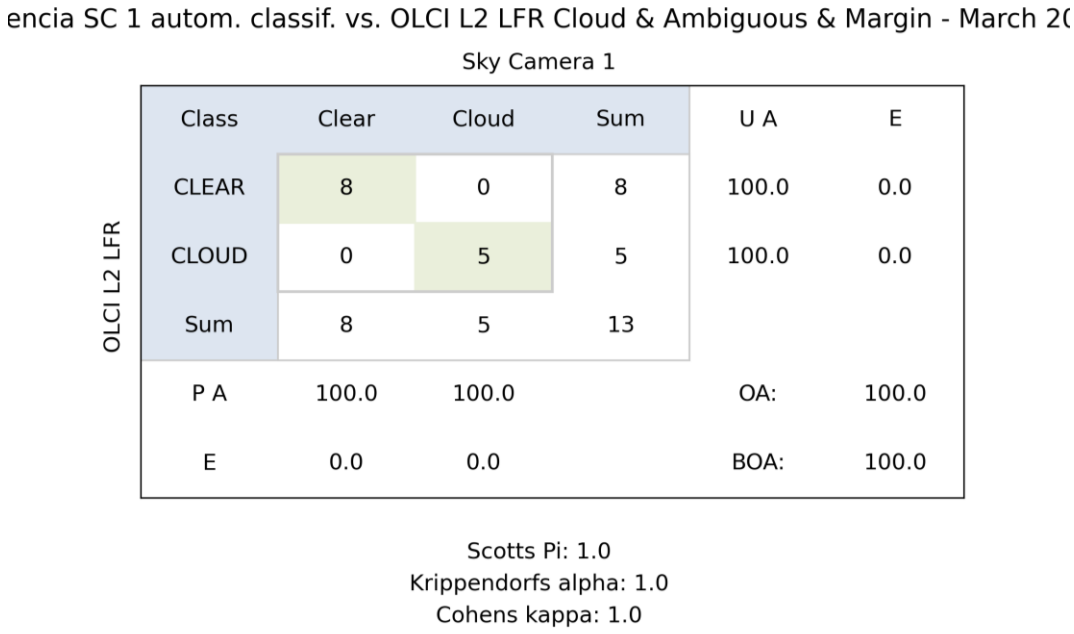

Figure 119: Confusion matrix showing validation results for OLCI L2 cloud screening including margin against SC1 automated classification.

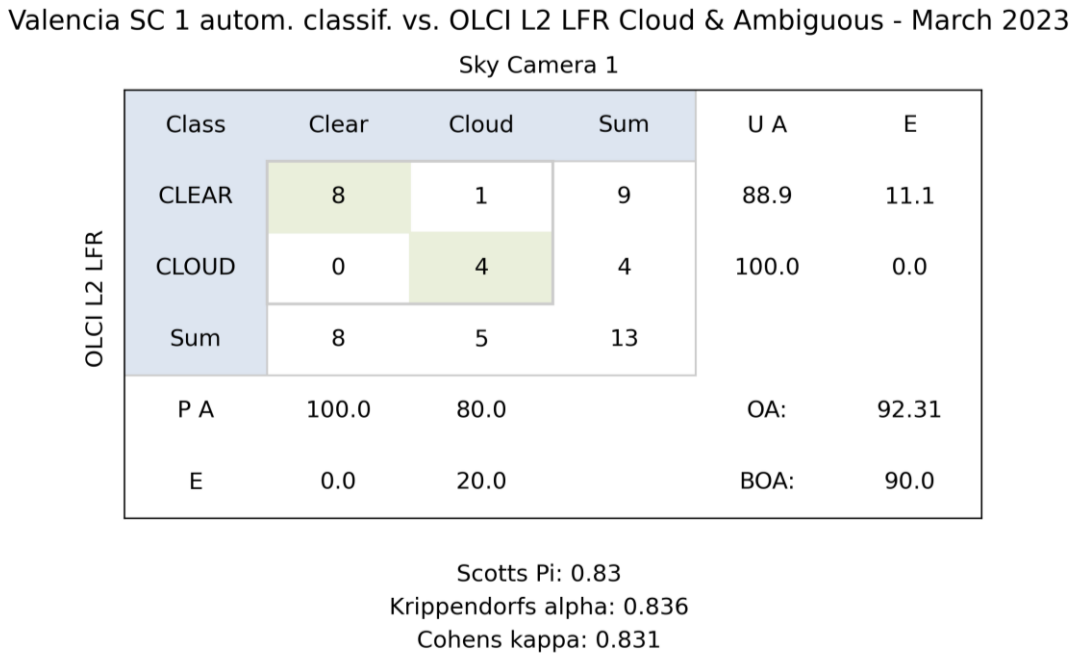

Figure 120: Confusion matrix showing validation results for OLCI L2 cloud screening excluding margin against SC1 automated classification.

5 Validation of Integrated Water Vapour over Land & Water

We continuously investigate the temporal evolution of quality measures of integrated water vapour, when comparing SUOMI NET (Ware et al. 2000) with reduced resolution data of OLCI L2 non-time-critical. All data until March 2022 has been acquired from EUMETSAT CODA, all data from Apr 2022 on has been downloaded from EUMETSAT's datastore (collection id: EO:EUM:DAT:0410).

705.000 (OLCI-A) and 394.000 (OLCI-B) potential matchups within the period of June 2016 (OLCI-A) January 2019 (OLCI-B) to end of March 2023 have been analysed. The global service of SUOMI-NET has been reduced at the end of 2018 thus OLCI-B colocations are less frequent outside North America.

For the cloud detection, the standard L2 cloud-mask has been applied (including the cloud ambiguous and cloud margin flags). The comparison of OLCI and GNSS shows a very high agreement (Figure 121). The correlation between both quantities is around 0.98. The root-mean-squared-difference is 1.9 -2.1 kg/m^2. The systematic overestimation by OLCI is 11%-12%. The bias corrected *rmsd* is around 1.3 kg/m^2.

The temporal evolution of several quality measures (Figure 122), indicates small seasonal variations, which are certainly related to retrieval assumptions. Comparing Figure 122 with the same figure from last month's report, it is noticeable that the numbers of valid matchups hardly changed. The reason is currently under investigation. We suspect a change in the API of EUMETSAT's datastore early March 2023, when version 2.3 was released. Searching for a cause, we detected that the API change required an update of our local software (for details see New features on Data Store 2.3).

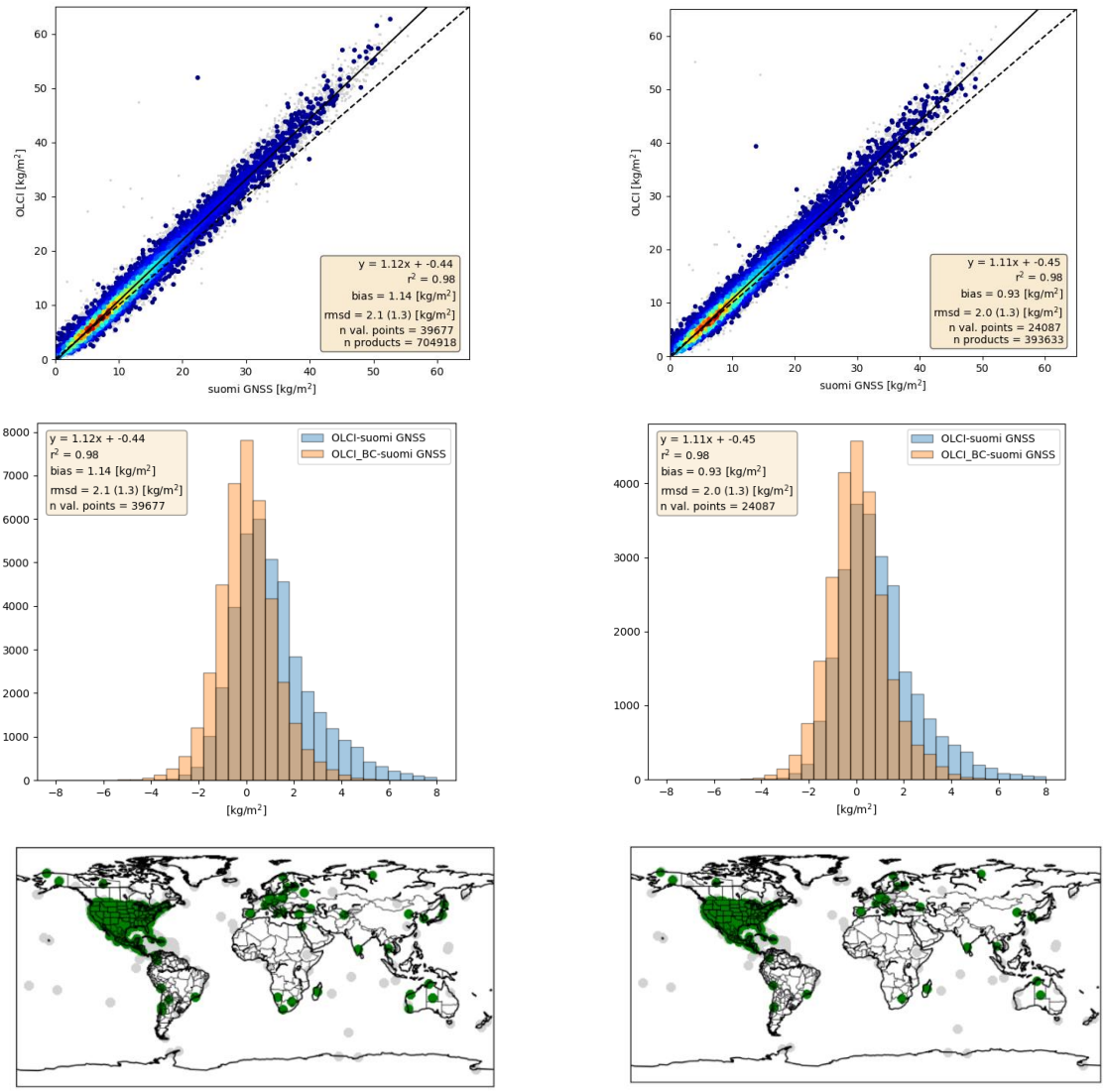

Figure 121: Upper: Scatter plot of the IWV products, derived from OLCI (A left, B right) above land and from SUOMI NET GNSS measurements. Middle: Histogram of the difference between OLCI (A: left, B: right) and GNSS (blue: original OLCI, orange: bias corrected OLCI). Lower: Positions of the GNSS (A: left, B: right).

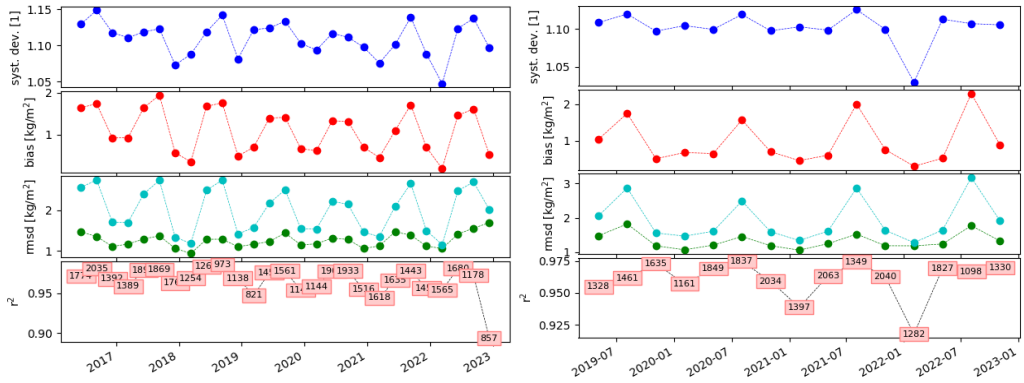

Figure 122: Temporal evolution of different quality measures for OLCI A (left) and OLCI B (right) with respect to SUOMI Net. From top to bottom: systematic deviation factor, bias, root mean squared difference (with and without bias correction), explained variance (number in boxes are the numbers of matchups)

6 Level 2 SYN products validation

6.1 SYN L2 SDR products

6.1.1 Introduction:

Intercomparison of sentinel 3 derived SYNERGY (SYN) surface directional reflectance (SDR) products are carried out against the surface reflectance products observed from MODIS and VIIRS and as a proxy to the in-situ reference data which are unavailable in this exercise for a direct validation.

SYN SDR product is derived from combined measurements of OLCI and SLSTR (Nadir and Oblique) onboard Sentinel 3 and is produced at 300 m spatial resolution. The SYN SDR measurements are compared against the normalized surface reflectance measurements observed from MODIS (MCD43A4.061, a combined Terra and Aqua product), observed at 500 m spatial resolution and from the VIIRS products (VNP43MA4.001) at 1 km spatial resolution. These Nadir BRDF-Adjusted Reflectance (NBAR) products observed from MODIS and VIIRS are corrected to a common nadir view geometry at the local solar noon zenith angle of the day of interest. The SYNERGY derived SDR products thus requires a prior adjustment to the same illumination and viewing conditions and before any intercomparison exercise could be undertaken. The geometric correction is performed with RTLS-R (Ross-Thick-Li-Sparse Reciprocal) BRDF (Bidirectional Reflectance Distribution Function) models, taken from the MODIS product MCD43A1.061 (version 6.1), also a combined Terra and Aqua product and from the VIIRS product, VNP43MA1.001 respectively. Considering the differences in spatial resolution for SYN (300 m), for MODIS (500 m), and for the VIIRS (1 km), the intercomparison exercise is processed at a coarser resolution of 0.01 degree (~ 1 km).

For the current study, the performance assessment of the intercomparison is represented in-terms of statistical variables, namely, Accuracy (A), Precision (P) and Uncertainty (U). For brevity, the Accuracy is known to represent the mean bias of the estimates (or the mean bias error), Precision to represent the repeatability and the uncertainty represents the root mean squared difference.

6.1.2 Results and Discussion:

After the geometric adjustment, the SYN SDR products are evaluated against those observed from MODIS and VIIRS nadir adjusted products. Only the closely matching spectral bands between MODIS and OLCI (difference of 10 nm or less) are selected.

For the inter-comparison exercise, the SYN SDR, MODIS and VIIRS surface directional reflectance (SDR) products are extracted over a 50 X 50 km box, and around several CEOS (Committee on Earth Observation Satellites), LPV (land product validation) sites, during the three month period between 2022-12-1 and 2023-03-01 and inter-comparisons are also drawn between MODIS and SYN SDR are also combined with those observed during the period 2022-09-01 and 2023-03-01 to check for the consistency over the last 6 month period. The selected CEOS LPS sites are known to represent varying biome classes across the globe. Table 6 below provides the list of CEOS LPV selected sites.

Table 6: List of CEOS LPV sited used as reference sites for intercomparison of SYN SDR products.

No	Site acronym	Country	Network	Lat	Lon	Land cover
1	**AU-Cumberland**	Australia	TERN-SuperSites, AusCover/OzFlux	-33.615	150.723	Broadleaved, evergreen
2	**AU-Great-Western**	Australia	TERN-SuperSites, AusCover/OzFlux	-30.192	120.654	Broadleaved, deciduous, open
3	**AU-Litchfield**	Australia	TERN-SuperSites, AusCover/OzFlux	-13.180	130.790	Broadleaved, evergreen
4	**AU-Robson-Creek**	Australia	TERN-SuperSites, AusCover/OzFlux	-17.117	145.630	Broadleaved, evergreen
5	**SP-Ali**	Spain	CORE	38.452	-1.065	Cropland
6	**US-Moab-Site**	United States	NEON, AERONET	38.248	-109.388	Shrub, closed-open, deciduous
7	**US-Talladega**	United States	NEON, AERONET	32.950	-87.393	Needle-leaved, evergreen
8	**AU-Wombat**	Australia	TERN-SuperSites, AusCover/OzFlux	-37.422	144.094	Broadleaved, evergreen
9	**FR-Guayaflux**	France	ICOS Associated	5.279	-52.925	Broadleaved, evergreen
10	**FR-Hesse**	France	ICOS	48.674	7.065	Broadleaved, deciduous, closed
11	**US-Harvard**	United States	NEON, AERONET	42.537	-72.173	Broadleaved, deciduous, closed
12	**US-Mountain-Lake**	United States	NEON, AERONET	37.378	-80.525	Broadleaved, deciduous, closed
13	**AU-Calperum**	Australia	TERN-SuperSites, AusCover/OzFlux	-34.003	140.588	Shrub, closed-open, deciduous
14	**AU-Cape-Tribulation**	Australia	TERN-SuperSites, OzFlux	-16.106	145.378	Broadleaved, evergreen
15	**AU-Rushworth**	Australia	TERN-AusCover	-36.753	144.966	Broadleaved, deciduous, open
16	**AU-Tumbarumba**	Australia	TERN-SuperSites, AusCover/OzFlux	-35.657	148.152	Broadleaved, evergreen
17	**FR-Puechabon**	France	ICOS	43.741	3.596	Needle-leaved, evergreen
18	**IT-Cat**	Italy	CORE	37.279	14.883	Cropland
19	**IT-Lison**	Italy	ICOS	45.740	12.750	Cropland
20	**US-Oak-Rige**	United States	NEON, AERONET	35.964	-84.283	Broadleaved, deciduous, closed
21	**AU-Watts-Creek**	Australia	TERN-AusCover	-37.689	145.685	Broadleaved, evergreen
22	**FR-Montiers**	France	ICOS	48.538	5.312	Broadleaved, deciduous, closed
23	**US-Bartlett**	United States	NEON, AERONET	44.064	-71.287	Broadleaved, deciduous, closed
24	**BR-Mata-Seca**	Brazil	ENVIRONET	-14.880	-43.973	Herbaceous, closed-open
25	**IT-Collelongo**	Italy	EFDC	41.849	13.588	Broadleaved, deciduous, closed
26	**SE-Dahra**	Senegal	KIT / UC	15.400	-15.430	Cultivated and managed areas
27	**AU-Zigzag-Creek**	Australia	TERN-AusCover	-37.474	148.339	Broadleaved, evergreen
28	**FR-Estrees-Mons**	France	ICOS Associated	49.872	3.021	Cultivated and managed areas
29	**NE-Loobos**	Netherlands	ICOS Associated	52.166	5.744	Needle-leaved, evergreen
30	**FR-Aurade**	France	ICOS	43.550	1.106	Cropland
31	**IT-Tra**	Italy	CORE	37.646	12.867	Cropland
32	**CR-Santa-Rosa**	Costa Rica	ENVIRONET	10.842	-85.616	Broadleaved, evergreen

Figure 123 shows the scatter plots of inter-comparison between MODIS and Sentinel3-A SYN SDR (OLCI bands) and for spectral band pairs, b01 vs Oa08 (Figure 123a), b02 vs Oa17 (Figure 123b), b03 vs Oa04 (Figure 123c) and b04 vs Oa06 (Figure 123d) and for the data extracted for the CEOS LPV sites shown in table 8 above.

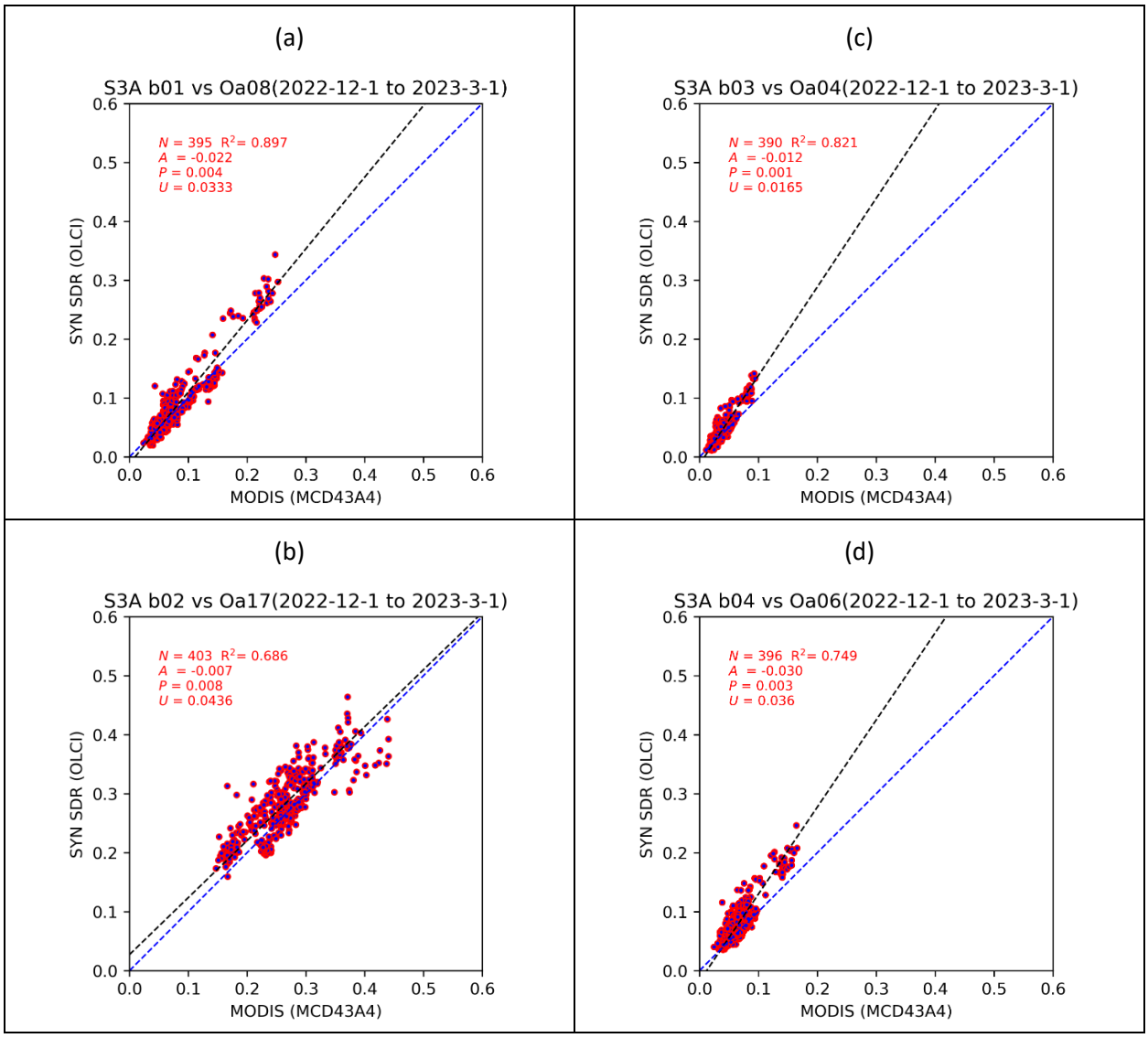

Figure 123: Scatter plots of intercomparison between sentinel S3A SYN SDR (OLCI) and MODIS for selected band pairs, b01 vs Oa08 (a), b02 vs Oa17 (b), b03 vs Oa04 (c) and b04 vs Oa06 (d).

Similarly, Figure 124 shows the overall scatter plots from the intercomparison of Sentinel3-B SYN SDR with MODIS for several spectral band pairs, b01 vs Oa08 (Figure 124a), b02 vs Oa17 (Figure 124b), b03 vs Oa04 (Figure 124c) and b04 vs Oa06 (Figure 124d)

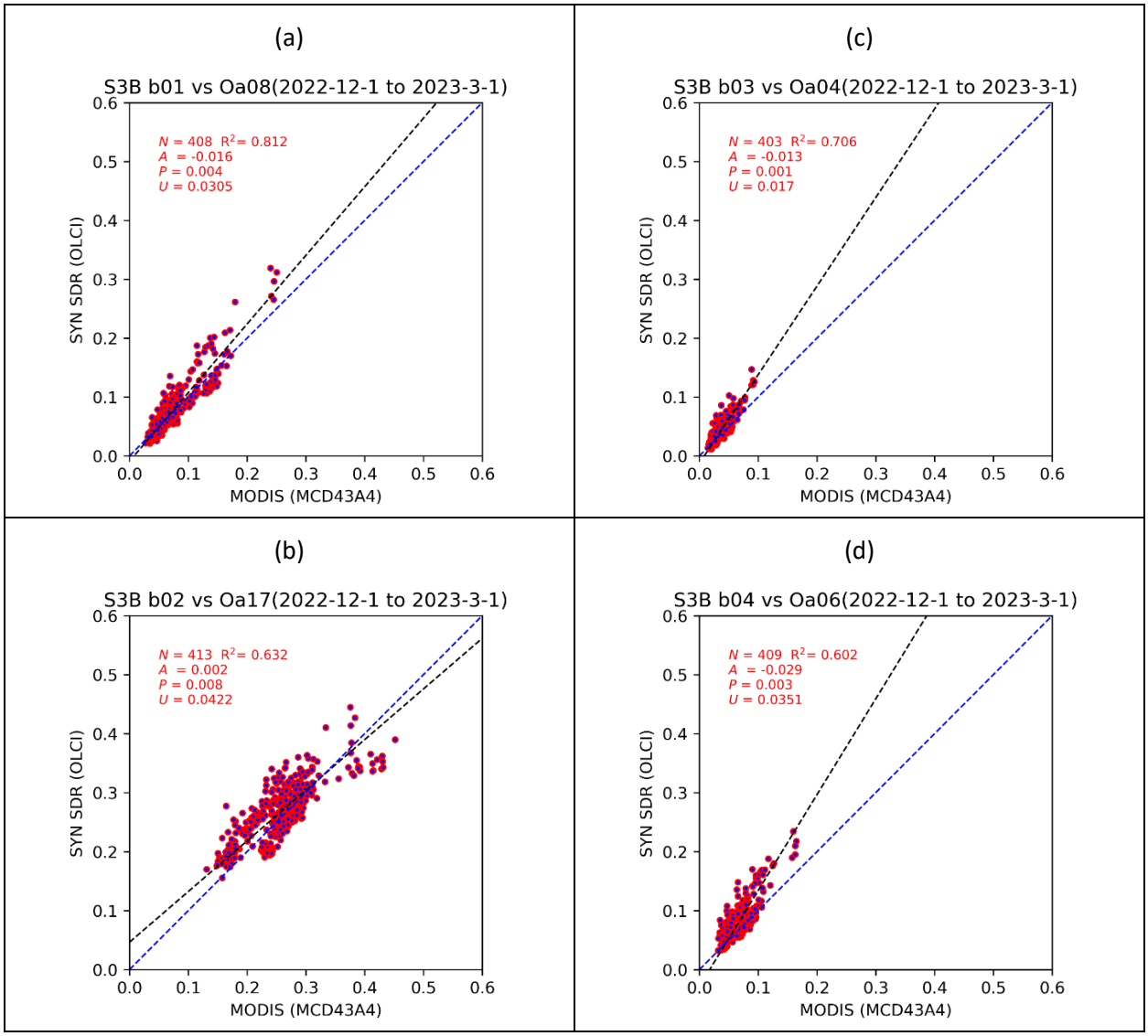

Figure 124: Scatter plot of intercomparison between sentinel S3B SYN SDR (OLCI) and MODIS for selected band pairs, b01 vs Oa08 (a), b02 vs Oa17 (b), b03 vs Oa04 (c) and b04 vs Oa06 (d)

An overall good comparison is observed between Sentinel S3A/S3B derived SYN SDR (OLCI) and MODIS surface reflectance products, and for all the selected spectral band pairs. Slightly better statistical scores are observed for Sentinel S3B SYN SDR (Figure 124) as compared to Sentinel S3A (Figure 123) as can be seen from the statistical indicators “U” or “RMSE” in the figures.

Similarly, Figure 125 shows the overall scatter plots from the intercomparison of Sentinel3-A SYN SDR with VIIRS for several spectral band pairs, M5 vs Oa09 (Figure 125a), M7 vs Oa17 (Figure 125b), M3 vs Oa04 (Figure 125c) and M4 vs Oa06 (Figure 125d)

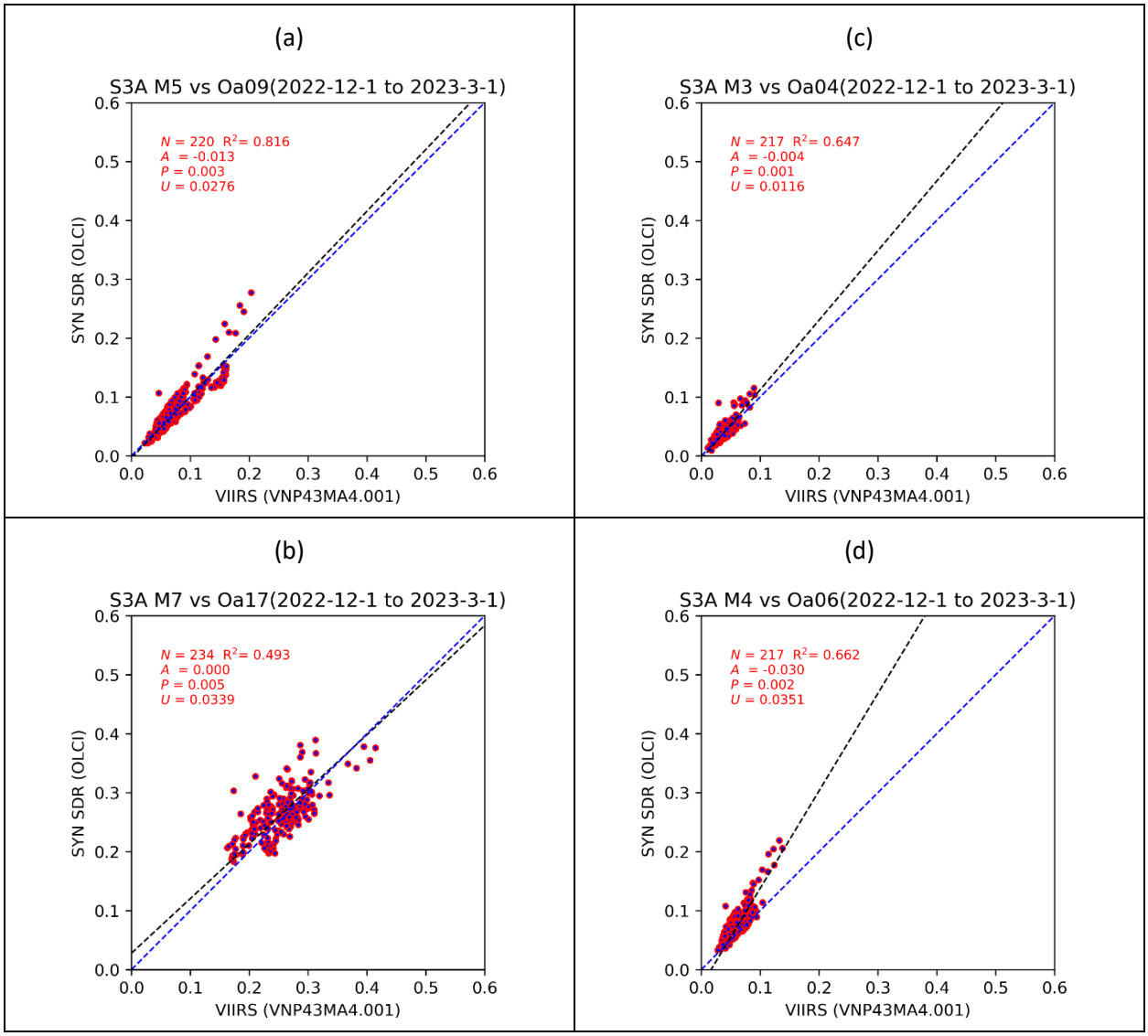

Figure 125: Scatter plot of intercomparison between sentinel S3B SYN SDR (OLCI) and VIIRS for selected band pairs, M5 vs Oa09 (a), M7 vs Oa17 (b), M3 vs Oa04 (c) and M4 vs Oa06 (d)

Similarly, Figure 126 shows the overall scatter plots from the intercomparison of Sentinel3-B SYN SDR with VIIRS for several spectral band pairs, M5 vs Oa09 (Figure 126a), M7 vs Oa17 (Figure 126b), M3 vs Oa04 (Figure 126c) and M4 vs Oa06 (Figure 126d).

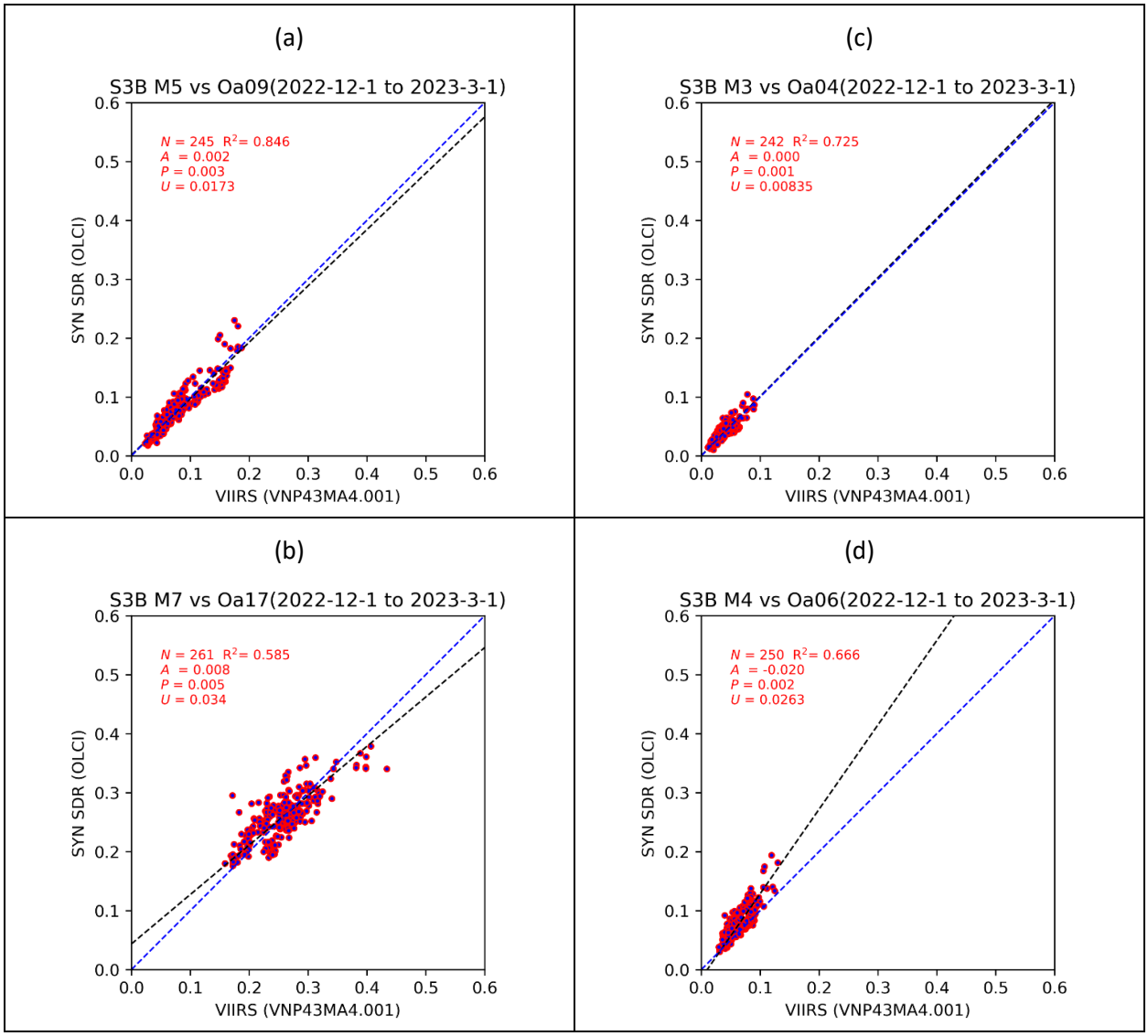

Figure 126: Scatter plot of intercomparison between sentinel S3B SYN SDR (OLCI) and VIIRS for selected band pairs, M5 vs Oa09 (a), M7 vs Oa17 (b), M3 vs Oa04 (c) and M4 vs Oa06 (d)

An overall good comparison is observed between Sentinel S3A/S3B derived SYN SDR (OLCI) and VIIRS surface reflectance products, and for all the selected spectral band pairs. Slightly better statistical scores are observed for Sentinel S3B SYN SDR (Figure 126) as compared to Sentinel S3A (Figure 123) as can be seen from the statistical indicators “U” or “RMSE” in the figures.

Figure 127 shows the scatter plots of inter-comparison between MODIS and Sentinel3-A SYN SDR (OLCI) and for spectral band pairs, b01 vs Oa08 (Figure 127a), b02 vs Oa17 (Figure 127b), b03 vs Oa04 (Figure 127c) and b04 vs Oa06 (Figure 127d) and for the data extracted for all the CEOS LPV sites during the period 2022-09 and 2023-02. This exercise is done to check the consistency of reflectance products observed over the last 6 months period.

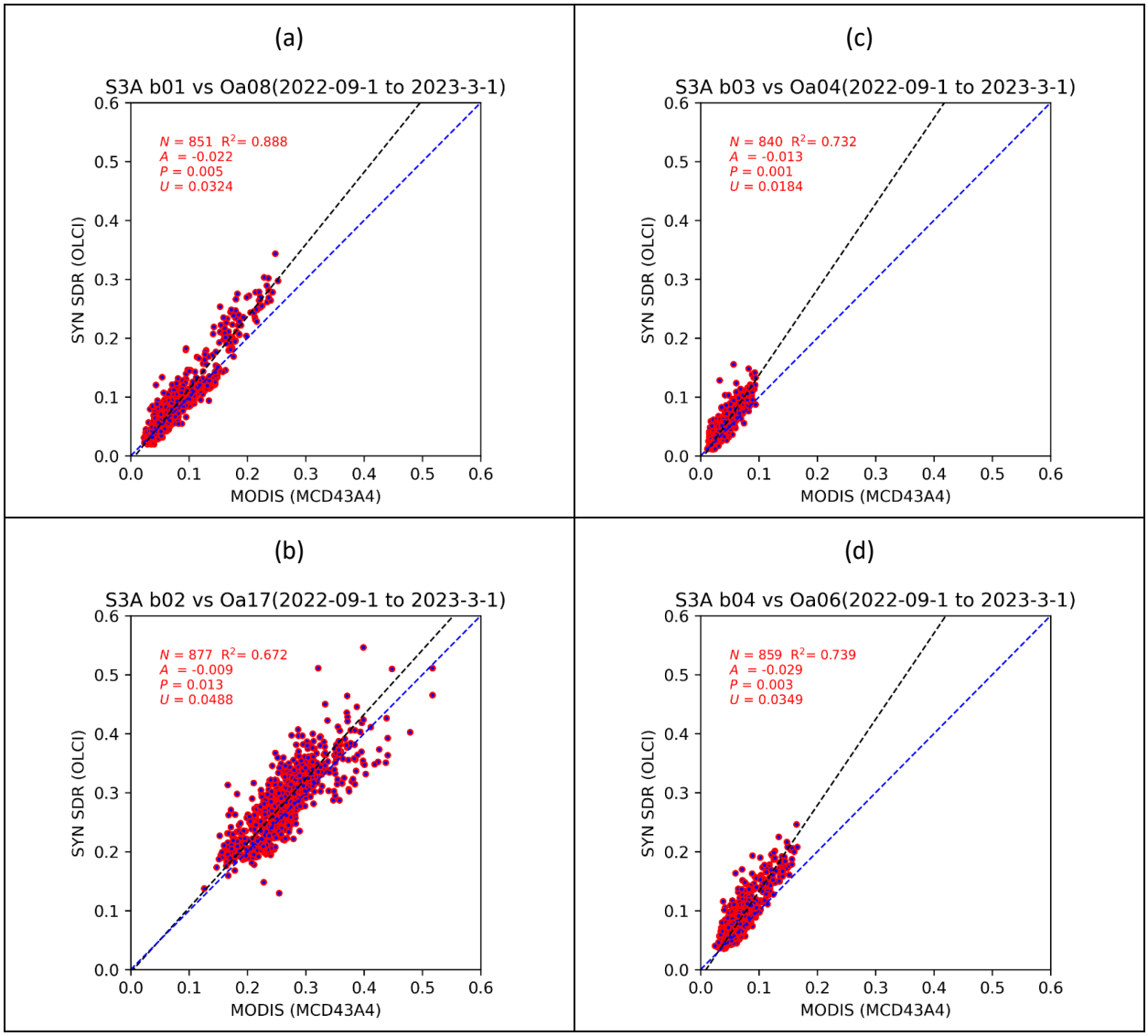

Figure 127: Scatter plot of intercomparison between sentinel S3A SYN SDR (OLCI) and MODIS for selected band pairs, b01 vs Oa08 (a), b02 vs Oa17 (b), b03 vs Oa04 (c) and b04 vs Oa06 (d)

Also, shown in Figure 128, is the scatter plots of inter-comparison between MODIS and Sentinel3-B SYN SDR (OLCI) and for spectral band pairs, b01 vs Oa08 (Figure 128a), b02 vs Oa17 (Figure 128b), b03 vs Oa04 (Figure 128c) and b04 vs Oa06 (Figure 128d) and for the data extracted for all the CEOS LPV sites during the period 2022-09 and 2023-02.

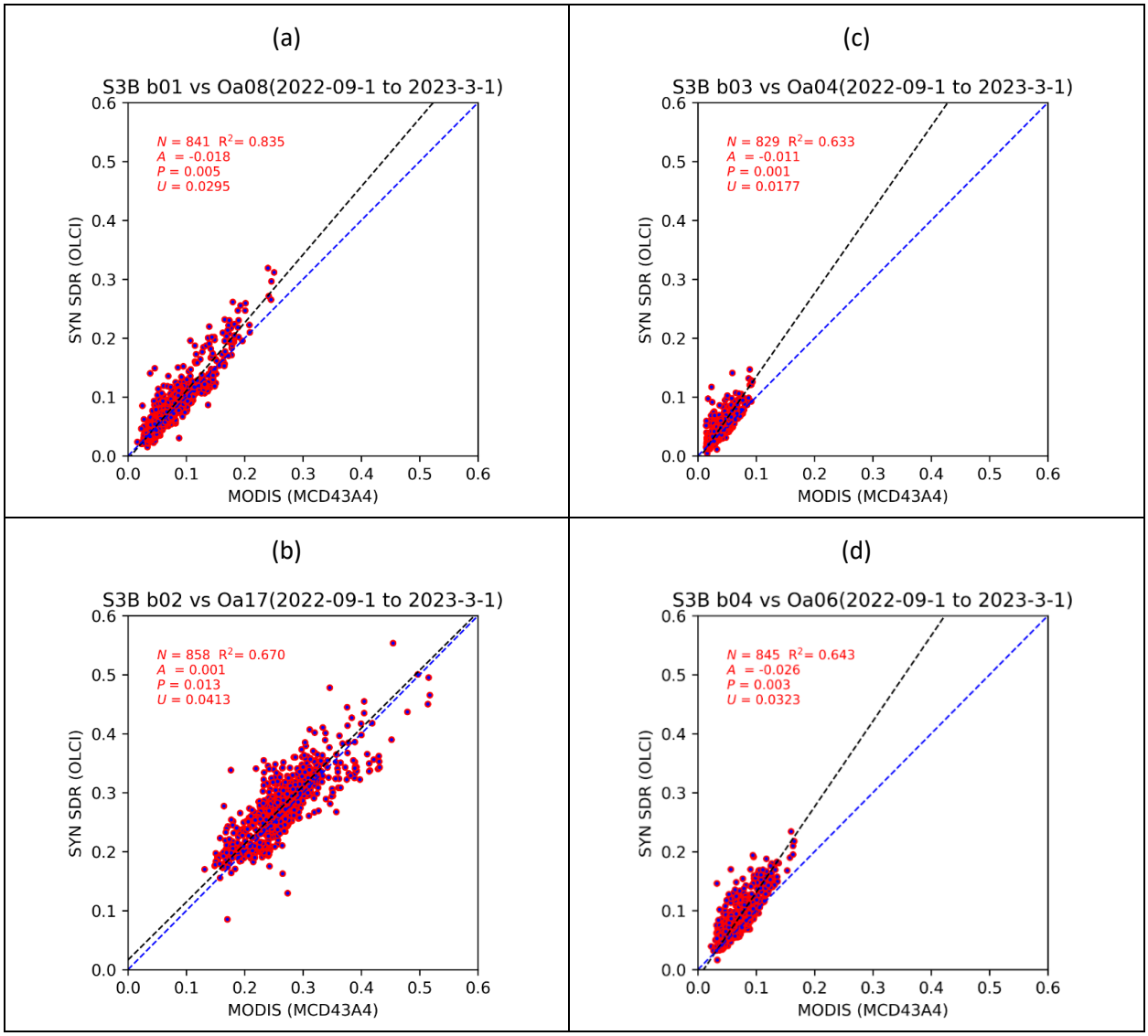

Figure 128: Scatter plot of intercomparison between sentinel S3B SYN SDR (OLCI) and MODIS for selected band pairs, b01 vs Oa08 (a), b02 vs Oa17 (b), b03 vs Oa04 (c) and b04 vs Oa06 (d)

From the two figures above, Figure 127 and Figure 128, a good consistency is observed between the Sentinel3-A/B derived SYN SDR products and MODIS products for an extended period of five months.

6.1.3 Conclusion

Under the OPT-MPC project and under the routine service validation, the Sentinel 3, derived SYNERGY SDR products are inter-compared against the MODIS and VIIRS nadir adjusted surface reflectance products. In general, a good agreement is observed between both Sentinel 3 A/B derived SYN SDR vis-à-vis MODIS and VIIRS surface reflectance products. The observed statistical scores are slightly better with S3B than compared to S3A as observed from uncertainty metrics. Overall, the correction of discrepancies with respect to acquisition geometry greatly improved the bias associated with SYN SDR products. The differences in spectral response functions as observed between spectral band pairs used in inter-comparisons has certain impact and it is envisaged to work on such spectral adjustment methods for the future inter-comparison exercise.

6.2 SY_2_VGP, SY_2_VG1 and SY_2_V10 products

The similarity of SYN VGT like products with the PROBA-V archive is evaluated through intercomparison of 10-daily composites extractions over LANDVAL [1] sites. Since there is no overlap with the PROBA-V nominal operational phase and no PROBA-V Collection 2 climatology is available yet, direct comparison is done by comparing the SY_2_V10 NTC products starting January/2021 with those of PROBA-V S10-TOC since January/2018.

The temporal evolution of statistics results below is based on intercomparison over the entire periods up to March/2023. The scatterplots are based on intercomparison between SY_2_V10 products of March/2023 with PROBA-V Collection 2 S10-TOC products of March/2020.

Products availability

Availability of SY_2_VG1 and SY_2_V10 products is checked through an automated query and download via the Copernicus Collaborative Node and the Copernicus Open Access Hub feeding the products database Belgian Collaborative Ground Segment (Terrascope, www.terrascope.be). For the month March/2023, there are a number of data quality issues with a deviating amount of missing data and empty tiles in the product listed below.

- S3A_SY_2_VG1____20230315T000000_20230315T235959_20230317T*____PS1_O_NT_002

Statistical consistency

The scatter density plots with geometric mean regression equation, coefficient of determination (R^2) and APU statistics based on intercomparison between SY_2_V10 products of March/2023 with PROBA-V Collection 2 products of March/2020 are shown in Figure 129. The APU statistics are defined as: Accuracy (A) or average bias, Precision (P) or the standard deviation of the bias, and Uncertainty (U) or the Root Mean Squared Distance. Accuracy is best for BLUE (< 1%), less good for RED (~2%) and NIR (~1%) and worse for SWIR (~-8%). The relatively large values for Precision (large scatter, low R^2) are caused by the fact that products of two different years are compared. The disagreement for the SWIR band is related to the SLSTR calibration offset (in bands S5 and S6).

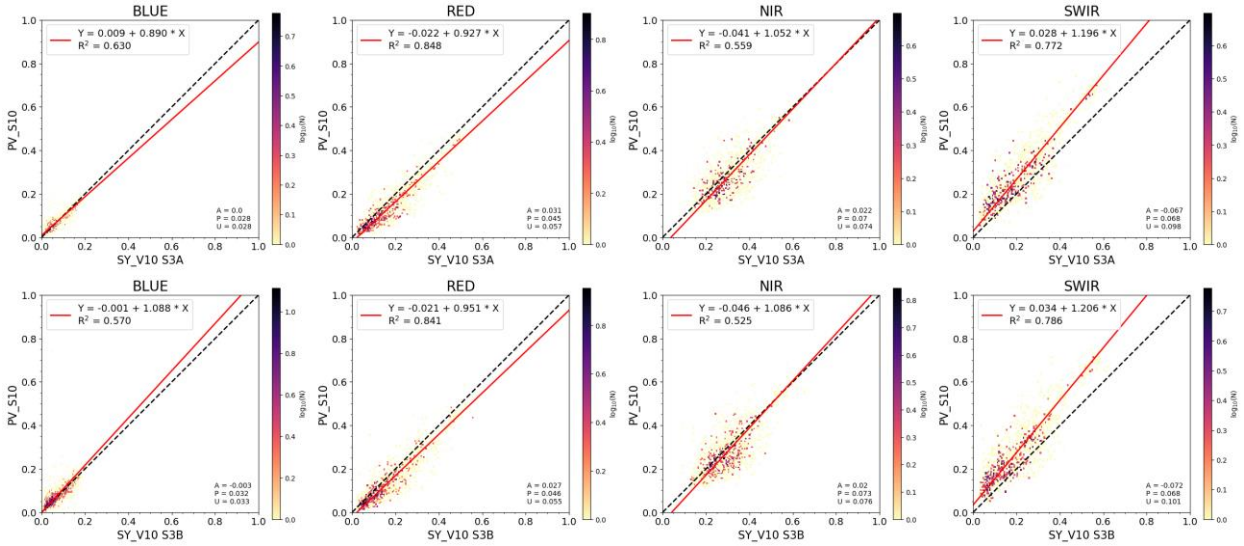

Figure 129: Scatter density plots between SY_V10 S3A (top) or S3B (bottom) and PROBA-V C2 S10-TOC for BLUE, RED, NIR and SWIR bands (left to right), March/2023 vs. March/2020

Temporal consistency

The temporal evolution of APU statistics derived from intercomparison of SY_2_V10 NTC products January/2021 – March/2023 with those of PROBA-V S10-TOC January/2018 – March/2020 (Figure 130). The APU statistics show stable evolution over time, although some seasonal pattern is observed for the mainly the SWIR channel, and to a lesser extent the RED and NIR channel. The temporal behaviour is stable.

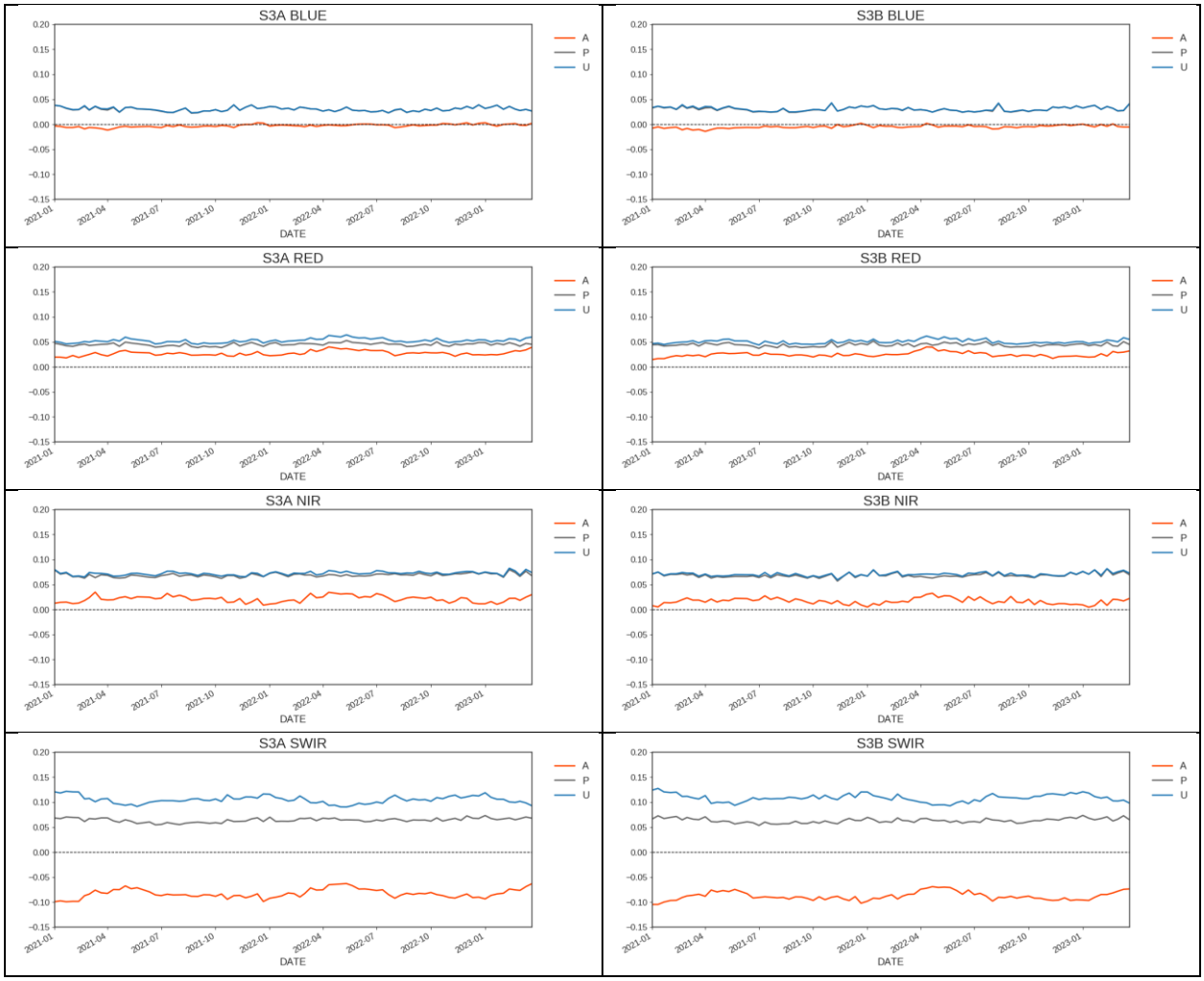

Figure 130: Temporal evolution of APU statistics between SY_2_V10 S3A (left) or S3B (right) and PROBA-V S10-TOC for BLUE, RED, NIR and SWIR bands (top to bottom), January/2021 - March/2023 (S3 SYN VGT) vs. January/2018 - March/2020 (PROBA-V)

References

[1] B. Fuster *et al.*, "Quality Assessment of PROBA-V LAI, fAPAR and fCOVER Collection 300 m Products of Copernicus Global Land Service," *Remote Sens.*, vol. 12, no. 6, p. 1017, Mar. 2020, doi: 10.3390/rs12061017.

6.3 SYN L2 AOD NTC products

There has been no new result during the reporting period. The last figures (reported in OLCI Data Quality Report covering February 2023) are considered valid.

7 Events

For OLCI-A, four Radiometric Calibration sequences have been acquired during the reported period:

- S01 sequence (diffuser 1) on 12/03/2023 05:13 to 05:15 (absolute orbit 36795)
- S01 sequence (diffuser 1) on 22/03/2023 10:56 to 10:58 (absolute orbit 36941)
- S01 sequence (diffuser 1) on 31/03/2023 18:46 to 18:48 (absolute orbit 37074)
- S05 sequence (diffuser 2) on 31/03/2023 20:27 to 20:29 (absolute orbit 37075)

For OLCI-B, four Radiometric Calibration sequences have been acquired during the reported period:

- S01 sequence (diffuser 1) on 11/03/2023 08:22 to 08:24 (absolute orbit 25389)
- S01 sequence (diffuser 1) on 21/03/2023 19:08 to 19:10 (absolute orbit 25538)
- S01 sequence (diffuser 1) on 31/03/2023 02:58 to 03:00 (absolute orbit 25671)
- S05 sequence (diffuser 2) on 31/03/2023 04:39 to 04:41 (absolute orbit 25672)

8 Appendix A

All Data Quality Reports, as well as past years Data Quality Reports and Annual Performance Reports, are available on dedicated pages in Sentinel Online website, at:

- https://sentinel.esa.int/web/sentinel/technical-guides/sentinel-2-msi/data-quality-reports
- https://sentinel.esa.int/web/sentinel/technical-guides/sentinel-3-olci/data-quality-reports
- https://sentinel.esa.int/web/sentinel/technical-guides/sentinel-3-slstr/data-quality-reports
- OPT Annual Performance Report Year 2022 (PDF document)

End of document